Stony Brook University

Local and Long Range Structure: Studies of Oxygen Ion Conductors through the use of Solid State ^{17}O and ^{71}Ga NMR Spectroscopy and X-Ray Powder Diffraction

A Dissertation Presented

by

John Luigi Palumbo

to

The Graduate School

in Partial Fulfillment of the

Requirements

for the Degree of

Doctor of Philosophy

in

Chemistry

Stony Brook University

August 2007

John Luigi Palumbo

We, the dissertation committee for the above candidate for the

Doctor of Philosophy degree, hereby recommend

acceptance of this dissertation.

Clare P. Grey - Advisor
Chemistry Department

John B. Parise - Chairperson
Earth and Space Sciences Department

David M. Hanson – 3rd Member
Chemistry Department

Jonathan C. Hanson - Outside Member
Chemistry Department, Brookhaven National Laboratory

This dissertation is accepted by the Graduate School

Lawrence Martin
Dean of the Graduate School

Abstract of the Dissertation

Local and Long Range Structure: Studies of Oxygen Ion Conductors through the use of Solid State ^{17}O and ^{71}Ga NMR Spectroscopy and X-Ray Powder Diffraction

by

John Luigi Palumbo

Doctor of Philosophy

in

Chemistry

Stony Brook University

2007

The research presented here involves the study of disordered crystalline materials, in an effort to determine how structure on the long range order as well as at the atomic level relates to function. Through the use of ^{71}Ga and ^{17}O Magic Angle Spinning Nuclear Magnetic Resonance (MAS NMR) and X-ray Powder Diffraction (XRD), changes in structure have been observed as a function of heat treatment and/or synthetic conditions. In particular, oxygen ion conduction of crystalline materials has been the focus of this thesis, where mechanisms of conductivity have been related to structure. The change in local and long range order of the relationship between the pyrochlore and fluorite structures as a result of synthesis conditions and heat treatment. Using the techniques mentioned above, a detailed description of cation ordering has emerged which helps describe ionic conductivity in these structures. Another study in this work examines anionic vacancy formation as a function of doping into the perovskite structure $LaGaO_3$. Vacancies provide a mechanism for conduction where oxygen ions can hop. Determining the local order in these structures helps to understand the mechanism responsible for this phenomenon. The following work describes how characterization of the local and long range order contribute to the overall understanding of ionic conduction in these materials.

Table of Contents

Chapter 3

^{17}O NMR Studies of the Fluorite to Pyrochlore Transition of Sol-gel Derived Compositions Along the $Y_2Ti_2O_7$ – $Y_2Zr_2O_7$ Binary

Chapter 4

Studies of Structure and Dynamics of $La_{1-x}Sr_xGa_{1-y}Mg_yO_{3-(x+y)/2}$ (LSGM) through the use of Variable Temperature ^{17}O and ^{71}Ga MAS NMR Spectroscopy and X-Ray Diffraction

Chapter 5

The Detection of the Development of Crystallization of LSGM Perovskites through the use of ^{17}O and ^{71}Ga NMR Spectroscopy and X-ray Powder Diffraction

Chapter 6

Conclusion

Table of Figures

List of Tables

Acknowledgement

In the course of my studies as a graduate student, I gave and received much support from the present and past members of the Clare P. Grey research group. However, none of it would have happened if it were not for the strong commitment and extreme hard work of my advisor for whom I am especially grateful.

Addition acknowledgements to Jonathan C. Hanson for assistance at BNL. Tobias A. Schaedler and Carlos G. Levi for stimulating collaborations as well as Namjun Kim and Luming Peng for sharing their experience with NMR.

Chapter 1:

Introduction

1.1 Abstract

Ionic conduction in ceramics has become a major field of research. As society searches for alternatives to fossil fuels, many have turned to hydrogen as an alternate. Solid Oxide Fuel Cells (SOFC) take advantage of converting chemical energy directly to electrical energy, which offers a clean and abundant source of fuel. To further improve the efficiency of SOFCs, a detailed understanding of the mechanism of ionic conduction is necessary. Often these materials have complex structures that require characterization on the local, atomic level, as well as on the macro level. The following chapters describe the characterization of ionic conducting ceramics on the local and macro levels in an attempt to lend insight into the mechanism of ionic conduction. In this chapter, a brief introduction is provided which details some of the theories and methods used in this study.

1.2 Solid Oxide Fuel Cells (SOFC)

For over a century, certain ceramic materials have been known to exhibit oxide ion conduction [2]. The first commercial application was around 1897 in Nernst Lamps. Using zirconium oxide ZrO_2, yttrium oxide Y_2O_3 and erbium oxide Er_2O_3 'Nernst Glowers' were manufactured by George Westinghouse in the United States at the turn of the century. Since then, oxide ion conductors have been used primarily in Lambda Sensors, which are devices used in automobiles to regulate catalytic activity by sensing the amount of oxygen present.

SOFCs offer environmentally sound alternatives to fossil fuels; therefore, they are on the forefront of technologies that vie to replace traditional powers sources such as fossil fuel driven power plants and the internal combustion engine (fig 1.1 and 1.2) [3].

Figure 1. 8 Fuel cell substation in West Babylon, NY as a part of LIPA's fuel cell substation with 3 rows of 25 grid connected fuel cells [4].

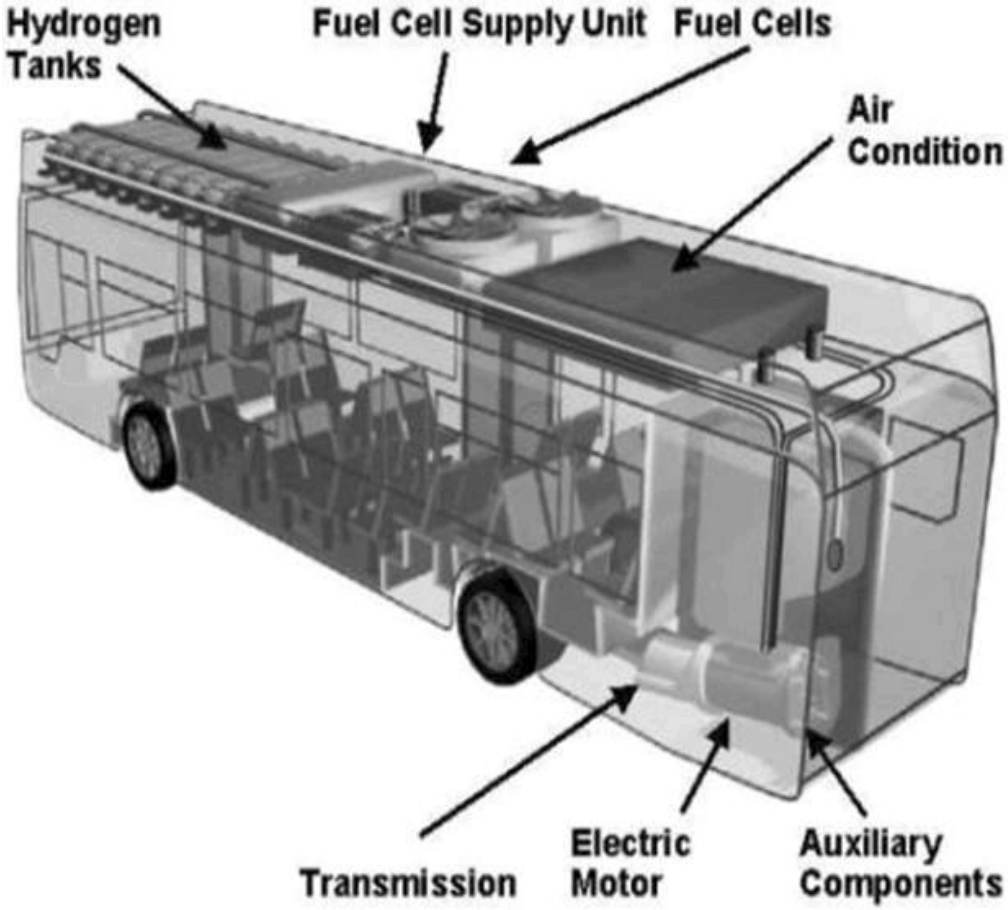

Figure 1. 9 Fuel cell bus [4].

In SOFCs, chemical energy is converted directly to electrical energy. SOFCs have greater fuel efficiency [2] than the internal combustion engine. However, there are difficulties in storage and delivery of hydrogen gas.

In a SOFC, O_2 is reduced at the cathode, and flows through the electrolyte in the form of the anion, O^{2-}. At the anode, the oxide ions combine with H_2 gas generating electrons and water. The electrons flow through a circuit to do work, and water is the primary waste product (figure 3).

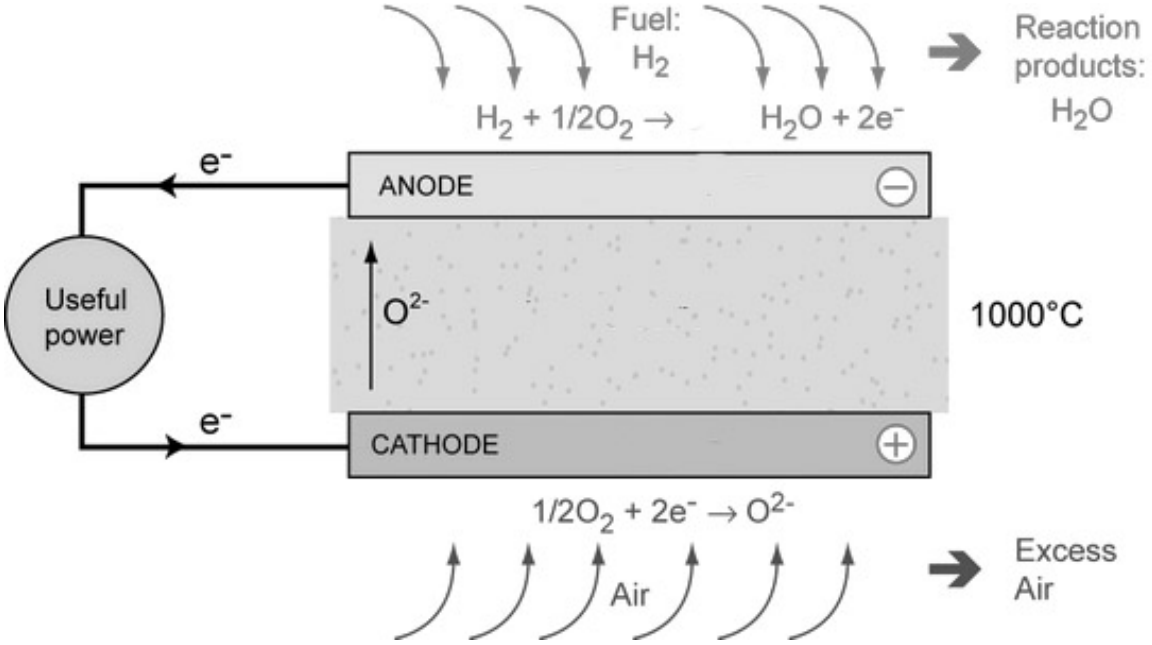

Figure 1. 10 Schematic of a SOFC [5].

SOFC technology relies on oxygen ion conduction through a ceramic electrolyte to deliver electrons to the load. The mechanism of oxygen ion travel is via a vacancy hopping through the electrolyte. To date, the electrolyte of choice is yttrium stabilized zirconia (YSZ) [6]. However, a doped variant of the compound $LaGaO_3$ is under consideration for its lower operating temperature. In 1994, doped $LaGaO_3$ was shown to exhibit exceptional oxygen ion conductivity [6]. Lanthanum gallate doped with 10% Sr on the lanthanum site and 10% Mg on the gallium site (LSGM), has the highest conductivity of several known ionic conductors [6]. The conductivity at 850°C of LSGM is comparable to that of yttrium stabilized zirconia (YSZ) at 1000°C. [7]. This decrease in operating temperature brings SOFC technology closer to being a viable alternative, for lowering the operating temperature allows greater flexibility in engineering the SOFC [8]. Another issue of the SOFC is compatible thermal expansion coefficients of the cathode, anode and electrolyte. For the all perovskite SOFC, thermal expansion coefficients are all similar, reducing wear from thermal cycling [9].

1.3 Ionic Conduction

Ionic conduction in a crystalline solid largely takes place by point defects in the crystalline lattice. The two basic types of point intrinsic defects are *Schottky* defects or *Frenkel* defects [10]. Schottky defects are generally described as vacancies on the lattice sites (either cation and/or anion) and are charge balanced. Frenkel defects differ from Schottky defects in that they occur off of the lattice site in an empty space in the crystal called an interstitial (figures 4 and 5). However, when the concentration of defects becomes sufficiently high (>1%), it

is not clear that these defects can be considered either of these types of defects; they may be regarded as an inherent part of the structure [11].

Extrinsic defects are another category of ionic defects where a foreign material is introduced into the crystalline lattice. Referred to as doping, these foreign materials often have a different charge than the host site. If, for example, the defect introduced into the crystal has a lower charge than the host site, a vacancy may be formed at the anion site or an additional cation will be introduced to maintain charge balance [10].

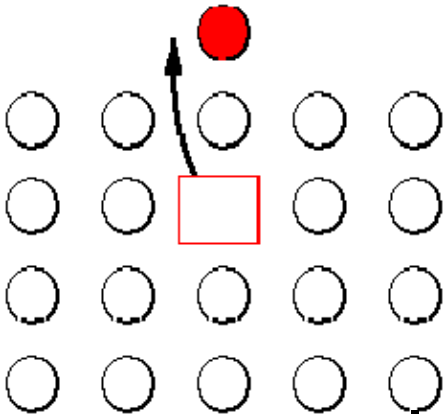

Figure 1. 11 Schematic lattice displaying a Schottky defect. The square in the middle of the image is a vacancy formed by the removal of an atom from the lattice.

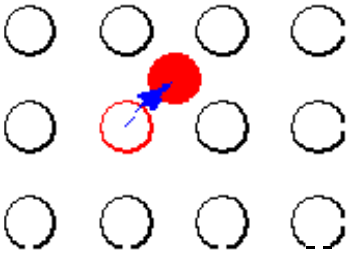

Figure 1. 12 Schematic depicting of a Frenkel defect. Displacement of atom in crystalline lattice into an empty space in the crystal known as an interstitial.

1.4 Introduction to Soft Mechanochemical Synthesis

One approach that has been used to prepare materials described in this thesis is the use of soft mechanochemical synthesis. Applications in chemistry began with mechanochemical synthesis by J.S. Benjamin in 1976 to make metal alloys ($Ni_{60}Nb_{40}$) by "a high energy ball milling technique" [12]. It was also reported that in 1981 *A. E.Ermakov* produced 'amorphous' powders of YCo_3, YCo_5, Y_2Co_7, and Y_2Co_{17} by the same technique [13]. Then in 1995, J. Ding *et al* synthesized ultra fine Fe powder using mechanochemical synthesis [14]. However, it was not until about 1999 that the first metal oxide was synthesized using this technique. S. E. Lee *et al* synthesized lead zirconate titanate [15], $Pb(Zr_xTi_{1-x})O_3$ (PZT) by mechanically activating PbO, ZrO_2 and TiO_2 to form nanocrystalline PZT as detected by XRD. Then in 2000 Q. Zhang *et al* synthesized the perovskite $LaMnO_3$ where, after 180 min of milling, a perovskite diffraction pattern appeared [16]. Often, ball milling affords less treatment at high temperature .

1.4.1 Theory of how Soft Mechanochemical Synthesis works

Mechanochemistry has a wide range of modern applications. Areas of interest include chemistry, physics, metallurgy, materials research, geochemistry, mining, environmental protection, biology, pharmacology [17][16].

To date, no complete theory exists as to why chemical reactions take place during the mechanical activation process [18, 19] however, there have been explanations as to how chemical reactions do occur.

V.V. Zyryanov [19] proposes the 'reaction zone' model to describe chemical phenomenon observed from mechanical processing of metal oxide reactants. This model proposes the formation of a dynamic state D^* from the action of the balls in the mill and the formation of material supersaturated with vacancies formed from the relaxation of D^* (figure 6).

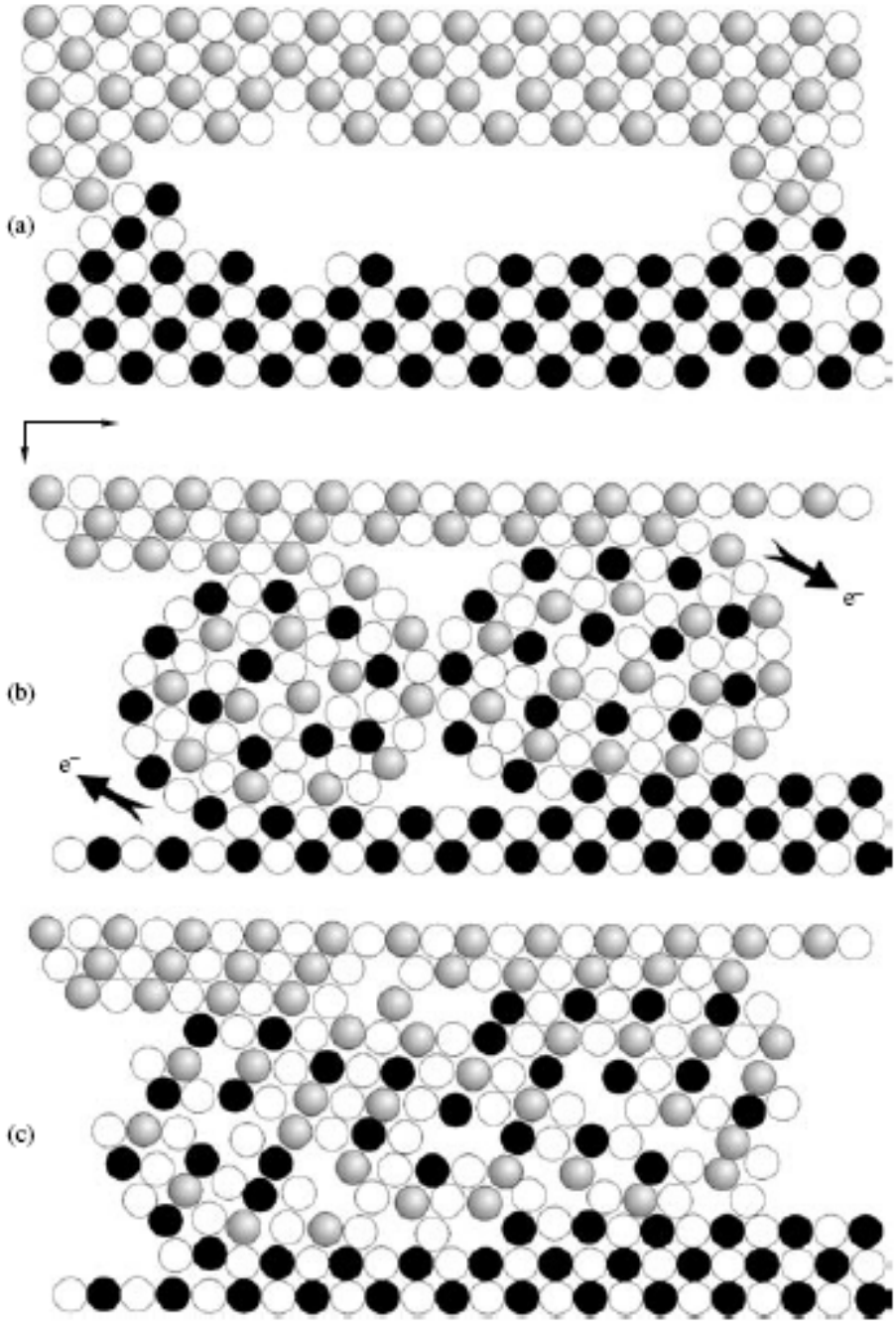

Figure 1. 13 Two-dimensional scheme illustrating the development of a dynamic state (D)* in the contact regions as a result of a primary loading event: (a) initial state; (b) roll growth until collision, accompanied by emission processes, (c) relaxation of (*D*)* to the primary product[18].

Some of the key components of the reaction zone model are dependent on the geometry of the reaction vessel and the governing classical physics behind the set up such as [18]:

1) The area of impact of the ball on the flat powder layer on the wall of the vessel;
2) The thickness of the layer of the sample on the vessel wall that is being enacted on by the ball;
3) The volume of the sample in the vessel;
4) The ball velocity in an average impact.

Often the resulting material is in an amorphous state and can be crystallized upon heating. As shown in chapter 5, initially amorphous products can form crystalline materials at relatively lower temperatures compared to that found in the literature.

1.5 Solid State Nuclear Magnetic Resonance Spectroscopy (NMR)

NMR is a useful analytical tool for extracting local geometry about an element of interest. In particular, the use of ^{17}O NMR to study the local structures of metal oxides is becoming increasingly popular due to the advancements in NMR equipment and the increased technological relevance of this diverse class of compounds. Measurement of the oxygen environment at the local level often aids in the interpretation of other techniques which measure long range structure, such as X-ray diffraction (XRD). Interpreting these data together often results in a model of the structure that facilitates structural details. However, the measurement and interpretation of ^{17}O NMR spectra is often difficult due to multiple interactions involving the nucleus and its local environment. Also the low natural abundance of ^{17}O (0.04%) and the difficulty involved in performing an ^{17}O enrichment add to the difficulty in acquiring spectra as well as it's quadrupolar nature (I = 5/2) as discussed in the next section.

1.5.1 Quadrupolar Nuclei

Most of the spin active nuclei in the periodic table have spin quantum numbers (I) > ½ and are quadrupoles. For a quadrupolar nucleus, the charge at the nucleus does not have a spherical distribution[19] and can be described by the relation eQ, where e is the fundamental electric charge (C), and Q the electric quadrupole moment (in units of Cm^2), defined as:

$$Q = \frac{3K \quad - I(I+1)}{(I+1)(2I+3)} Q_0 \qquad [1.1]$$

$$Q_0 = \int \rho(3z^2 - r^2) dV \qquad [1.2]$$

where K is the projection along the z axis the defines the direction of distortion and ρ is the charge density.

There are significant interactions between the the quadrupolar moment of the nucleus (which is an inherent property possessed by the nucleus and does not change) with the surrounding electric field gradient (EFG). The EFG is described with 3 components $V_{xx} < V_{yy} < V_{zz}$ and is defined along a Principal Axis System (PAS). The z component of the EFG is parallel to the magnetic field of the molecular frame[19] and is defined as $V_{zz} = eq$ (where q is the field gradient). The departure from axial symmetry is a measure of the distortion of the EFG and is expressed via the asymmetry parameter

$$\eta = (V_{xx} - V_{yy})/V_{zz} \qquad [1.3]$$

with values between 0 and 1 (where 0 is an axially symmetric EFG). The size of the quadrupolar interaction is the Quadrupolar Coupling Constant (QCC) is described as the product of the EFG and the quadrupolar moment:

$$QCC = e^2qQ/h \qquad [1.4]$$

η and the QCC can be derived via simulation of the NMR spectrum, providing a measure of the local environment. This can aid in detailing the overall structure of the system under study.

1.5.2 Zeeman Splitting

When nuclei with nucleus spin number greater than zero (I) are subjected to an external magnetic field (B_o), the spin states of the nuclear magnetic moment (μ) become non-degenerate and separate into distinct energy levels. This interaction is called the Zeeman interaction (fig 1.7). The Zeeman interaction can be described by the Hamiltonian [20]

$$H_z = -\mu \cdot B = -\gamma I_z B_o = -\omega_o I_z \qquad [1.5]$$

where γ is the gyromagnetic ratio describing the ratio between the nuclear angular momentum and the nuclear magnetic moment. When the two vectors are parallel, the sign is positive, and when antiparallel, negative.

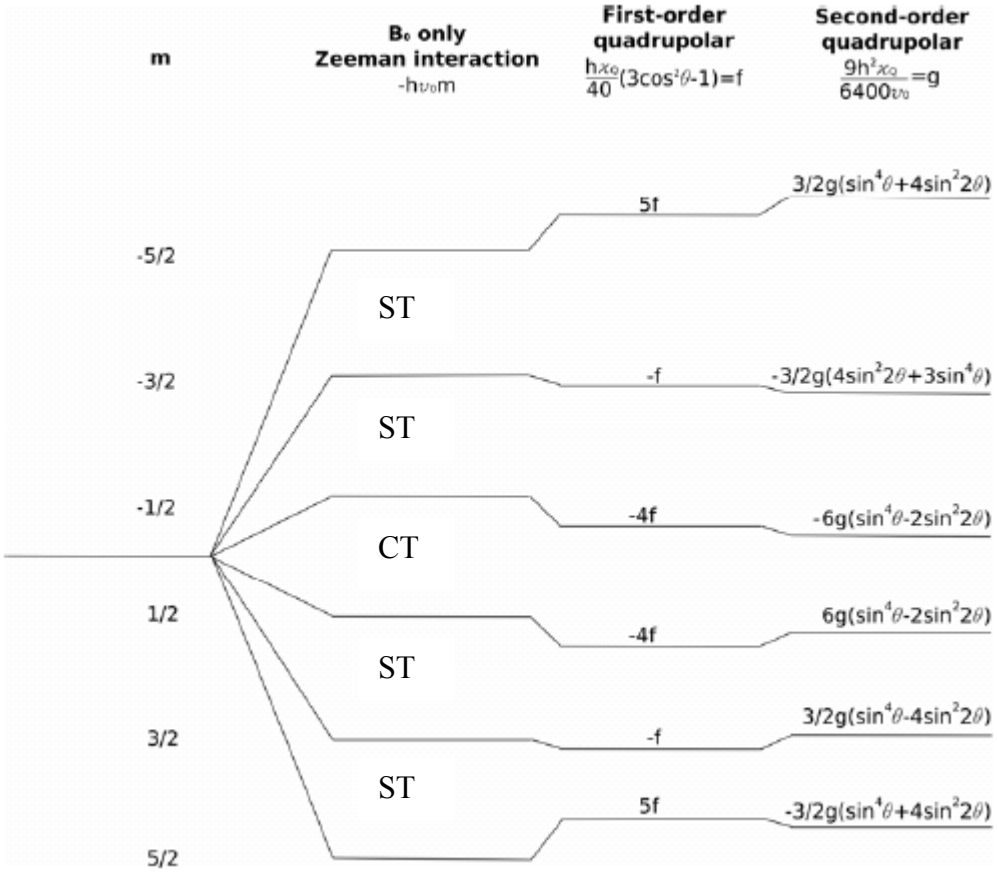

Figure 1. 14 Zeeman splitting diagram for spin 5/2 system showing non-degenerate spin states as a result of exposure to a magnetic field (B_0) separated by the Larmor frequency υ_0, which is dependent on magnetic field strength. First order quadrupolar interaction is shown for an axial system where the central transition (CT) is left unaffected, while the ST are affected. This interaction is orientation dependent and is zero when $\theta = 54.736°$ and $(3\cos^2\theta - 1) = 0$. For the second order quadrupolar interaction, the central transition is affected as well as the satellite transitions (ST). This interaction and is not completely removed under MAS conditions. In this figure, χ_q = QCC [1].

1.5.3 Quadrupolar Interaction and Magic Angle Spinning (MAS)

The 1st order quadrupolar interaction further shifts the Zeeman energy levels of the non- degenerate spin states of a nucleus. 1st order interactions are averaged out by MAS because it has an orientational dependence of $(3\cos^2\theta - 1)$. The 2nd order quadrupolar interaction further affects the differences in energy of the spin states. The 2nd order quadrupolar interactions have a different orientational dependence and are not completely averaged out by MAS. The effect of the 2nd order interaction is to broaden the spectral lines. The Hamilotonians describing first and second order splittings are given as [21]

$$H_Q^{(1)} = eQ/4I(2I+1)\hbar\ \sqrt{6}\ /3\ [3I_z^2 - I(I+1)]V_{(2,0)} \qquad [1.6]$$

$$H_Q^{(2)} = -\ 1/\omega_0 \left[\frac{eQ}{2I(2I-1)\hbar}\right]^2 \{\tfrac{1}{2}\ V_{(2,-1)}V_{(2,1)}[4I(I+1) - 8I_z^2 - 1] \qquad [1.7]$$

$$+\ \tfrac{1}{2}V_{(2,-2)}V_{(2,2)}[2I(+1) - 2I_z^2 - 1\ ]\}I_z \qquad [1.8]$$

$$\omega_o = \gamma B_o \qquad [1.9]$$

where, in the PAS $V_{(2,i)}$ are second rank spherical harmonics such that

$V_{(2,0)} = \sqrt{3/2}\,eq \qquad V_{(2,\pm1)} = 0 \qquad V_{(2,\pm2)} = \tfrac{1}{2}\,eq\eta$.

It can be seen from equation 7 that the 2nd order lineshape is inversely proportional to magnetic field strength. Therefore, a quantative measurement of the strength of the 2nd order interaction can be made by using different magnetic field strengths.

When the 2nd order interaction is the dominant interaction (and is not obscured by other interactions, such as distributions in chemical shift), line shapes observed can be simulated and the QCC and asymmetry parameter η can be calculated.

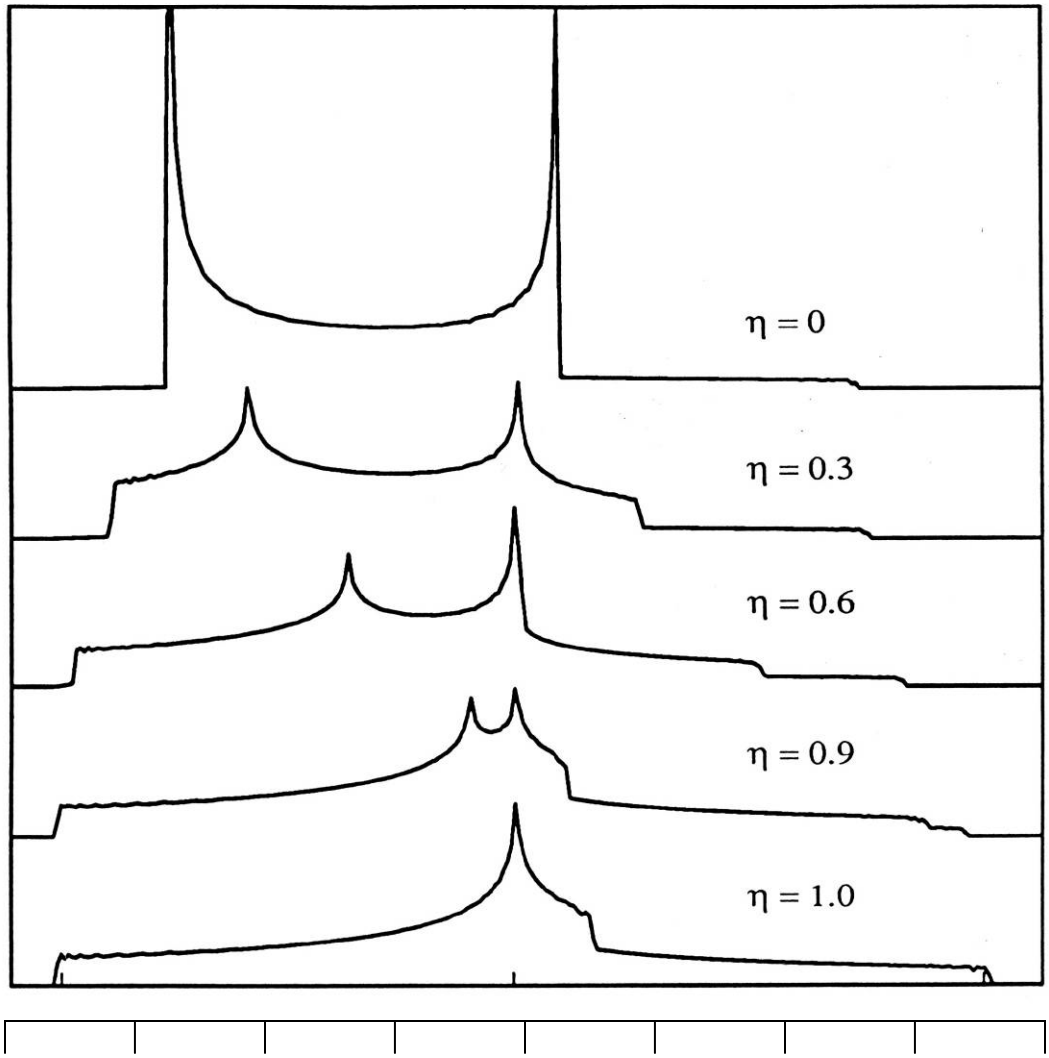

Figure 1. 15 The effect of varying the asymmetry η from 0 to 1. As η approaches 0, the environment about the nucleus has increasing axial distortion. Often these line shapes appear in a spectrum and can be fit using simulation software to extract both η and QCC [21].

The work presented in this dissertation uses these principles outlined here to help identify relationships between local and long range structures responsible for ionic conduction in solid electrolytes.

1.6 References

[1]. S.E Ashbrook; M.E. Smith, *Chem. Soc. Rev.* **2006,** 35, 718-735.
[2]. J.C. Boivin; G. Mairesse, *Chem. Mater.* **1998,** 10, 2870-2888.
[3]. S.C. Singhal, *Solid State Ionics* **2002,** 152-153, 405-410.
[4]. http://www.rise.org.au/info/Applic/Fuelcells/image018.png, In Long Island, NY, 2006.
[5]. http://www.doitpoms.ac.uk/tlplib/fuel-cells/printall.php, In 2006.
[6]. Y. Matsuzaki; I. Yasuda, *Solid State Ionics* **2002,** 152-153, 463-468.
[7]. T. Ishihara; H. Matsuda; Y. Takita, *J. Am. Chem. Soc.* **1994,** 116, 3801-3803.
[8]. H. Inaba; H. Tagawa, *Solid State Ionics* **1996,** 83, 1-16.
[9]. M. Hsu; L. Wu; J. Wu; Y. Shiu; K. Lin, *Electrochem. Solid-State Lett.* **2006,** 9, (4), A193-A195.
[10]. L. Smart; E.Moore, *Solid State Chemistry*. Second Edition ed.; Chapman and Hall: London, 1995.
[11]. A. R. West, *Solid State Chemistry and its Applications*. John Wiley and Sons: New York, 1984.
[12]. J.S. Benjamin, *Sci. Am.* **1976,** 234, 40.
[13]. A.E. Ermakov; E.E. Yurchikov; V.A. Barinov, *Fiz. metal metalloved* **1981,** 52, 1184.
[14]. J. Ding; W.F. Miao; P.G. McCormick; R. Street, *Appl. Phys. Lett.* **1995,** 67, 25.
[15]. S.E. Lee; J.M. Xue; D.M. Wan; J. Wang, *Acta Mater.* **1999,** 47, (9), 2633.
[16]. Q. Zhang; F. Saito, *Alloys Comp.* **2000,** 297, 99-103.
[17]. Abstracts In IV Int. Conf. on Mechanochemistry and Mechanical Alloying, Braunschweig, Germany, 2003.
[18]. D. B. Stojanovic, *J. Mater. Proc. Tech.* **2003,** 143-144, 78-81.
[19]. V.V. Zyryanov, *Inorg. Mater.* **2005,** 41, 378-392.
[20]. M. H. Levitt, *Spin Dynamics*. John Wiley and Sons: New York, 2001.
[21]. C. P. Slichter, *Principles of Magnetic Resonance*. 3rd ed.; Springer - Verlag New York, 1996.

Chapter 2:

^{17}O NMR studies of Local Structure and Phase Evolution for Materials in the $Y_2Ti_2O_7$ – $ZrTiO_4$ Binary System

^{17}O MAS NMR and XRD studies of precursor-derived $Y_{1.6}Zr_{0.4}Ti_2O_{7.2}$ and $Y_{1.2}Zr_{0.8}Ti_2O_{7.4}$ have been performed to investigate the development of local and long-range order in these materials as they evolve from a metastable amorphous state on heating. Zirconium titanate ($ZrTiO_4$) was also investigated to help interpret the ^{17}O NMR spectra of the ternary compositions. Consistent with earlier studies, crystallization was observed at 800 ºC to form a fluorite structure and a small amount of rutile; weak broad reflections were also observed which were ascribed to the presence of small pyrochlore-like ordered domains or particles within the fluorite phase. As the temperature was increased further, the sizes of these domains grew along with the concentration of rutile. At the highest temperature studied (1300 ºC), the reflections of the thermodynamic phases, pyrochlore and zirconium titanate ($ZrTiO_4$), dominated the XRD pattern. The ^{17}O NMR spectra revealed a series of different peaks that were assigned to different 3 and 4-coordinate O local environments. The data were consistent with the formation of a metastable phase $Y_{2-x}Zr_xTi_{2-y}Zr_yO_{7+x}$ with pyrochlore-like ordering but with Zr substitution on both cation sites of the pyrochlore structure. At low temperatures, doping on the A (Y^{3+}) sites predominates (i.e., x>y), consistent with the fact that the pyrochlore develops out of a more disordered fluorite-like, phase. As the temperature is raised, the Zr doping on the A site decreases and the metastable phase at this temperature can now be written as $Y_{2-x'}Zr_{x'}Ti_{2-y'}Zr_{y'}O_{7+x'}$ (i.e., $x' < y'$); TiO_2 is also observed, consistent with this suggestion. At high temperatures, doping on the B site decreases and the resonances due to the stoichiometric pyrochlore yttrium titanate ($Y_2Ti_2O_7$) dominate the NMR spectra. Weaker ^{17}O NMR resonances due zirconium titanate ($ZrTiO_4$) are also observed.

2.1 Introduction

Ternary oxides of general formula $A_2B_2O_{7+\delta}$, (with, for example, A, B = Y^{3+}, Ti^{4+}, Zr^{4+}), have been shown to exhibit moderate-to-good oxygen ion conductivity [1]. Applications of these and related materials range from oxygen sensors and electrodes, to electrolytes for solid oxide fuel cells (SOFCs) [2]. Many $A_2B_2O_7$ oxides adopt either the pyrochlore or fluorite structure depending on the sizes of the A and B cations, but fluorite can sometimes occur metastably in materials that form pyrochlores, if the materials are doped and/or synthesized at low homologous temperatures [3, 4]. Cation doping in $Y_2Ti_2O_7$ has been studied by using techniques such as X-ray diffraction (XRD), thermo-gravimetric analysis (TGA), differential scanning calorimetry (DSC), transmission electron microscopy (TEM) and MAS NMR [3, 5-8].

Neutron diffraction studies of the $Y_2Ti_2O_7 – Y_2Zr_2O_7$ quasi-binary examined the pyrochlore-to-fluorite transition, as well as the relationship between cation mixing on the A and B sites and the occupancy of the vacant O3 site of the pyrochlore structure [8][7] . ^{17}O MAS NMR spectroscopy was subsequently used by N.Kim *et al* [5] to investigate the local structure in this binary system.

A recent study by Schaedler et al [3] described the phase evolution of initially amorphous, precursor-derived compositions along the $Y_2Ti_2O_7 – Y_2Zr_2O_7$ and $Y_2Ti_2O_7 – Zr_2Ti_2O_8$ ($ZrTiO_4$) tie lines. The approach involved heat treating samples of the amorphous mixed oxides at different temperatures and characterizing the transformation products with XRD, TEM and DSC [3]. Pyrochlore, fluorite, $ZrTiO_4$ and rutile phases were all observed depending on the starting composition and the heat treatment used during synthesis, the results providing insight into the metastable phase evolution in $YO_{1.5}$-TiO_2-ZrO_2 system. This current paper reports results from a ^{17}O MAS NMR study of local structure for two compositions of general formula $Y_{2-x}Zr_xTi_2O_{7+x}$, where x = 0.2 (10 mole% ZrO_2, denoted 10Zr) and 0.4 (20Zr), in the $Y_2Ti_2O_7 – Zr_2Ti_2O_8$ tie line. Amorphous samples of these compositions were prepared by sol-gel routes and heated at various temperatures in order to follow the changes in local structure in the metastable phases that occur on heat treatment, and to relate the changes in local structure to the long – range structural rearrangements.

2.1.1 Structures

The pyrochlore structure (space group $Fd\bar{3}m$), adopted by the end-member $Y_2Ti_2O_7$, is derived from the fluorite structure, but the cations, ($A^{3+} = Y^{3+}$) and ($B^{4+} = Ti^{4+}$), are ordered on two different crystallographic sites (Figure 1(a)) resulting in a doubling of the cell parameters over those of fluorite. This cation ordering results in three different possible sites for oxygen O1, (1/8, 1/8, 1/8; Wyckoff position 8a), O2 (x, 1/8, 1/8; 48f) and O3, (3/8, 3/8, 3/8; 8b). These oxygen sites are all four coordinated, but are associated with distinct anion coordination environments $O2A_4$, $O1A_2B_2$ and $O3B_4$. Here, and throughout the paper, the notation $OM_xM'_y$ indicates that the oxygen anion is coordinated to $x$$M^{n+}$ and $y$$M'^{n'+}$cations in its 1st coordination shell. The O3 site is not occupied in a stoichiometric pyrochlore such as $Y_2Ti_2O_7$, but may sometimes be partially occupied on cation doping (e.g., in $Y_2Ti_{2-x}Zr_xO_7$) [6, 8], [4]. In the more disordered fluorite structure ($Fm\bar{3}m$ space group), adopted by for example $Y_2Zr_2O_7$, the oxygen atoms are similarly tetrahedrally-coordinated, but a range of local environments $OA_{4-x}B_x$ will be present.

The structure of the material with nominal composition $ZrTiO_4$ is more complex, since the ordering and stoichiometry of this compound are strongly affected by pressure, the presence of other metal cation dopants, and thermal history. $ZrTiO_4$ has a structural phase transition at just below 1200 °C. The high temperature form of Zr TiO_4 belongs to space group *Pbcm* [9] and adopts the α-PbO_2 structure, wherein the cations are completely disordered over one crystallographic site. The Zr:Ti ratio in this phase is not fixed, the possible deviations from the ideal 1:1 stoichiometry, increasing as the temperature is raised above the phase transition.[10] α-PbO_2 is structurally related to fluorite, the ions shifting to form distorted, edge-sharing MO_6 octahedra [11] which form a zigzag pattern along the c axis (Figure 2.1b) [12]. The cations order below 1200 °C, the extent of ordering depending on the cooling rate from the disordered state, and any

cation doping. The cation ordering results in the formation of alternating double slabs with Ti-Ti-Zr-Zr-Ti-Ti-Zr-Zr sequences along the c direction[9]. A Zr deficient material $Zr_5Ti_7O_{24}$ is similarly derived from the α-PbO_2 structure, with almost complete ordering to form alternating single Zr and double Ti-rich slabs Ti-Ti-Zr-Ti-Ti-Zr [10]. High resolution TEM studies of ordered materials close to the nominal $ZrTiO_4$ composition, showed that Ti-Ti-Zr- and Ti-Ti-Zr-Zr- blocks can coexist, the single slabs existing as uniformly distributed faults within the structure, and resulting in regions with Zr:Ti ratios of less than 1.[9] A recent, ambient temperature phase diagram for the ZrO_2-TiO_2 binary reported by Troitzsch *et al.* [10] reveals even more complexity and explains why exsolution of TiO_2 and baddeleyite can sometimes be seen on rapid cooling. [13]. An ordered phase with a close to 1:1 stoichiometry is stable between approximately 1160 and 1080 ºC, while below this temperature, the ordered phase with a composition close to that of $Zr_5Ti_7O_{24}$ (in equilibrium with Ti^{4+}-doped ZrO_2) represents the thermodynamic phase.

2.1.2 Local Structure and NMR Spectroscopy

To aid in the interpretation of the NMR spectra of these materials, the local environments present in these phases need to be considered. The neutron diffraction results for $Zr_5Ti_7O_{24}$ showed that the oxygen atoms of the ordered phase remain 3-coordinate in between the Ti-Ti slabs, but a displacement of the oxygen environments in between the Ti and Zr slabs occurs so that the OTi_2Zr local environment is coordinated to a fourth Zr at a slightly longer distance, forming an OTi_2Zr_2 environment (Figure 2.1c) and 8-coordinate Zr ions. Although no neutron diffraction data is available for any partially-ordered (metastable) $ZrTiO_4$ materials, it seems likely that similar displacements of the oxygen atoms may occur, if domains containing Zr slabs are present, similarly resulting in $O(M,M')_4$ environments, in addition to the $O(M,M')_3$ environments found in the disordered α-PbO_2 phase. However, a relatively recent Zr and Ti EXAFS study of the crystallization of phases with this composition, below the order-disorder transition, does not show any evidence for the formation of Zr coordination environments of higher than 6 [14].

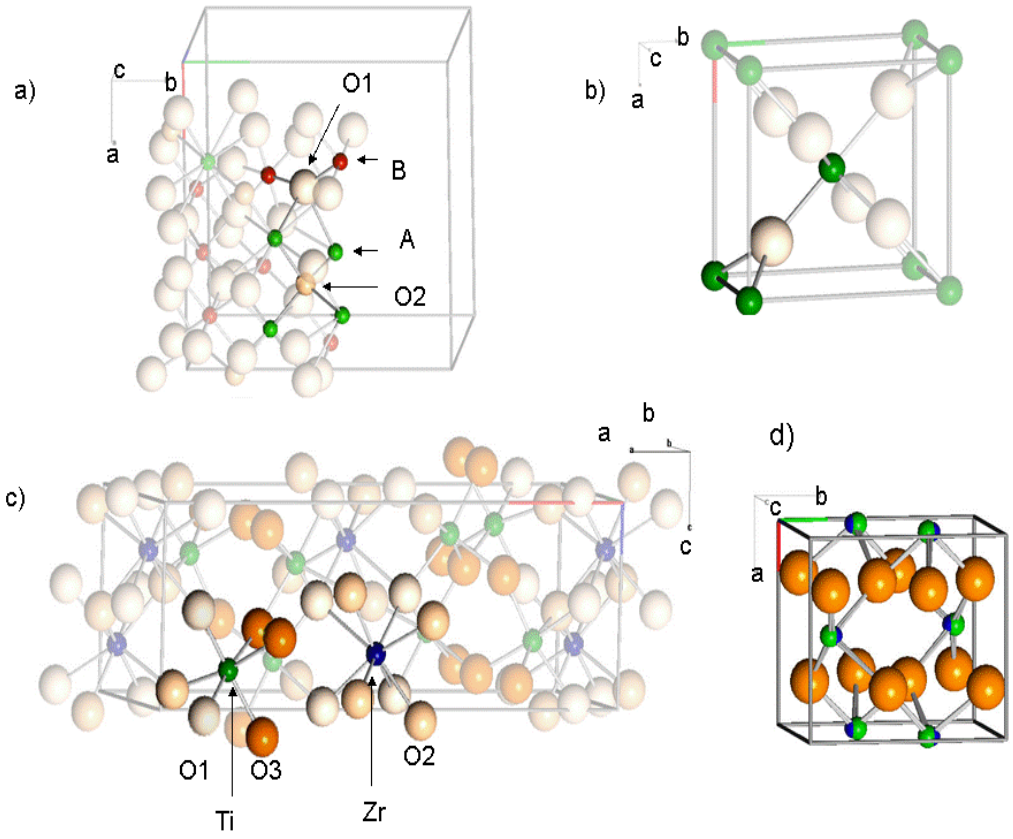

Figure 2. 10 a) Pyrochlore structure showing the two local oxygen environments O1A2B2 and O2A4. b) Room temperature structure of rutile. The local OTi3 environment is shown along with the unit cell (Ti small spheres, oxygen large sphere), c) The unit cell of the partially ordered $Zr_5Ti_7O_{24}$ structure; the 6 coordinate Ti and 8 coordinate Zr are highlighted. d) The high temperature (α-PbO_2) structure of $ZrTiO_4$.

The ^{17}O MAS NMR spectra of some of the phases relevant to this investigation have been reported [5], the results demonstrating that the ^{17}O chemical shift of the different local environments in these solids depends strongly on both the oxygen coordination number and the nature of the directly bound cations. The pyrochlore $Y_2Ti_2O_7$ contains two distinct, sharp resonances at 457 and 385 ppm, which are assigned to the two tetrahedrally-coordinated oxygen sites $O2Y_4$ and

$O1Y_2Ti_2$, with associated multiplicities of 1:6 (O1:O2). Rutile has a single ^{17}O NMR resonance with a reported shift of 588 ppm [15], corresponding to the trigonally-coordinated O local environment OTi_3 (see Figure 2.1b). The ^{17}O NMR spectrum of $ZrTiO_4$ has yet to be reported. Possible impurities in $ZrTiO_4$ are monoclinic ZrO_2 (Baddeleyite), which contains 3- and 4-coordinate local environments with associated ^{17}O NMR resonances at 401 and 324 ppm, respectively [15], and tetragonal ZrO_2, which contains a single OZr_4 local environment which resonates at 376 ppm. The results are consistent with the general observation that oxygen atoms in lower coordination environments resonate at higher frequencies [5, 16, 17]

Introducing dopants on the cation sites can create different local environments for oxygen, despite the oxygen occupying the same crystallographic site in the lattice. If these environments occur randomly within the sample, these will not directly visible by XRD. For example, the ^{17}O NMR spectrum of the fluorite $Y_2Zr_2O_7$ contains a very broad resonance centered at about 360 ppm, which corresponds to the single crystallographic site of fluorite [5]. The broadening arises from the presence of different local environments, $OY_xZr_{4-x,}$ in this compound each with slightly different chemical shifts. In the 10 Zr and 20 Zr compounds, there are several possible local oxygen environments that should, in principle, resemble local environments in related structures. The chemical shifts of the various relevant local environments were estimated in our previous ^{17}O study on pyrochlores [5]. Based on these results, it is clear that a substitution for Ti by Zr (or Y) in the local environments $OTi_{3-x}Y_x$ (or $OTi_{3-x}Zr_x$) will result in an approximately additive shift in the ^{17}O NMR resonance to lower frequency, by approximately 36 ppm per Y^{3+} substitution (and slightly more for Zr^{4+} substitution) for the pyrochlore materials. The results are summarized in Table 2.1, in order to help in the subsequent interpretation of the NMR data.

Local Environment	OTi_3		OY_2Ti_2	OY_4	OY_2Zr_2	OZr_4		OZr_3
Material	Rutile	Anatase	$Y_2Ti_2O_7$	$Y_2Ti_2O_7$	$Y_2Zr_2O_7$	t-ZrO_2	m-ZrO_2	m-ZrO_2
Shift (referenced to $H_2{}^{17}O$, ppm)	588 [15]	557 [15]	457 [5]	385 [5]	360 [5]	376 [15]	324 [15]	401 [15]

Table 2. 4 Summary of the ^{17}O shifts of different O local environments from references 15 and 5.

In this work, XRD and ^{17}O MAS NMR were used to examine both long range structure and the local environments surrounding the oxygen atoms for the two compositions: 10 and 20Zr. ^{17}O MAS NMR spectra of rutile and $ZrTiO_4$ are first presented to help the subsequent analysis of the local order that arises in the first coordination sphere of oxygen in the two compounds under investigation, 10Zr ($Y_{1.6}Zr_{0.4}Ti_2O_7$) and 20 Zr ($Y_{1.2}Zr_{0.8}Ti_2O_7$). The results from these studies are described in the context of the earlier study by *Schaedler et al* [3].

2.2 Experimental

The syntheses of $Y_{1.2}Zr_{0.8}Ti_2O_7$ (20Zr), $Y_{1.6}Zr_{0.4}Ti_2O_7$ (10Zr) and $ZrTiO_4$ (ZT) are identical to those described earlier. [3]. A reverse co-precipitation method was used, with precursors yttrium nitrate, titanium iso-propoxide and zirconium n-butoxide, mixed in iso-propanol (HPLC grade) in stoichiometric amounts. The resultant solution was added drop-wise to aqueous ammonium hydroxide at a constant pH of 10. The pH was maintained by simultaneous addition of NH_4OH. The resultant precipitates were filtered, dried, ground using a mortar and pestle and pyrolyzed at 700°C for 1hr at 10°C/min. Heat treatments (summarized in Table

2.2) were performed by preheating the furnace and placing the samples, contained in open alumina crucibles in the furnace at 800°C/1hr, 1000°C/5hrs and 1300°C/5hrs. These samples are labeled with the following notation 10Zr800, indicating that the 10Zr sample was heated at 800 °C. The 10Zr, 20Zr and ZT samples, as well as a sample of rutile TiO_2 (Alfa Aesar, 99.99% purity,[catalogue # 14631]), were then enriched with $^{17}O_2$ gas (50% concentration $^{17}O_2$, Isotec) by heating the samples at 550 - 600°C for 24 hrs in a sealed Pyrex vacuum tube. A second set of samples was prepared by heating the pyrolyzed sample in a sealed quartz tube with enriched $^{17}O_2$ gas. The sealed quartz ampoule was placed in a room temperature furnace and heated to 1000°C over 5hrs then allowed to cool to room temperature. The $ZrTiO_4$ precursor was first heated for 1hr at 700°C to induce crystallization, and subsequently enriched with $^{17}O_2$ gas in a sealed quartz tube by heating to 1000 °C overnight. The heat-treatment and $^{17}O_2$-enrichment protocols for all the samples are listed in Table 2.2. A Rigaku Miniflex XRD bench top X-ray diffractometer was used to assure sample purity both before and after enrichment for all samples.

Compound Stoichiometry	**Label**	**Heat Treatment (C) in air**	**^{17}O enrichment technique (24hrs)**
10Zr	10Zr 800	800/1hr	Evacuated Pyrex tube 550°C
	10Zr 1000	1000/5hrs	Evacuated Pyrex tube 550°C
	10Zr 1300	1300/5hrs	Evacuated quartz tube 1000°C
20Zr	20Zr 800	800/1hr	Evacuated Pyrex tube 550°C
	20Zr 1000	1000/5hrs	Evacuated Pyrex tube 550°C
	20Zr 1300	1300/5hrs	Evacuated Pyrex tube 550°C
$ZrTiO_4$	ZT 700	700/1hr	
	ZT 1000		Evacuated quartz tube 1000°C

Table 2. 5 Heat treatment and ^{17}O enrichment technique for the studied compounds.

^{17}O MAS NMR experiments were performed with a double or triple resonance 4mm MAS Chemagnetics probes on either an Infinity Plus 360 MHz or 500 MHz spectrometer operating at 48.8 or 67.7 MHz respectively, with a rotor spinning speed of 15 kHz. One pulse and Hahn echo ($\pi/2 - \tau - \pi - \tau$) pulse sequences were used with solid $\pi/2$ pulses of 1.3μs. The ^{17}O reference was $H_2{}^{17}O$ (10% ^{17}O, Isotec.) which was set to 0 ppm. Spectral deconvolution was performed with the NUTS software.

2.3 Results

2.3.1 Model Compounds

The spectrum of rutile is dominated by a single isotropic resonance at 589 ppm with a line width of ~720Hz, which is assigned to the OTi_3 local environment shown in Figure 1a, consistent with the shift reported in earlier studies (588 ppm) [15].

XRD revealed that the $ZrTiO_4$ amorphous precursor had crystallized upon heat treatment at 700°C/1h, in agreement with our earlier report [3] and other sol gel studies of this composition [14]. The XRD pattern for the sample heated at 700°C/1h and then at 1000°C/5hrs (ZT1000, Fig 2.2) shows reflections due to $ZrTiO_4$ and small amounts of rutile and baddeleyite (monoclinic ZrO_2) second phases, consistent with earlier observations [13]. A sharp resonance is observed in the ^{17}O MAS NMR spectrum of ZT1000 (Figure 2.3) at approximately 594 ppm, which is close to the isotropic resonance of rutile, and is therefore assigned to the OTi_3 local environment in the excess rutile phase.

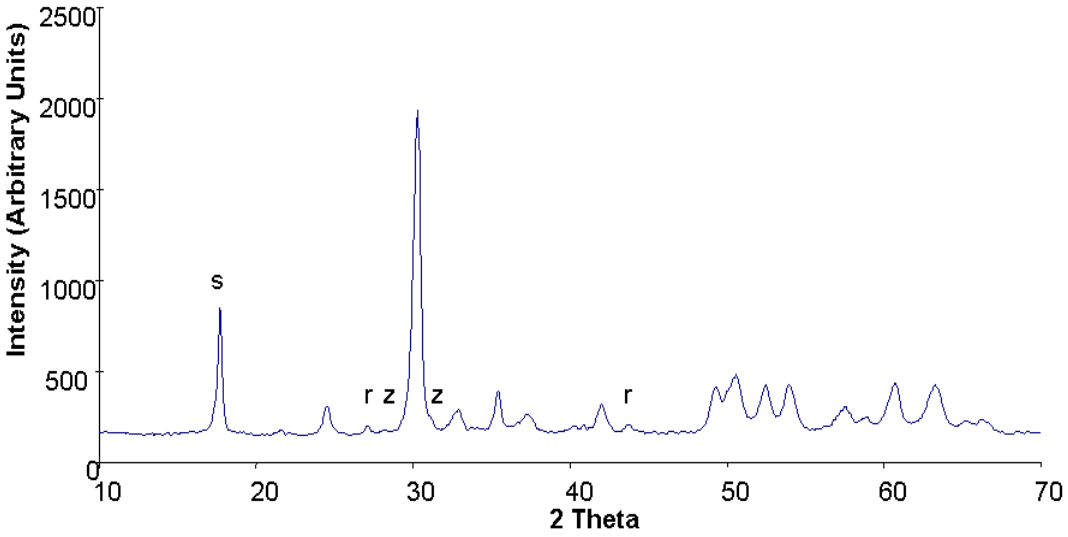

Figure 2. 11 XRD pattern of $ZrTiO_4$ post $^{17}O_2$ gas enrichment at 1000°C. Rutile and monoclinic ZrO_2 are indicated as R and Z respectively and the Teflon sample holder as S.

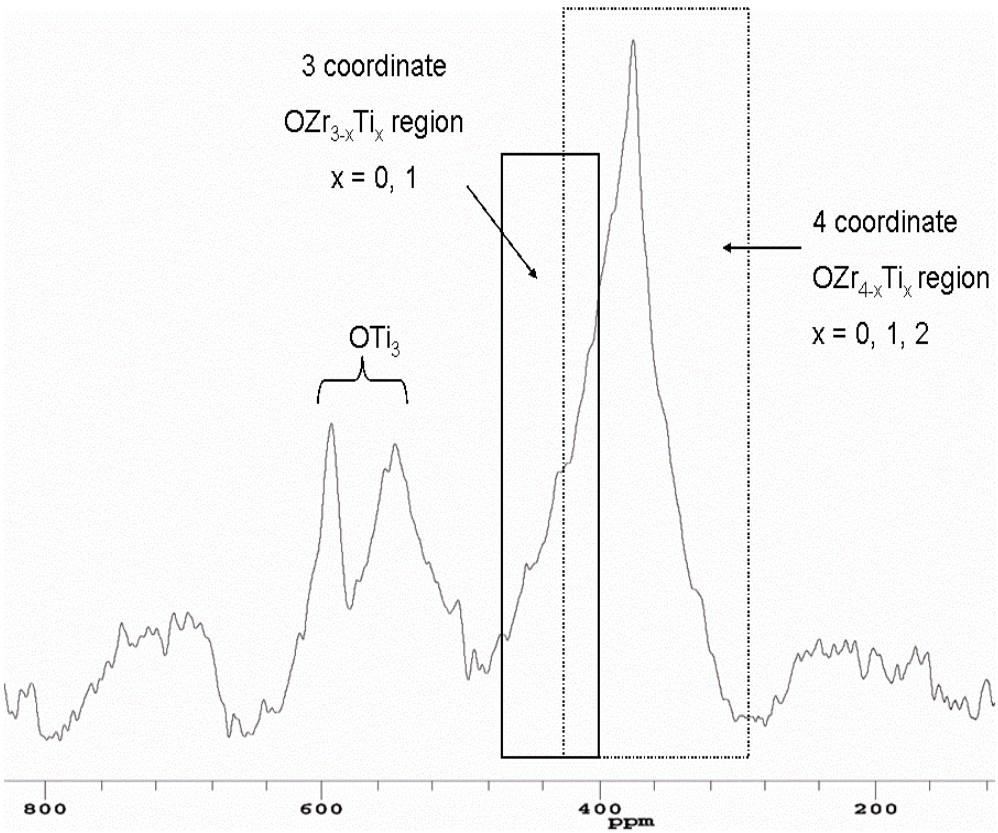

Figure 2. 12 ^{17}O MAS NMR 1 pulse spectrum of $ZrTiO_4$ heated to 1000°C (ZT1000) collected at 8.45T with a 4mm rotor at a spinning speed of 15 kHz.

The resonance at 564 ppm is assigned to a second OTi_3 oxygen environment, which is present in the Ti rich double layers in ordered $Zr_5Ti_7O_{24}$ and is likely to be present at least to some degree in $ZrTiO_4$ prepared at 1000 ºC which may show local ordering. The average OM_3 (M = Zr, Ti) environment in the high temperature form of $ZrTiO_4$ has a different local geometry than in rutile, presumably accounting for the slightly different chemical shift for this environment. The O-Ti-O bond angles in rutile (figure 2.1b) are 90° x 4, 98° x 2 and 81° x 2 where the O_3Ti are in a trigonal planar arrangement [18], whereas the O-Ti-O bond angles in $ZrTiO_4$ range between 83 and 102° and the O_3Ti group is no longer planar. The Ti is displaced slightly out of the plane formed by the 3 oxygen atoms lowering the symmetry [19], increasing the distortion of the local environment of oxygen. The increased breadth of resonance relative to that from rutile is ascribed to a range of distortions for the OTi_3 local environment.

All the other 3 and 4-coordinate local environments in ZT1000 must be contained within the broad envelope that spreads from approximately 460 – 320 ppm. The maximum of this broad resonance (374 ppm) occurs at the same

chemical shift as the OZr_4 environment in t-ZrO_2 but at higher frequency than the same environment in m-ZrO_2 (Table 2.1). Resonances at frequencies of ≤374 ppm are therefore consistent with environments such as OZr_3Ti and OZr_4, which are predicted to resonate at approximately 360 and 324 ppm, respectively, based on the shifts seen for m-ZrO_2 [15] and those for the pyrochlores and fluorites listed in Table (2.1). Since both Ti-for-Zr substitution in the O coordination sphere, and a lower coordinate environment result in a shift to positive frequencies (Table 2.1), components of the lineshape at even higher frequencies are ascribed to increased Ti substitution or to lower O coordination environments. Not all the (theoretically) possible local environments (e.g., OTi_2Zr, $OTiZr_2$, OZr_3, OZr_3Ti, OZr_2Ti_2, $OZrTi_3$) are present. High concentrations of Ti-rich or low coordinate environments such as $OZrTi_3$ and $OZrTi_2$ can be excluded, which are expected to resonate at >450 and approx. 500 ppm, respectively (assuming additive shifts for these local environments). Interestingly, this is consistent with the structure of $Zr_5Ti_7O_{24}$, where the structural distortion transforms the OZr_2Ti environment into an OZr_2Ti_2 environment.

2.3.2 Heat treatment of 10Zr:

The long-range structures of $Y_{1.6}Zr_{0.4}Ti_2O_{7.2}$ observed following different heat treatments, as detected by XRD (Figure 2.4), are given in Table 3, while the NMR spectra are shown in Figure 5. The XRD patterns reveal that the amorphous phase has crystallized by 800°C and that the fluorite and rutile structures are clearly present at this temperature (Figure 2.5).

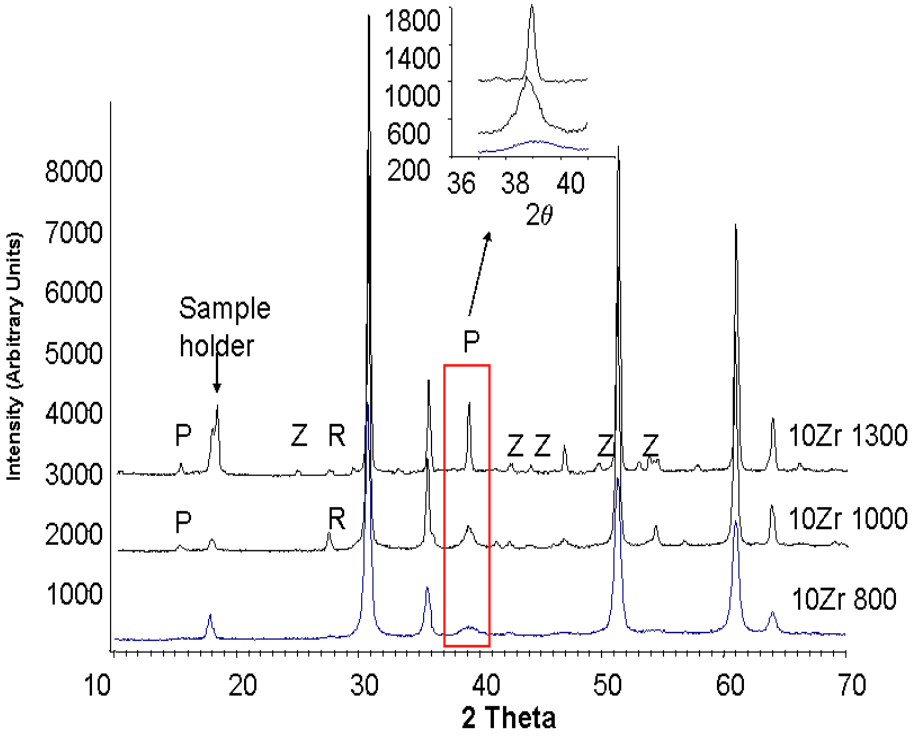

Figure 2. 13 XRD of the 10Zr series using CuKα on the Rigaku bench top diffractometer. Inlay shows the evolution of the pyrochlore peaks. (P = pyrochlore, R = rutile, Z = $ZrTiO_4$, S=Teflon sample holder).

	$^{17}O_2$ Enrichment	10 Zr	20 Zr
800 (°C)	before	f? + p + r (vw) 5.2 nm	f? + p + r(w) n/a
	After (550°C)	f? + p + r (vw) 30	f? + p + r(w) n/a
1000 (°C)	before	p + r 9.6 nm	p + r + z 11 nm
	After (550°C)	p + r 47	p + r + z 34 nm
1300 (°C)	before	p + r(w) + z(vw) 24 nm	p+ r(vw) + z >60 nm
	After (1000 °C)	p + r(w) + z(vw) > 60 nm	p+ r(vw) + z >60 nm

Table 2. 6 Phases seen from XRD. Average particle sizes shown are calculated using the Debye - Scherrer formula. At 1300 °C, the line widths of the reflections are governed by the instrumental resolution. (f = fluorite, p = pyrochlore, r = rutile, z = ZrTiO4, vw = very weak, w = weak).

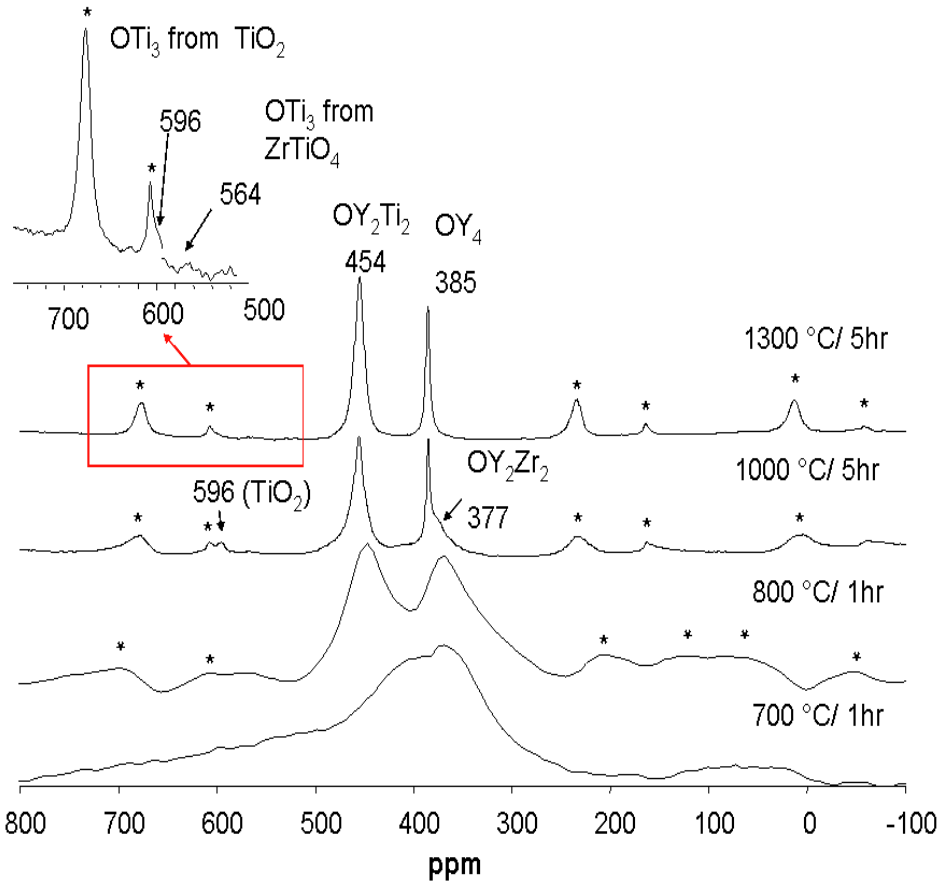

Figure 2. 14 ^{17}O MAS NMR 1 pulse spectra of $Y_{1.6}Zr_{0.4}Ti_2O_{7.2}$ (10Zr series) from amorphous, 800°C, 1000°C, and 1300°C shown (from bottom to top), collected at 11.6T. Asterisks indicate spinning sidebands.

The broader reflection at 39° corresponds to the 331 reflection of the pyrochlore structure and suggests that some cation ordering has already occurred at this stage. Based on the full width at half height (FWHM) line width of this reflection, the average size of the pyrochlore domains is estimated to be approximately 10 nm. The size of the domains grows slightly on annealing at 550 °C in $^{17}O_2$. At 1000°C, the pyrochlore and rutile phases are clearly visible by XRD and NMR, and the size of the pyrochlore domains has grown to ~8 nm. (41 nm after annealing in $^{17}O_2$). The results suggest that the coherence length scale of pyrochlore-like ordering increases with annealing time. The unit cell parameters were extracted from the reflections common to both the pyrochlore and fluorite phases and vary from 10.06, 10.12, to 10.08 Å for 10Zr800, 1000 and 1300, respectively. Following heat-treatment at 1300°C, the sample is dominated by the pyrochlore phase but also contains weak reflections due to $ZrTiO_4$ and very weak reflections due to rutile.

The NMR spectra of the 10Zr series in Figure 2.5 are in qualitative agreement with the XRD data. Starting with the spectrum that easiest to interpret, i.e., that of 10Zr1300, two dominant resonances are observed at 454 and 385 ppm

which are assigned to the $O1Y_2Ti_2$ and $O2Y_4$ local environments of the pyrochlore structure in Fig. 1a [5]. Neither of these resonances can be fit by a single Lorentzian or Gaussian lineshape and both show evidence of broader components in their baselines indicating some residual disorder in the pyrochlore phase. The inset to the spectrum of 10Zr1300 shows an enlargement of the higher frequency region where weak characteristic resonances due to TiO_2 and $ZrTiO_4$ are observed.

At 1000°C, the pyrochlore (455 and 385 ppm) and rutile (596 ppm) phases are clearly visible by NMR as well as the superstructure reflection in the XRD (Figures 5 and 4). A broader resonance at approx. 377 ppm is also observed in the NMR spectra, along with a weaker broad resonance at 411 ppm; these can be seen more clearly in Figure 2.6.

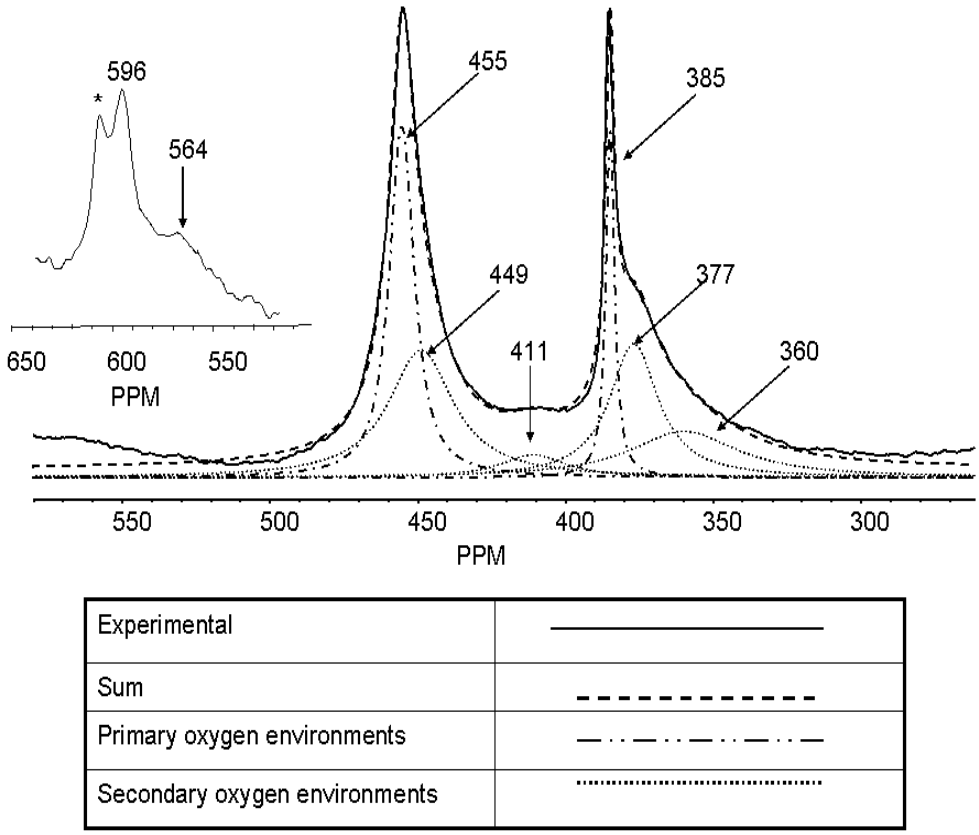

Figure 2. 15 Deconvolution of the two main ^{17}O NMR resonances of the 10Zr 1000 spectrum showing the contribution of the different oxygen local environments to the spectrum. An expansion of the higher frequency region is shown as an inset.

Earlier work by Kim et al. suggests that substitution of Y^{3+} by Zr^{4+} in the oxygen local coordination sphere of environments $OY_{4-x}Zr_x$ in Zr^{4+}-doped $Y_2Ti_2O_7$ results

in small ^{17}O NMR shifts to lower frequencies of approximately 7 – 10 ppm per Zr^{4+} for Y^{3+} replacement. Much larger shifts to higher frequency are expected when Ti^{4+} substitutes for Y^{3+} in the O local coordination shell. Since the new resonance at 411 ppm lies intermediate between the $O2Y_4$ and $O1Y_2Ti_2$ resonances (Table 2.1), we tentatively ascribe it to $OY_{3-x}Zr_xTi$, i.e., a 4-coordinate O resonance, most likely in the pyrochlore phase, containing only one Ti^{4+} in its local coordination sphere and 3 Y^{3+}/Zr^{4+} ions. The lower frequency resonance at 377 ppm is very close in chemical shift to both the main resonance seen in $ZrTiO_4$ in the sample prepared under similar temperature conditions and the $OZrY_3$ environment in a pyrochlore (approx. 373 ppm). A weak, broader resonance is also observed at 564 ppm, which is likely associated with the OTi_3 environment in $ZrTiO_4$, indicating that local environments in this phase must also contribute to the intensity of the 377 ppm resonance. Presumably, the sizes of the crystallites are too small to allow the $ZrTiO_4$ phase to be detected by XRD at this temperature. A weaker resonance due the OTi_3 environments of rutile is seen at 596 ppm. Deconvolution of resonances found in the spectral region from 550 – 300 ppm suggests that there may also be additional very broad resonances to lower frequencies of the main pyrochlore peaks, at approx. 450 and 360 ppm. These resonances are present in the 10Zr800 (fig 2.5) spectrum with much higher intensities and are tentatively assigned to environments such as OY_2Ti_2 (450 ppm) and OY_2Zr_2 and OY_3Zr in the 360 ppm region.

Two resonances dominate the spectrum of 10Zr 800 (fig 2.5) with chemical shifts close to those found for $Y_2Ti_2O_7$, although the two sets of resonances are much broader and have shifted to lower frequencies (447 and 368 ppm, Figure 2.7).

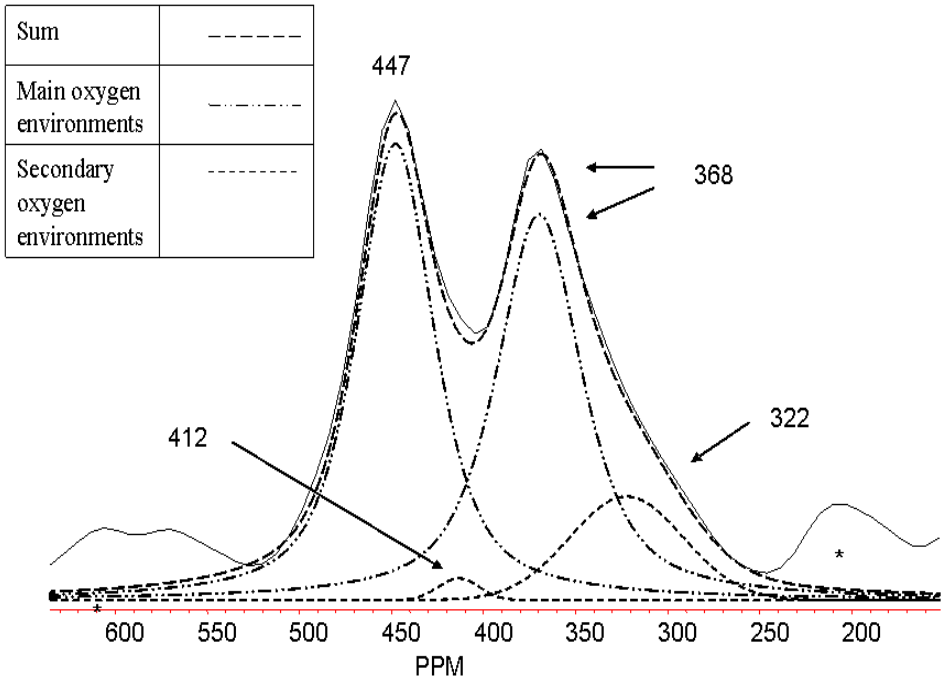

Figure 2. 16 Deconvolution of the 10Zr 800 spectrum showing two main oxygen environments and 2 secondary environments.

Again, the resonance at 368 ppm is assigned to Ti-free local environments such as OY_3Zr and OY_2Zr_2; these environments have very similar shifts (approx. 373 and 360 ppm [5]) and it is therefore difficult to resolve them. Deconvolution of the lineshape (fig 2.7) suggests that at least one more resonance at even lower frequencies (approx 322 ppm) is required to reproduce the lineshape. Based on the shift for the 4-coordinate environment in monoclinic-ZrO_2 at 324 ppm [15], this resonance is assigned to the OZr_4 local environment. The much weaker resonance at 412 ppm is assigned to $OY_{3-x}Zr_xTi$.

The ^{17}O NMR spectrum of the amorphous material (fig 2.5) is dominated by two overlapping resonances at approximately 420 and 370 ppm, which are tentatively assigned to $OY_{3-x}Zr_xTi$ and OY_2Zr_2, respectively. Both these resonance are broad, suggesting that other Ti-deficient local environments (e.g., OY_3Zr and $OYZr_3$) are present. A very broad resonance to higher frequency is observed which is ascribed to the Ti-rich environments (e.g., OTi_3 or OTi_2Zr/Y).

2.3.3 Heat treatment of 20Zr:

The phases seen by XRD for the $Y_{1.2}Zr_{0.8}Ti_2O_{7.4}$ composition are similar to those seen for 10Zr at the three temperatures studied (800°C/1h, 1000°C/5h, 1300°C/5h) (figure 2.8; Table 2.2). However, the pyrochlore phase is relatively less well developed at 800 and 1000°C, and the reflections due to $ZrTiO_4$ are more intense at 1300°C, consistent with the higher concentration of Zr in this sample. Weak reflections due to t-ZrO_2 are also observed at 1000°C. The ^{17}O NMR spectra of the $Y_{1.2}Zr_{0.8}Ti_2O_{7.4}$ series are shown in figure 2.9.

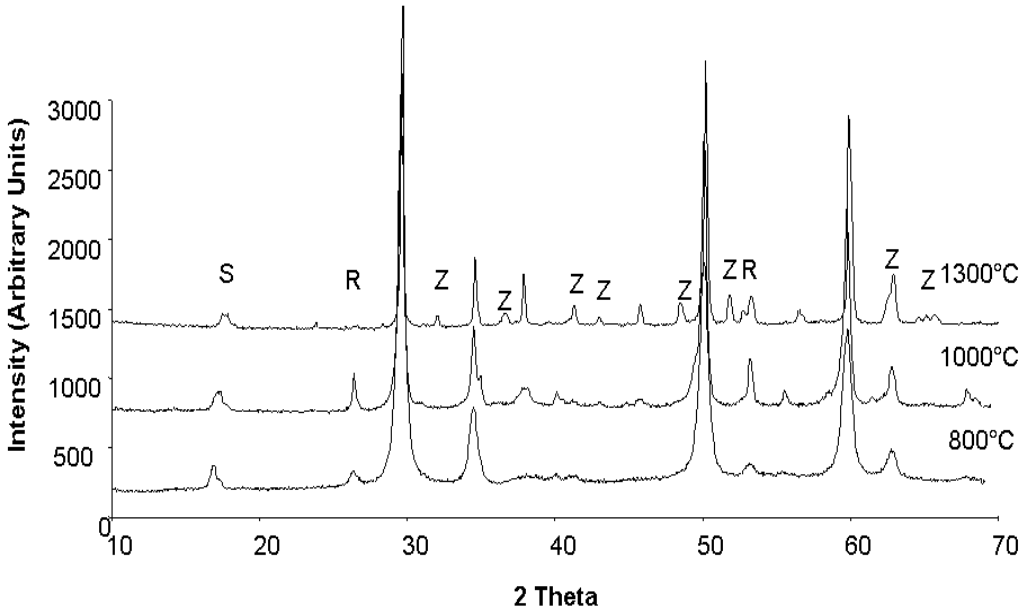

Figure 2. 17 XRD patterns of the 20Zr series. S = sample holder, R = rutile, Z = $ZrTiO_4$.

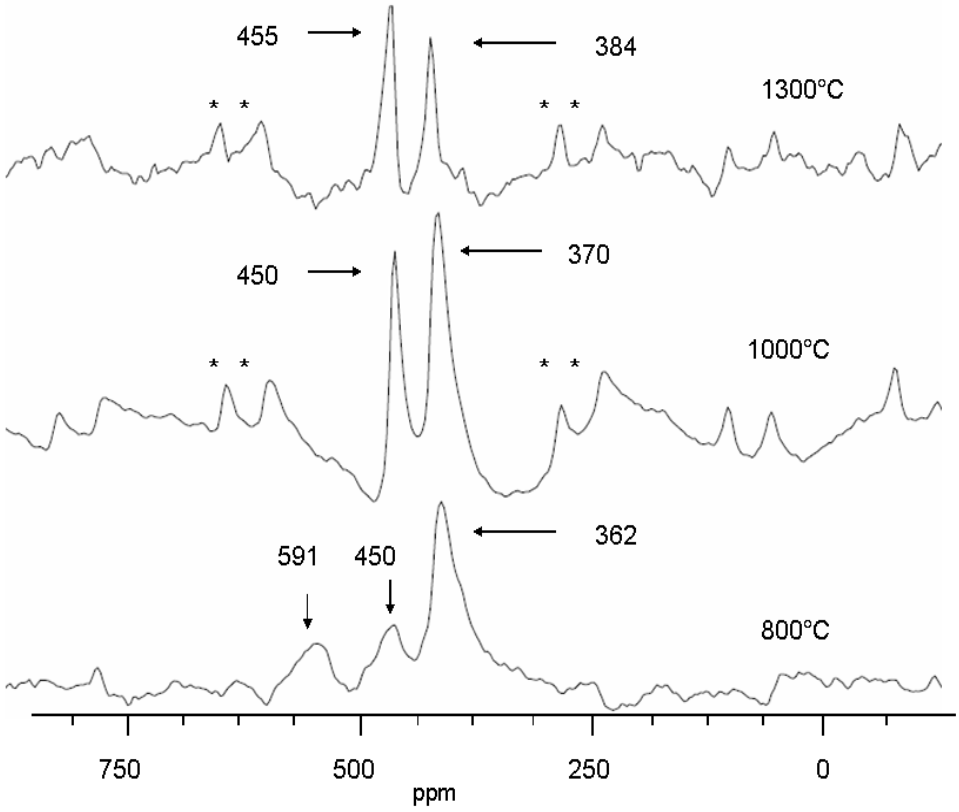

Figure 2. 18 ^{17}O MAS NMR spectra collected at 8.45T for the 20 Zr series ($Y_{1.2}Zr_{0.8}Ti_2O_{7.4}$); top to bottom, heat treatment at 1300°, 1000°, and 800°C. Asterisks indicate 1st order spinning sidebands.

All three data sets contain similar isotropic resonances as the 10Zr spectra; however there are some noticeable differences. The resonances in all three spectra of the 20Zr series are broader, relative to the 10Zr series. The signal-to-noise (S/N) of these spectra is also worse than those for 10Zr, in part due to the broader resonances. For the sample annealed at 1300 ºC, the poorer S/N is also ascribed to the different enrichment method (see Table 2.2). Other causes of the decrease in S/N include different sample volumes used in the enrichment process, oxygen-leaks in the enrichment system and poorer oxygen-mobility in the higher Zr containing samples (leading to difficulties in enrichment). The spectrum of the material at 800°C exhibits 3 main isotropic resonances at 591 (OTi_3), 450 ($OYZrTi_2$) and 362 ppm (OY_3Zr and OY_2Zr_2). At 1000°C, the lowest frequency resonance has shifted to 370 ppm, and subsequently to 384 ppm at 1300°C. This is consistent with a decrease in the Zr concentration in the local coordination shell, with 384 ppm corresponding to the $O2Y_4$ local environment. The resonance due to t-ZrO_2 (Table 2.1) in the spectrum of 20Zr1000 is presumably contained in the 370 ppm

resonance. The S/N of these spectra are too poor to allow the $ZrTiO_4$ and TiO_2 resonances to be identified unambiguously at higher temperatures.

2.4 Discussion

The evolution of the long-range structures was summarized in Table 2.2; the implications from NMR concerning the doping of the cations within these phases and the extent of ordering will now be explored. Not until 10Zr and 20Zr are heated to ~ 800°C for an hour are crystalline structures observed by diffraction and well resolved resonances seen in the NMR spectra. The observation of small pyrochlore domains by diffraction (approx. 3 and 15 nm, before and after ^{17}O enrichment), and the similarity of the ^{17}O NMR spectrum to that of the ordered pyrochlore phase seen at higher temperature, suggest that small domains of pyrochlore-like ordering are present at 800 °C and above. Sharp peaks are present for the reflections that are characteristic to both the fluorite and pyrochlore phases indicating that peak broadening is not a consequence of small particle sizes, and that on a longer length-scale, the lattice is fluorite-like. The 10Zr spectrum is dominated by two resonances that are assigned to the local environments $OZrYTi_2$ and OY_2Zr_2. Given the pyrochlore-like ordering, these resonances must originate from the O1 ($O1A_2B_2$) and O2 ($O2A_4$) sites, in the pyrochlore structure. Only a very weak resonance due to the O2 local environment OY_2TiZr (411 ppm) is observed in the spectrum of 10Zr800, which would arise from substitution of the B site by Zr. This indicates that Zr predominantly substitutes for Y on the A site of the pyrochlore structure, in the small pyrochlore domains that are present at low temperature. This forms a metastable phase with composition $(Y_{2-x}Zr_x)(Ti_{2-y}Zr_y)O_{7+x}$ (x>y). The 20Zr spectra are also consistent with this hypothesis, since the $OZrYTi_2$ and OY_2Zr_2 resonances are similarly observed at this temperature. As the material is heated further to 1000 °C, the environment $OY_{3-x}Zr_xTi$ is now observed clearly for 10Zr (the signal-to-noise of 20Zr spectrum is not good enough to allow more detailed analysis). This indicates that the Zr ions have now substituted for Ti in the B site to form $Y_2Ti_{2-y}Zr_yO_7$, either due to movement of Zr ions from the A to the B site, (some) Zr remaining in the structure, or preferential removal of Zr from the A sites and, thus, from the structure. The former proposal will be accompanied by Ti removal from the pyrochlore domains; this is consistent with the observation of rutile by both NMR and XRD in higher concentrations. The latter proposal is supported by the emergence of a tetragonal zirconia phase in 50Y-20Zr in the XRD patterns, suggesting that both mechanisms occur for the 20Zr sample. In 10Zr, the smaller Zr concentrations of Zr ions can probably be accommodated by moving them from the A to B sites (preferred by Zr^{4+} due to its valence and size), which is accompanied by Ti removal from the B sites, consistent with the appearance of a rutile phase. As the temperature is increased to 1300 °C, more Zr is rejected from the structure and phases such as $ZrTiO_4$ are seen more clearly by XRD, although this phase was detected at 1000 °C by NMR for 10 Zr.

The variations in occupancies of the different ions in the different sites of the pyrochlore structure are consistent with the lattice parameters of the phases

(derived from the full set of reflections from pyrochlore and fluorite). The smallest lattice parameter (1.006nm) is estimated observed for 10Zr800 ($Y_{2-x}Zr_xTi_{2-y}Zr_yO_{7+x}$ (x>y)), consistent with the substitution of the smaller Zr^{4+} ion (ionic radius 0.206 nm) for Y^{3+} (0.212 nm) on the Y^{3+} site. As Zr^{4+} is removed from this site, forming $Y_2Ti_{2-y'}Zr_{y'}O_7$, the lattice parameter increases to 1.012 nm, due to both substitution of Zr^{4+} for the much smaller Ti^{4+} ion on the B site (and the accompanying elimination of Ti^{4+} from the structure), and the removal of Zr^{4+} from the A site. Assuming no residual substitution of Zr on the A site, a lattice parameter of 1.012 is consistent with a value for y of approximately 0.2 [7]. Finally, the lattice parameter drops again to 10.08 Å, as the Zr^{4+} concentration on the pyrochlore B site decreases and $ZrTiO_4$ is precipitated. A similar trend was observed for 20Zr. Interestingly, the unit cell parameters derived for the pyrochlore superstructure reflections are similar (within error) to those estimated for the whole set of fluorite + pyrochlore reflections (1.004 (±0.002) nm, 1.010 (±0.002) for 1.007 (±0.001) for 800, 1000 and 1300 Zr, respectively. This further suggests that the pyrochlore is ordering out of a fluorite phase rather than being present as a separate, distinct phase. The NMR spectrum of the amorphous phase (10Zr700) suggests that Ti rich and Ti-poor local environments are present. This suggests that Y and Zr rich fluorite like domains may even be starting to form in the nominally amorphous material, along with regions more rich in Ti, which may explain why the pyrochlore phase that crystallizes at low temperatures contains Zr-doping on the Y (A) site. However, it is important to stress that our NMR experiments are only probing structure in the 1st cation coordination shell, so it is not possible to determine the extent of any compositional variations in the amorphous phase.

2.5 Conclusions

A combination of XRD and solid state NMR has been used to investigate the crystallization of samples with compositions $Y_{1.6}Zr_{0.4}Ti_2O_7$ and $Y_{1.2}Zr_{0.8}Ti_2O_7$. The results provide insight into the phase evolution (from the amorphous to crystalline state) observed in this system, which involves the formation of a series of metastable phases that differ in their extent of incorporation of Zr on the A and B sites of the pyrochlore $Y_2Ti_2O_7$. The first crystalline phase observed in this study has reflections that can by indexed as fluorite. Superstructure reflections are seen due to a metastable pyrochlore phase $Y_{2-x}Zr_xTi_{2-y}Zr_yO_{7+x}$, with a small domain size, which is derived from the stoichiometric pyrochlore $Y_2Ti_2O_7$, with Zr doping on the A (Y) and B (Ti) sites of the structure. At low temperatures, doping on the A sites predominates (i.e., x>y), consistent with the fact that the pyrochlore develops out of a more disordered Zr and Y rich fluorite-like precursor phase. As the temperature is raised, Zr is exsolved from the pyrochlore, primarily from the A site. The metastable phase at this temperature can now be written as $Y_{2-x'}Zr_{x'}Ti_{2-y'}Zr_{y'}O_{7+x'}$ (i.e., x' < y'); TiO_2 is also observed, consistent with this suggestion. This is in agreement with studies of the $Y_2Ti_2O_7 – Y_2Zr_2O_7$ tie line where the thermodynamically stable form of the Zr-doped pyrochlore phase $Y_{2-z}Zr_zTi_2O_7$ can accommodate Zr up to $z \geq 0.8$; the metastable phase in this tie line can tolerate even higher Zr dopings [5]. At high temperatures, essentially all the Zr is exsolved and the final thermodynamically stable phases, $ZrTiO_4 + Y_2Ti_2O_7$ are observed.

The paper clearly shows that a combination of the long-range probe of structure, XRD, can be combined with ^{17}O NMR to examine subtle structural changes in doping and in local ordering.

Note: This work has been previously published as J. L. Palumbo *et al.*; *J. Solid State Chem.* **2007**, 180, (7), 2175 - 2185

2.6 References

[1]. J.A. Kilner; R.J. Brook, *Solid State Ionics* 1982, 6, (3), 237-252.
[2]. J.C. Boivin; G. Mairesse, *Chem. Mater.* 1998, 10, 2870-2888.
[3]. T. A. Schaedler; W. Francillon; A. S. Gandhi; C. P. Grey; S. Sampath; C. G. Levi, *Acta Materialia* 2005, 53, 2957-2968.
[4]. C. Heremans; B.J. Wuensch, *J. Solid State Chem.* 1995, 117, 108-121.
[5]. N. Kim; C. P. Grey, *J. Solid State Chem.* 2003, 175, 110 - 115.
[6]. B.J. Wuensch, K.W. Eberman, C. Heremans, E.M. Ku, P. Onnerud, E. M.E. Yeo, S.M. Haile, J. K. Stalick, J. D. Jorgensen, *Solid State Ionics,* 2000, 129, 111-133
[7]. Y. Liu; R. L. Withers; L. Noren, *J.Solid State Chem.* 2004, 177, 4404.
[8]. B. J. Wuensch; K. W. Eberman; C. Heremans; E. M. Ku; P. Onnerud; E. M.E. Yeo; S.M. Haile; J. K. Stalick; J. D. Jorgensen, *Solid State Ionics* 2000, 129, 111-133.
[9]. P.K. Davies; R. Christofferson, *J. Am. Ceram. Soc.* 1992, 75, (3), 563-69.
[10]. U. Troitzsch; A.G. Christy; D.J. Ellis, *Phys. Chem. Minerals* 2005, 32, 504-514.
[11]. R.W. Lynch; B. Morosin, *J. Am. Ceram. Soc.* 1972, 55, (8), 409-413.
[12]. P. Bordet; A. McHale; A. Santoro; R. S. Roth, *J. Solid State Chem.* 1986, 64, 30 - 46.
[13]. U. Troitzsch; A.G. Christy; D.J. Ellis, *J. Am. Ceram. Soc.* 2004, 87, (11), 2058-2063.
[14]. J. Xu; C. Lind; A. P. Wilkinson; S. Pattanaik, *Chem. Mater.* 2000, 12, 3347 - 3355.
[15]. T.J. Bastow; S.N. Stuart, *Chem. Phys.* 1990, 143, 459-467.
[16]. P. J. Dirken, T. J. Bastow, . E. Smith, H. J. Whitfield, *J. Phys. Chem.* 1996, 100, 18539-18545.
[17]. M. E. Smith, T. J. Bastow, H. J. Whitfield, *J. Mater. Chem* 1992, 2, (9), 989 - 990.
[18]. E.P. Meagher; G.A. Lager, *Can. Min.* 1979, 17, 77-85.
[19]. R. E. Newnham, *J. Am. Ceram. Soc.* 1967, 50, 216.

Chapter 3:

^{17}O NMR Studies of the Fluorite to Pyrochlore Transition of Sol-gel Derived Compositions Along the $Y_2Ti_2O_7 - Y_2Zr_2O_7$ Binary

Abstract:

^{17}O magic angle spinning nuclear magnetic resonance (MAS NMR) and X-ray diffraction (XRD) have been used to study the crystallization of initially amorphous, sol-gel derived $Y_2Zr_{0.4}Ti_{1.6}O_7$, $Y_2Zr_{0.8}Ti_{1.2}O_7$, $Y_2Zr_{1.2}Ti_{0.8}O_7$ materials, which lie along the $Y_2Ti_2O_7$ - $Y_2Zr_2O_7$ tie line. The initial crystalline structure that forms is a fluorite. ^{17}O MAS NMR spectroscopy is in agreement with the XRD of the fluorite, as broad spectra are observed. As heating progresses, the fluorite structure transforms into the defect pyrochlore. The superstructure 331 pyrochlore peak starts to emerge in the XRD pattern, which is also suggestive of the beginning of cation ordering over the longer-range. Distinct regions in the ^{17}O NMR spectra show oxygen coordinated to specific cation arrangements, which are characteristic of the pyrochlore structure. At the highest temperature used in this study, XRD reveals increased ordering, the 331 peak increasing in intensity and the ^{17}O MAS NMR spectra being dominated by resonances due to pyrochlore-type local ordering.

3.1 Introduction

In chapter 2, substitution of Zr for Y was explored along the $Y_2Ti_2O_7$ – $Zr_2Ti_2O_8$ ($ZrTiO_4$) tie line of similar sol-gel derived amorphous oxides. XRD and ^{17}O NMR were used to observe pyrochlore, fluorite, rutile and $ZrTiO_4$ structures both at local and long – range levels of the compositions $Y_{1.6}Ti_2Zr_{0.4}O_{7.2}$ and $Y_{1.2}Ti_2Zr_{0.8}O_{7.4}$ [1]. It was shown that 10 and 20 mole % Zr substitution for the A site cation (Y) first crystallizes with fully developed fluorite reflections as well as a broad weak reflection of pyrochlore and weak reflections of rutile. Upon heating to 1000°C for 5h, the pyrochlore reflections further develop as do the reflections of rutile. Further heating to 1300°C for 5h continues to precipitate rutile as well as $ZrTiO_4$. These results suggest that Zr prefers B site occupancy, displacing Ti from the B site in the form of rutile and $ZrTiO_4$.

In this chapter, results are reported from a ^{17}O MAS NMR study of local structure for the composition of general formula $Y_2Zr_{2-x}Ti_xO_7$, where x = 0.4, 0.8, 1.2 (10, 20 and 30 mole% ZrO_2, denoted 10Zr, 20Zr, and 30Zr, respectively) in the $Y_2Ti_2O_7$ –Y_2 Zr_2O_7 tie line. Amorphous samples were prepared by sol-gel routes and heated at various temperatures in order to observe changes in local structure. As the metastable phases developed upon heat treatment, we were able to relate the changes in local structure to the long – range structural rearrangements as a function of heat treatment using XRD and ^{17}O NMR. Both the long-range structure, determined by XRD, and the local oxygen environments, as determined by ^{17}O NMR, have proven to be complementary techniques in elucidating the structural details of the cation ordering, and consequently, some of the subtleties of the overall structure. ^{17}O MAS NMR spectroscopy has been shown to distinguish oxygen environments with specific cation coordination [2-4]. In general, when oxygen is coordinated by different cations, oxygen resonances appear in distinct regions of the ^{17}O NMR spectra, a summary of which can be found in table 2.1. This fact aids in the interpretation of the spectra

which allows for a more detailed local picture of the oxygen coordination environments as the pyrochlore structure emerges. In this chapter, we found that the amount of Zr substituting for Ti strongly affects the degree of cation ordering. As the Zr content is increased, cation disorder becomes more prevalent, consistent with other studies [5-7]. The phase evolution from fluorite to pyrochlore structures is examined along the $Y_2Ti_2O_7 – Y_2Zr_2O_7$ binary tie line. The crystallographic structures are the same as those discussed in chapter 2.

T.A. Schaedler *et al* in 2005[8] explored the metastable evolution of pyrochlore structure as a result of a liquid precursor synthesis route. In their work, the fluorite structure occurred at Zr dopant levels as low as 10 mole % Zr at 800°C (fig 3.9). Upon further heating at 1300°C for 5 h, single phase pyrochlore was observed. In the same study, the same compound was heated at 1300°C for 300 h to achieve a thermodynamic equilibrium where the pyrochlore structure emerged. At 30 mole % Zr substitution, Schaedler *et al* found a single phase fluorite structure after heating at 1300°C for 6h. Further heating at 1300°C for 300h produced pyrochlore and fluorite as separate phases, where the pyrochlore was representative of the thermodynamic phase, in agreement with earlier studies of the thermodynamic phase by Heremans *et al* [6], and Y. Liu *et al* [7]. It is important to note that all of these studies used a liquid precursor route that achieved atomic level mixing and were heated sufficiently long (> 3 days at > 1300°C) to achieve the thermodynamic phase.

As the Zr content on the B site is increased in the pyrochlore structure, gradual occupancy of the normally vacant O3 site occurs. The occupancy of the O3 site approaches 50% at 30Zr and is filled from the next nearest neighboring O1 site [6]. The O1 site then to relaxes from the ideal position of (x 1/8 1/8) where x = 0.4625 Å for the pure pyrochlore, to x = 3/8 for the fluorite structure [6]. The thermal anisotropic displacement factor for the O1 site increases dramatically between 15 and 30 mole % substitution of Zr for Ti [6]. The partial occupancy of both the O1 and O3 sites as well as the increase in the thermal anisotropic displacement parameter suggest that ionic conduction occurs via hopping from the O1 to O3 sites in the pyrochlore structure [6].

Bastow *et al.* have shown that oxygen coordinated to Ti resonates at 588 ppm in rutile, where oxygen is in a trigonal planar arrangement with 3 Ti atoms [3]. When the local geometry changes such that the planar symmetry is broken but Ti remains 3 coordinate to oxygen, the shift changes by about – 30 ppm, as found in the Ti-O environment found in $ZrTiO_4$ [1].

For the systems studied here where there is pyrochlore-like ordering, gradual occupancy of the O3 site contributes toward line broadening in the ^{17}O NMR spectra. In the fully ordered pyrochlore, the O3 site is vacant. The effect of the increasing occupancy of the O3 site as increasing amounts of Zr are introduced into the system, tends to relax the coordinate of the O1 site, therefore changing the M-O bond length [5]. In addition to the gradual occupancy of the O3 site with increasing Zr content, the effect of larger Zr cation replacing the smaller Ti cation is to further distort the M-O bond length of the BO_6 [7], leading

further to a distribution of bond lengths which inevitably broadens the ^{17}O NMR spectrum.

Additional factors can determine the fluorite to pyrochlore transition. Different metastable states obtained by varying synthesis conditions can affect the kinetics of cation ordering. Solution routes to these compounds take advantage of atomic level mixing not found in the traditional solid state route. The product formed at low temperatures has a thoroughly mixed homogeneous cation distribution before the heat treatment. Deploying a subsequent mild heat regiment, the system is able to order in ways not always seen, resulting in unusual properties [9]. In principle, if cation ordering and structure can be controlled by use of metastable precursors, this opens the opportunity to tailor the material for specific functions with optimized performances.[10] These materials can sometimes be referred to as advanced materials. An 'advanced material' utilizes the "energize and quench" approach, capturing a material at room temperature that has not reached its lowest equilibrium state. This material can then be manipulated to optimize performance by slowly controlling the kinetics of the system.

3.2 Experimental:

The syntheses of $Y_2Zr_{0.4}Ti_{1.6}O_7$, $Y_2Zr_{0.8}Ti_{1.2}O_7$, $Y_2Zr_{1.2}Ti_{0.8}O_7$ (10Zr, 20Zr and 30Zr, respectively) are identical to those described earlier [8]. A reverse co-precipitation method was used, with precursors yttrium nitrate, titanium iso-propoxide and zirconium n-butoxide, mixed in iso-propanol (HPLC grade) in stoichiometric amounts. The resultant solution was added drop-wise to aqueous ammonium hydroxide at a constant pH of 10. The pH was maintained by simultaneous addition of NH_4OH. The resultant precipitates were filtered, dried, ground using a mortar and pestle and pyrolyzed at 700°C for 1hr at 10°C/min. Heat treatments were performed by preheating the furnace and placing the samples, contained in open alumina crucibles in the furnace at 800°C/1hr, 1000°C/5hrs and 1300°C/5hrs. The samples were then quenched in air. These samples are labeled with the following notation 20Zr800, indicating that the 20Zr sample was heated at 800 °C. The series were then enriched with $^{17}O_2$ gas (50% concentration $^{17}O_2$, Isotec) by heating the samples at 600°C for 24 hrs in a sealed Pyrex vacuum tube containing ~8mL of $^{17}O_2$. XRD was performed before and after $^{17}O_2$ enrichment on a Scintag diffractometer using Cu $K\alpha_1$ radiation to assure sample purity.

^{17}O MAS NMR experiments were performed with a double resonance 4mm MAS Chemagnetics probe on a 360 or 500 MHz spectrometer operating at 48.8 or 67.7 MHz respectively, with a rotor spinning speed of 15 kHz. One pulse and Hahn echo ($\pi/2 - \tau - \pi - \tau$) pulse sequences were used with solid $\pi/2$ pulses of 1.0μs with recycle delays of 1.0 s. The ^{17}O reference was $H_2{}^{17}O$ (10% ^{17}O, Isotec.) which was set to 0 ppm.

3.3 Results

The XRD of the compound 10Zr heated to 800°C (10Zr800) exhibits a diffraction pattern consistent with that of a pyrochlore structure (fig 3.1). The reflections of the fluorite structure are present as well as a relatively broad superstructure reflection at ~38° due to pyrochlore like ordering. The ^{17}O MAS NMR spectrum of this compound (10Zr800) in figure 3.2 reveals two main broad dominant resonances at 386 and 452 ppm which can be assigned to OY_4 and OY_2Ti_2 respectively. The featureless intensity between the two main resonances at 400 ppm suggests a high degree of cation disorder despite the suggestion of the two resonances reminiscent of the pyrochlore. For the 10Zr sample heated to 1000°C/5hrs, the superstructure reflection in the diffraction pattern (fig 3.1) at 38° becomes sharper and more intense suggesting more pyrochlore-like ordering relative to the same compound heated at 800°C/1hr (fig 3.1). The ^{17}O MAS NMR spectrum of 10Zr1000 (fig 3.2) again exhibits two main resonances at 452 ($O1Y_2Ti_2$) and 386 ($O2Y_4$) ppm. These two resonances are consistent with pyrochlore-like ordering. Although the relative intensities of the resonances are closer to that predicted for the O1 and O2 with a ratio of 6:1 (O1:O2), the breadth of the resonances continues to suggest disorder. In addition, a weak resonance at 343 ppm emerges. 4- coordinate oxygen coordinated to zirconium resonates at 325 ppm suggesting that this resonance is due to a locally Zr rich region. The spectrum of 10Zr1300 (heated at1300°C/5hr) is similar. The XRD of this material shows a superstructure reflection at 38° which has further increased in intensity and further narrows, again suggesting increased pyrochlore-like ordering relative to the low temperature treatments of this compound. The main resonances seen here are also at 452 and 386 ppm as well as the small resonance to lower frequency at 343 ppm. A subtle feature at 400 ppm suggests that another distinct oxygen environment may be present.

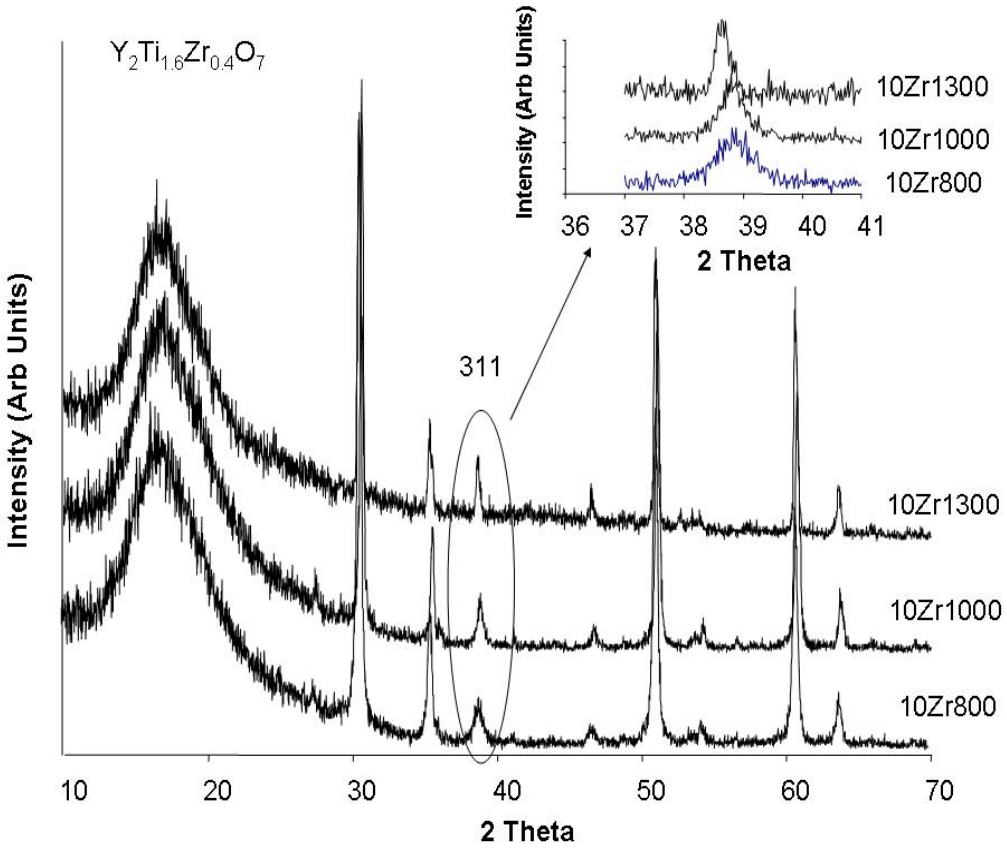

Figure 3. 11 XRD of $Y_2Ti_{1.6}Zr_{0.4}O_7$ (10Zr) at the various heat treatments. The XRD patterns collected using CuKα1 from a Rigaku diffractometer, show the pyrochlore superstructure emerging at ~38 deg for the three 10Zr samples in this study. The 1300°C sample exhibits a much more developed peak at the same 2 θ value. Diffraction patterns are shown post $^{17}O_2$ gas enrichment. The broad feature at ~18 degrees is background from the Teflon sample holder.

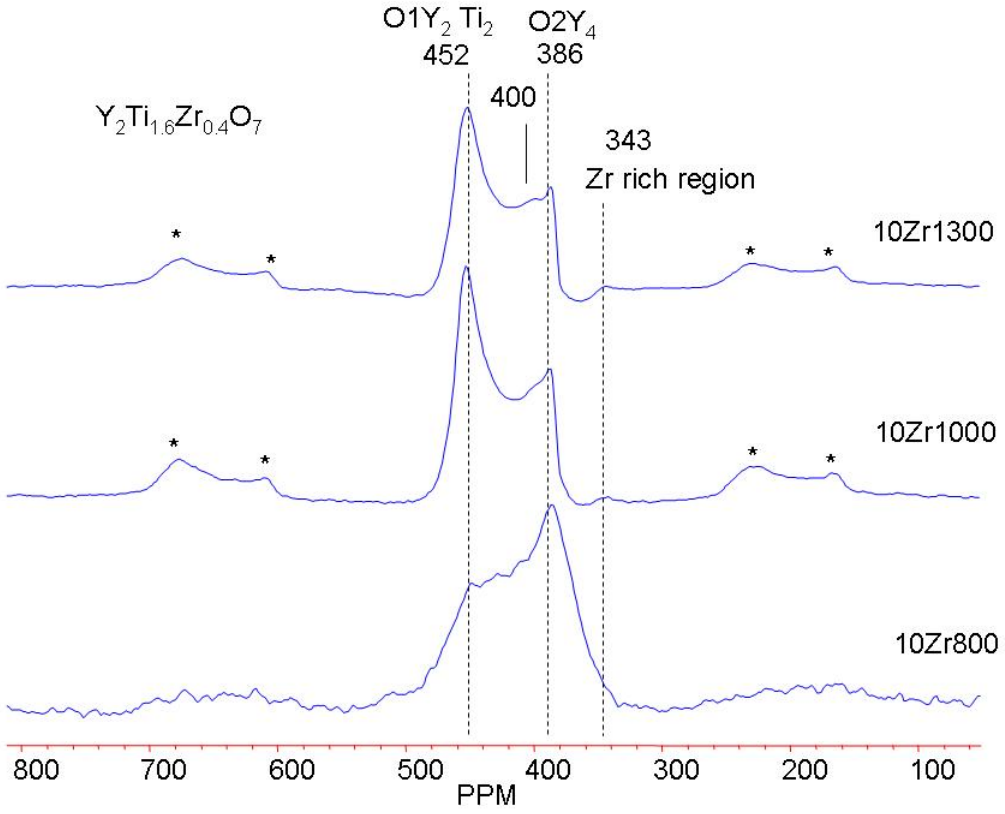

Figure 3. 12 ^{17}O MAS NMR of the $Y_2Ti_{1.6}Zr_{0.4}O_7$ (10Zr) composition heated at 800/1hr, 1000/5hr, and 1300°C/5hr (bottom to top) collected at 11.5T with a spinning speed of 15kHz using a Hahn echo where the 90° flip angle = 1.0μs (spinning side bands from the two main resonances are indicated by asterisks).

The XRD pattern for $Y_2Ti_{1.2}Zr_{0.8}O_7$ heat treated at 800°C/1hr (denoted as 20Zr800), exhibits a diffraction pattern of a fluorite structure (figure 3.3). No superstructure reflections are evident in 20Zr800 suggesting a complete random distribution of cations consistent with a fluorite structure. This is echoed in the ^{17}O NMR spectrum of 20Zr800 which exhibits a main, featureless resonance at about 380 ppm, consistent with multiple local environments expected in the disordered fluorite structure (figure 3.4).

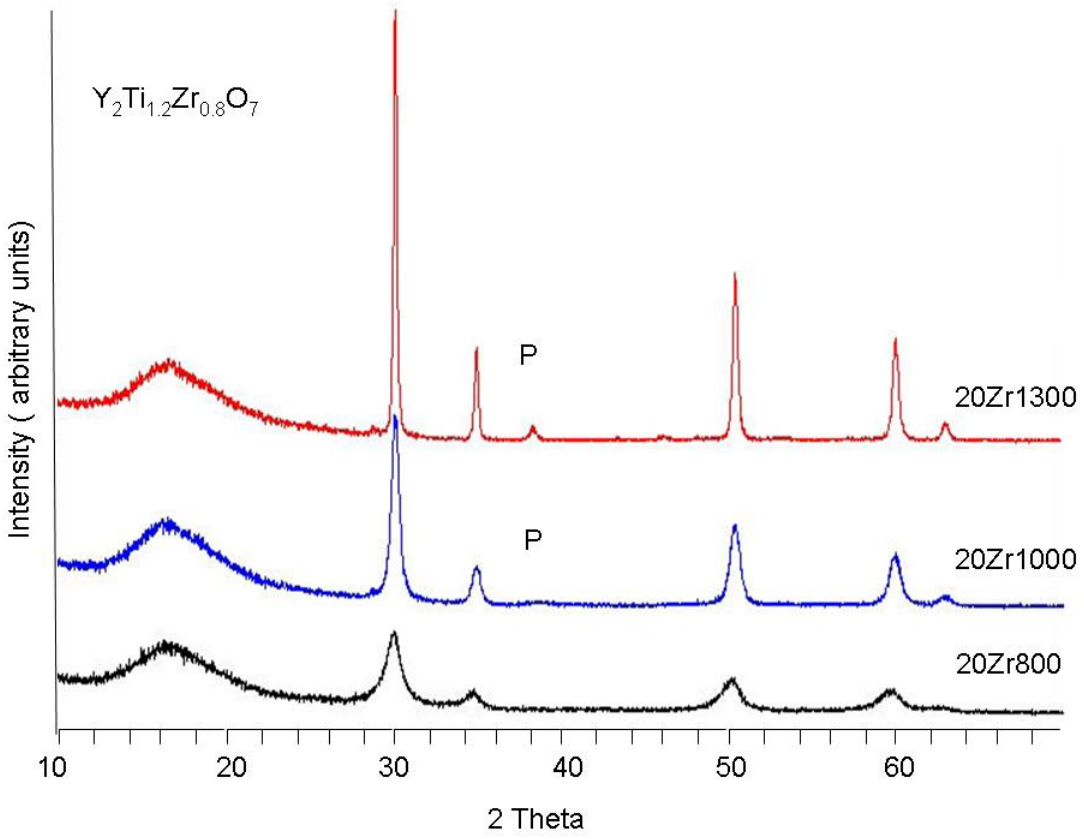

Figure 3. 13 XRD of $Y_2Ti_{1.2}Zr_{0.8}O_7$ (20Zr) after the various heat treatments. The XRD collected on the sample treated at 1000°C shows the beginning of the emergence of the pyrochlore phase at ~38 deg. The 1300°C sample exhibits a much more developed peak at the same 2 θ value. The broad feature at ~18 degrees is background from Teflon sample holder.

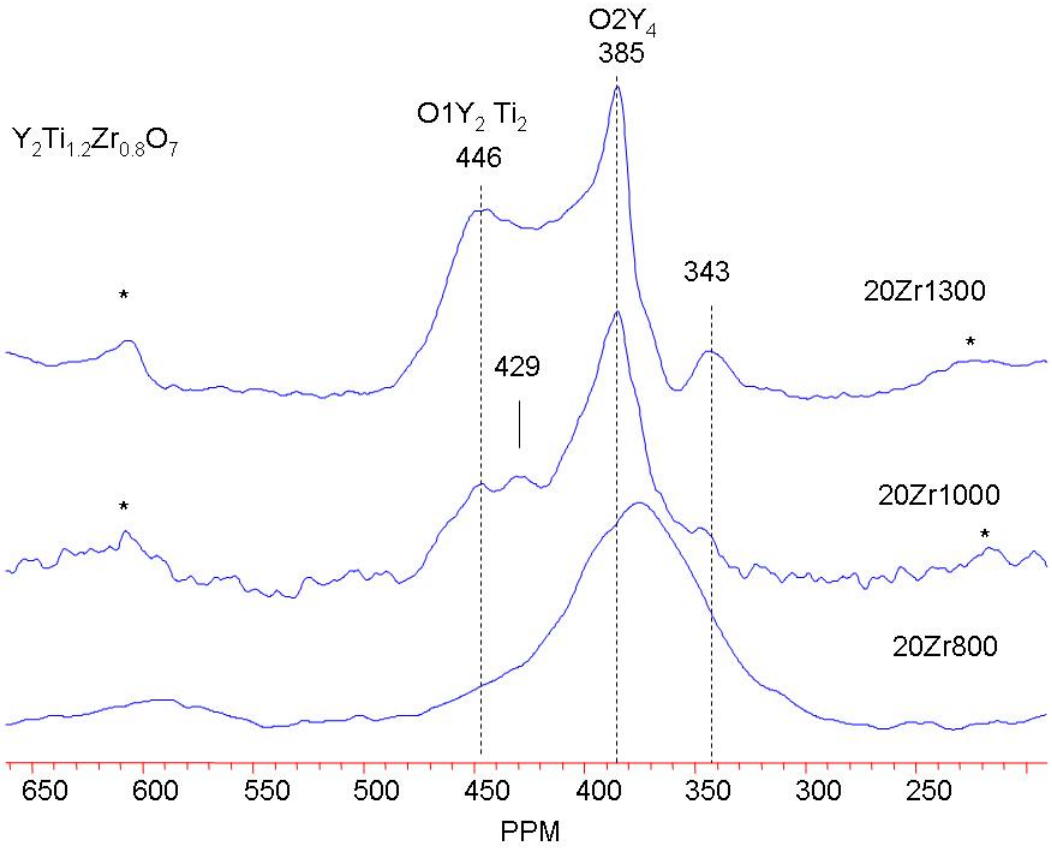

Figure 3. 14 ^{17}O MAS NMR of the $Y_2Ti_{1.2}Zr_{0.8}O_7$ (20Zr) composition heated at 800/1hr, 1000/5hr, and 1300°C/5hr (bottom to top) collected at 11.5T with a spinning speed of 15kHz (where the side bands are indicated by asterisks). The sample treated at 1000°C exhibits additional oxygen environments seen as peaks between 385 and 446 ppm.

In the XRD of the sample 20Zr1000 in figure 3.3, an emergence of the 331 reflection shows the onset pyrochlore ordering. The ^{17}O NMR of 20Zr1000 (fig 3.4) contains a main resonance at 385 ppm with additional resonances of approximately half the intensity at 429 and 446 ppm. As in the spectrum of the 10Zr1000 in figure 3.2, the 20Zr1000 spectrum in figure 3.4 has a feature at about 343 ppm. These 4 resonances indicate cation ordering with relatively large distributions in chemical shift. However, the two resonances in this spectrum at 446 and 385 ppm can be assigned to the pyrochlore environments, $O1Y_2Ti_2$ (446 ppm) and $O2Y_4$ (385 ppm).

For 20Zr1300, the XRD (figure 3.3) exhibits a reflection of the pyrochlore structure at ~38°, yet it is of low intensity, suggesting that the superstructure of the pyrochlore structure is evident yet not fully developed. The ^{17}O NMR spectrum of this compound (figure 3.4) confirms the ordering peaks of the XRD; 2 dominant resonances at 446 and 385 ppm representing the main oxygen environments of the pyrochlore ($O1Y_2Ti_2$ and $O2Y_4$, respectively). However, the

resonance at 343 ppm is also more intense, which is reminiscent of a Zr rich oxygen environment. The breadths of these resonances in the ^{17}O NMR spectrum of 20Zr1300 are broad; this is ascribed to a distribution in chemical shifts, because no significant 2nd order quadrupolar interactions were detected as determined from spectra acquired at two different magnetic field strengths.

When the sample containing 30 mole % of Zr is substituted for Ti ($Y_2Ti_{0.8}Zr_{1.2}O_7$) is heat treated at 800°C/1hr (30Zr800) the XRD exhibits a fluorite diffraction pattern with broad reflections as seen in figure 3.5. The ^{17}O NMR spectrum of this compound (30Zr800) resembles the 20 mole % substituted Zr compound heat treated at 800°C/1hr (20Zr800) in that it exhibits a single, broad resonance at about 380 ppm (figure 3.6).

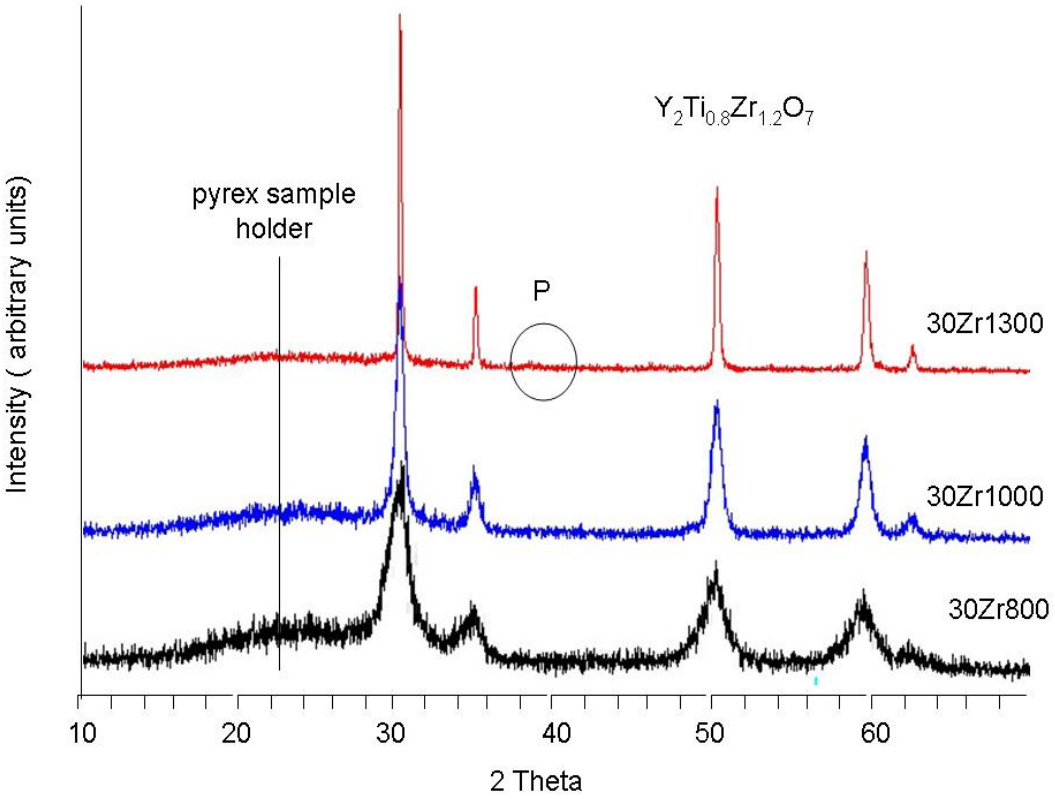

Figure 3. 15 XRD of $Y_2Ti_{0.8}Zr_{1.2}O_7$ at the various heat treatments (1300/5hr, 1000/5hr, 8001/hr, top to bottom). The XRD patterns collected on a Rigaku bench top diffractometer consistently show the pattern of a fluorite with increasing crystallinity as the heat treatment temperature increases. The broad reflections at low 2θ values (~22 deg) are from pyrex sample holder.

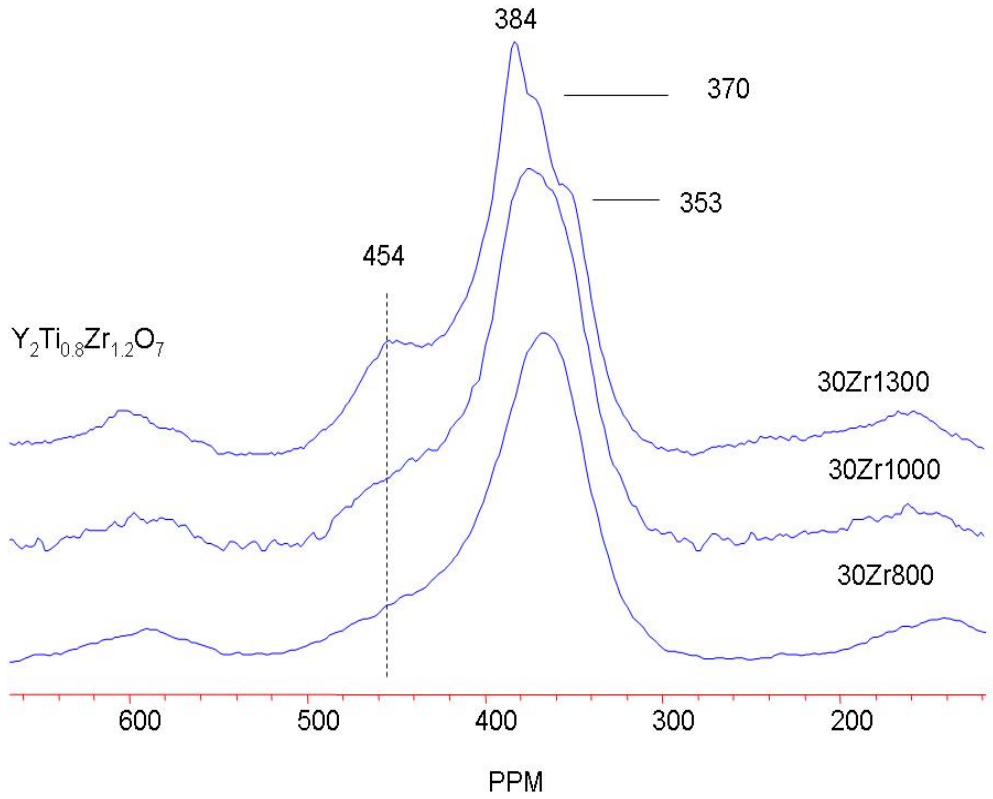

Figure 3. 16 ^{17}O MAS NMR of the compound 30Zr ($Y_2Ti_{0.8}Zr_{1.2}O_7$) heat treated at 800°C/1hr, 1000°/5hr and 1300°/5hr (bottom to top). As the temperature is increased, the transition from a fluorite structure to a disordered 'pyrochlore-like' structure is observed exemplifying both the subtlety of structural rearrangements of a metastable compound and the sensitivity of ^{17}O MAS NMR to structural rearrangements as noted in the profound differences in the three spectra presented in this figure.

When 30 mole % Zr is heat treated at 1000/5hrs (30Zr1000), the XRD reflections as seen in figure 3.5 decreases in breadth, yet, no superstructure reflections appear. The ^{17}O NMR spectrum of 30Zr1000 remains broad (figure 3.6) and featureless like that of 30Zr800, with the exception of another broad, weak resonance (~450 ppm) that emerges at the high frequency foot of the main resonance seen at 380 ppm. This perhaps indicates some local ordering.

The XRD of the $Y_2Ti_{0.8}Zr_{1.2}O_7$ compound (fig 3.5) heat treated at 1300/5hr (30Zr1300) is consistent with the diffraction pattern of a fluorite except for a very weak reflection at 38° reminiscent of the pyrochlore. Differences from the samples heated at 800 and 1000°C are seen in the widths of the reflections of the XRD only; no significant additional reflections appear suggesting that only the particle size has increased and/or the crystallinity has increased. The ^{17}O NMR of this sample (figure 3.6) exhibits separate resonances at 454, 384, 370,

and 353 ppm. A limited number of distinct oxygen environments must now be formed resulting in more resolved features in the spectrum.

3.4 Discussion

The diffraction of 10Zr800 in the work presented here clearly shows a broad superstructure reflection at 38° (fig 3.1). In the study by Schaedler *et al* [8], 10Zr800 is reported as a fluorite. This difference is accountable from slight differences in the heat treatment performed in our study compared to that described by Schaedler. In our study, amorphous samples were placed in a preheated furnace at specific temperatures for specific durations (see experimental section). In the study conducted by Schaedler *et al* [8], heat treatment was introduced in a stepwise manner. The furnace was preheated to 700°C, the sample was placed in the furnace for 1 hr, cooled in air, analyzed, reintroduced into the furnace at the next temperature (800°C) for 1hr, cooled in air, etc, through out the entire temperature range studied. Given the sensitivity of structural rearrangements that occur with heating in these systems, small variations inevitably will occur with small changes in heat treatment. Further, for the 20Zr1000 sample heated at 1000°C for 5 h in our study, the XRD in figure 3.3 shows the emergence of a broad and weak pyrochlore superstructure, whereas this same dopant level in [8] shows a fluorite. Again, the notable difference between the heating used in our study and that of Schaedler's is that our sample was heated for 5 h at 1000°C constantly where Schaedler heated the 20Zr sample for 3 separate 1 hr intervals, each at 100°C starting from 700°C. These differences are summarized in figure 9.9. It is interesting to note how the differences in structure reported by the two studies can serve as an example of structural dependence on heat treatment protocols.

From previous ^{17}O MAS NMR work on the fluorite to pyrochlore transition, it has been established that, of the two crystallographic oxygen sites in the pyrochlore structure, O1 coordinated by 2 Y and 2 Ti (denoted as $O1Y_2Ti_2$) resonates at ~455 ppm, whereas the O2 site is four coordinate with Y ($O2Y_4$) and resonates at 385 ppm [4]. For the stoichiometric pyrochlore, these two resonances are distinct, sharp lines because there is neither cation nor anion disorder (see figure 2a in [4]), and no significant contribution to line width due to distributions in chemical shift. Multiple oxygen environments are expected when there is cation substitution *and* disorder. The spectrum of 10Zr800 in figure 3.2 exemplifies this; two prominent features appear at 452 and 386 ppm. These are the two characteristic resonances of the $O1Y_2Ti_2$ and $O2Y_4$ oxygen environments found in the pyrochlore structure. However, they appear as features of a broader resonance that is indicative of distributions of bond lengths as well as other possible combinations of A and B cations coordinating to the same oxygen, for example where one of the Ti is substituted by Zr forming an OY_2TiZr environment.

The occupancy of the O3 site for the 10 mole % dopant level is 2-5% [6]. The detection of distinct O3 coordination is unlikely by ^{17}O NMR due to the low

concentration of these sites. The 10Zr1000 spectra in figure 3.2 reveals that, in addition to the main resonances of the pyrochlore structure found at 452 and 386 ppm, a small but distinct resonance lies to lower frequency just beyond the foot of the resonance at 386 ppm. This small feature appears at 343 ppm, which is in the expected range of a zirconium rich oxygen environment (table 2.1). Of the two Zr sites in the Baddeleyite structure, the tetrahedral OZr_4 site resonates at 324 ppm [2]. If we allow this resonance to increase in frequency per Y substitution for Zr in the tetrahedral OZr_4 site in Baddeleyite, a resonance at 343 ppm is observed which is assigned to the $O1Y_2Zr_2$ environment found in, for example, $Y_2Zr_2O_7$.

For the spectrum of 10Zr1300, the resonances found in the spectrum of 10Zr1000 are found here; a notable but subtle exception is the resonance at ~400 ppm. The resonance at 400 ppm is assigned to the oxygen environment of OY_2TiZr, containing only one Ti in the cation coordination shell as discussed in chapter 2. Substituting one Ti for one Zr in the first coordination sphere of oxygen would have the effect of shifting the resonance toward higher frequency, but not higher than an oxygen coordinated to 2 Ti and 2 Y.

Of the three compositions studied on the $Y_2Ti_2O_7$-$Y_2Zr_2O_7$ tie line in this study, perhaps the most dynamic as seen from the ^{17}O NMR spectra are the 20% mole substituted Zr (20Zr, fig 3.4) sample. The three separate heat treatments capture the metamorphosis from the fluorite structure to the disordered pyrochlore as seen from the NMR spectra. The ^{17}O NMR spectrum of 20Zr800 exhibits a single broad resonance that appears at about 380 ppm which is reminiscent of a fluorite. Complete cation disorder of the fluorite structure results in a broad line in the ^{17}O NMR spectrum, largely due to distributions in chemical shift resulting from the wide variety of local environments present in this material. The XRD of the 20Zr1000 sample overall suggests a fluorite structure. However, in the XRD at 38° a weak reflection appears of the pyrochlore structure just starting to form on the length scale probed by XRD (figure 3.3). The ^{17}O NMR spectrum however, exhibits discernable resonances that suggest local pyrochlore-like environments reminiscent of other ^{17}O NMR studies of pyrochlore structures, where the pyrochlore resonances appear at 446 and 385 ppm (fig 3.4). This suggests cation ordering that is intermediate between that found in the pyrochlore and fluorite structures. Arrangements that are neither pyrochlore nor fluorite must maintain a certain amount of disorder for they are not purely ordered pyrochlores. These local environments of disorder are most likely responsible for anionic conduction observed in these materials, for one requirement of anionic conduction in crystalline materials is that oxygen sublattice remains disordered. When the anion sublattice is highly ordered, such as that found in the pyrochlore, conductivity is noticeably lower [11]. An intermediate arrangement of $O1A_2BB'$ coordination about oxygen would be in concert with this degree of disorder and is more likely found in the fluorite structure. In the deconvolution of this spectrum (20Zr1000), a resonance at 405 ppm suggests (figure 3.7) $O1A_2BB'$ coordination due to the chemical shift range of this environment. It is assigned to an O environment of $O1Y_2TiZr$ on this basis. In the 20Zr compounds, O3 occupancy approaches 20%. The O3 site has $O3B_4$ coordination so it is likely that the

resonance at 429 ppm has oxygen coordinated to both Zr and Ti, forming an $O3Ti_2Zr_2$ environment which would be expected to resonate in this range. However, the resonance at 347 ppm in figure 3.7 may have contributions from O1 and O3 resonances. O1 coordinated to 2Y and 2Zr is expected to resonate here. However, the increased occupancy of the O3 site will contribute to intensity in this frequency range due to O3 being coordinated to 4 B site cations. This region likely contains $O1Y_2Zr_2$ resonances. $O1Y_2Zr_2$ coordination arises from the pyrochlore-like environment (distinct cation coordination to O1) and $O3Zr_4$ arising from the disordered array of anions where O3 occupancy occurs. Following the same trend of O3 occupancy, the feature at 364 ppm in figure 3.8 is therefore assigned to oxygen coordinated to both Zr and Ti, rich in Zr coordination and is assigned to $O3Zr_3Ti$. The areas under the curve, as shown in the table of figure 3.8, approximate the 20% O3 occupancy of this compound. Again, the breadth of these peaks, suggests distributions in chemical shift. An $O3Ti_4$ environment was not observed which is perhaps due to the instability of a Ti atom coordinated to more than 6 O atoms. However, this arrangement is likely to occur as the O3 site is occupied. The instability of the OTi_4 site may help account for the dramatic increase in conductivity of this compound as reported in [6].

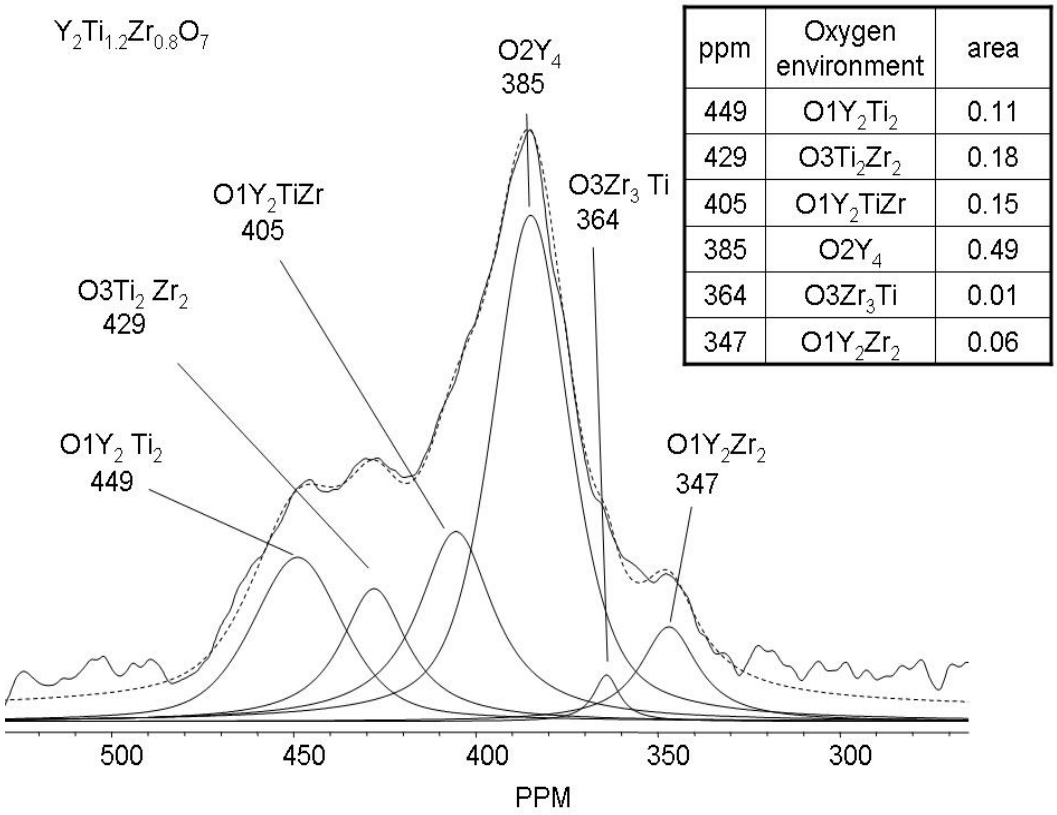

ppm	Oxygen environment	area
449	$O1Y_2Ti_2$	0.11
429	$O3Ti_2Zr_2$	0.18
405	$O1Y_2TiZr$	0.15
385	$O2Y_4$	0.49
364	$O3Zr_3Ti$	0.01
347	$O1Y_2Zr_2$	0.06

Figure 3. 17 Deconvolution of the sample $Y_2Ti_{1.2}Zr_{0.8}O_7$ (20Zr1000) heat treated at 1000°C for 5 hrs. Distinct oxygen environments can be seen based on the

deconvolution using NUTS software. Ppm assignments in figure are those of the deconvoluted peaks along with their assignments to possible oxygen environments in the structure. Dashed line is the simulated spectrum.

The XRD sample 20Zr1300 reveals the emergence of a very weak pyrochlore reflection at about 38° (figure 3.3) suggesting pyrochlore-like domains. The ^{17}O NMR spectrum in figure 3.4 is consistent with the XRD in that pyrochlore resonances dominate at 446 and 385 ppm. These are assigned to the oxygen environments of the pyrochlore structure $O1Y_2Ti_2$ and $O2Y_4$, respectively. However, a smaller but significant resonance is seen at a lower frequency resonating at 343 ppm. Based on the argument of Y and Zr decreasing the resonance frequency of oxygen and the possibility of the O1 site being coordinated to two yttrium atoms and two zirconium atoms, this resonance is assigned to the $O1Y_2Zr_2$ oxygen environment in the pyrochlore structure. In addition, $O3B_4$ environments are expected as the O3 occupancy is 20% for this compound [6] which would result in an $O3Zr_4$ environment. Still, the breadth of the lines suggests distribution in chemical shift for the overall shape is not completely synonymous with other pyrochlore structures studied previously. Hidden between the two dominant resonances seen at 446 and 385 ppm in this spectrum, a submerged resonance gives rise to the slight feature at ~400 ppm, of an $O1Y_2TiZr$ environment. The deconvoluted peak at 425 ppm is likely to be an $O3Ti_2Zr_2$ environment. Comparing the ^{17}O NMR spectra of $Y_2Ti_2O_7$ and $Y_2(Zr_{0.3}Ti_{0.7})_2O_7$ from N. Kim *et al* [4] to the work presented here, it is noted that the spectrum of the 20Zr1300 best resembles that of the disordered pyrochlore of $Y_2(Zr_{0.3}Ti_{0.7})_2O_7$. The two spectra (20Zr1300 and $Y_2(Zr_{0.3}Ti_{0.7})_2O_7$) differ most notably in the low frequency foot at approximately 343 ppm as well as the broad feature in between the to main pyrochlore resonances in this work, not seen in the spectrum of *Kim et al*. In this current work, the resonance at 343 is more defined, separated from the dominant resonance of the $O2Y_4$ site at 385 ppm. This separation is possibly due less broadening of both resonances at 385 and 344 ppm, respectively. The peak at 344 ppm does not resonate at a high enough frequency to account for any Ti atom in the first coordination sphere of the O while simultaneously not resonating at a low enough frequency to contain all Zr atoms in the first coordination shell. However, in the spectrum of $Y_2(Zr_{0.3}Ti_{0.7})_2O_7$ ([4]), the two resonances at 463 and 385 do not have the broad component between them as is evident in the spectrum in this study (fig 3.4, 20Zr1300). An additional resonance seen in the deconvolution of figure 3.8 reveals two small resonances at low frequency. This resonance at 344 is assigned to $O1Y_2Zr_2$ and the resonance at 329 ppm is assigned to $O3Zr_4$. The OZr_4 environment found in Baddeleyite [2], which has a resonance of 324 ppm, is very close to our deconvoluted peak at 329 ppm.

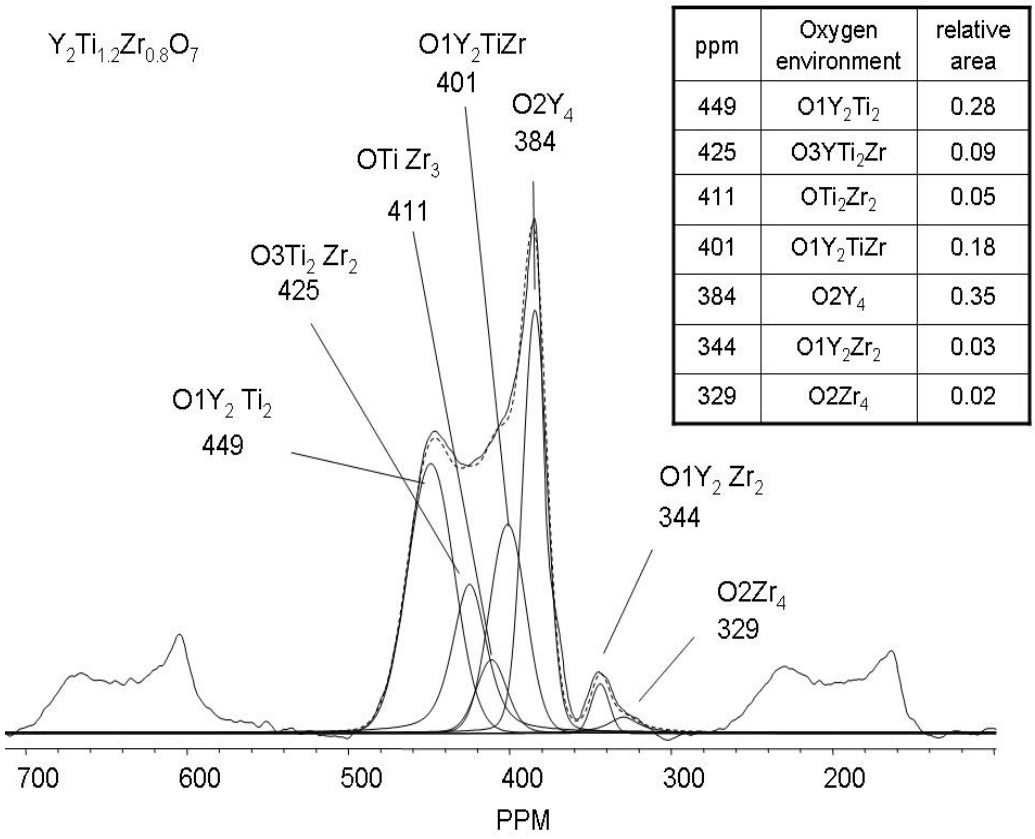

ppm	Oxygen environment	relative area
449	$O1Y_2Ti_2$	0.28
425	$O3YTi_2Zr$	0.09
411	OTi_2Zr_2	0.05
401	$O1Y_2TiZr$	0.18
384	$O2Y_4$	0.35
344	$O1Y_2Zr_2$	0.03
329	$O2Zr_4$	0.02

Figure 3. 18 Deconvolution of ^{17}O NMR spectrum of $Y_2Ti_{1.2}Zr_{0.8}O_7$ (20Zr1300) after heat treatment of 1300°C for 5 hrs. Pyrochlore resonances intensify revealing a disordered pyrochlore where there is further ordering of the O1 and O2 sites.

As Zr is increasingly substituted for Ti along the tie-line, the system tends to stay in a disordered state on heating. For the 30% mole substituted compounds (30Zr), excessive heat treatment (3+days) at elevated temperatures (>1300°C) phase separation between the fluorite and pyrochlore structures has been documented [6-8]. At this dopant level, the O3 site approaches 50% occupancy. An O3 occupancy of 50% further alters the O1 position by displacing it from its ideal position found in the stoichiometric pyrochlore, causing it to relax toward the O3 site. This will affect the M-O bond lengths [6] and further induce repulsive effects between the O1 and O3 sites. In addition, the thermal anisotropy for the O1 site at this dopant level is significant [6]. All of these factors contribute to the broadening of the ^{17}O NMR spectra. In addition, at this level of Zr substitution for Ti, a small degree of A and B site cation exchange takes place as seen from the reduced neutron scattering of Y located in the A site [6]. Yttrium has the strongest neutron scattering power of the cations in the sample, and, decreasing scattering intensity from the A site at this dopant level is

attributable to a decrease in yttrium concentration on the A site. Combining these factors with the metastable nature of the samples reported on in this study, 'intermediate' states of order between the fluorite and the pyrochlore are observed in the weak pyrochlore-like reflection in the XRD of 30Zr1300 (fig 3.5). This may be further explained by comparison of the ^{17}O NMR spectra of the 30Zr series (fig 3.6) to the XRD of the same series (fig3.5). The XRD shows the fluorite sublattice only for samples heated at 800 and 1000°C (fig 3.5) where the ^{17}O NMR spectrum of 30Zr800 is in agreement with this. However, the ^{17}O NMR spectrum of 30Zr1000 shows development in the 454 ppm region suggesting formation of local ordering but further interpretation is limited due to the low intensity and significant breath. However, this difference in the resonance at 454 ppm between 30Zr800 and 30Zr1000 at ~454 ppm suggests a certain increase in cation ordering. This region of the spectrum is where oxygen coordinated to 2Y and 2Ti occurs in the stoichiometric pyrochlore. The ^{17}O NMR of the 30Zr1300 further exhibits the beginnings of cation ordering for distinct oxygen environments emerge. The XRD in figure 3.5 of 30Zr1300 shows a slight indication of pyrochlore superstructures, consistent with the suggestion of pyrochlore ordering seen in the ^{17}O NMR spectrum. Taking into account the 50% occupancy of the O3 site, the thermal anisotropy of the O1 site and the onset of A and B mixing [6], distinction of the O1, O2 and O3 sites becomes difficult when assigning these resonances to this spectrum of 30Zr1300 (fig 3.6) Yet, the two resonances at 454 and 384 ppm are reminiscent of the pyrochlore as previously discussed suggesting OY_2Ti_2 and OY_4 like environments. Other discernable resonances emerge at 370, 353 ppm, which can only be due to substitution of Ti for Zr, and a smaller amount Zr substituting for Y. The resonance at 370 ppm is assigned to an environment of OZr_3Ti and the resonance at 353 ppm to OZr_4. In comparing the assignments of these environments to that of figure 3.7, a shift to higher frequency for the same oxygen environments are found in figure 3.6 (30Zr1300). This may be accounted for by the increased repulsion induced by the closer proximity of the O1 and O3 sites in the higher doped compound. Inevitably, as the O1 site relaxes toward the O3 site, distortion in the oxygen valence due to repulsion of the two sites will occur and this can change the resonance of the chemical shift of these oxygen environments.

The difference in ordering of cations between the 10Zr series and the 20Zr series serves as a measure of the ordering of the anion sublattice as shown from the ^{17}O NMR spectra. As disorder increases, conductivity increases, most notably between 10 Zr and 20Zr [11]. The ^{17}O NMR spectra illustrate that one of the primary differences between the oxygen environments in these two series (10 and 20Zr) is that intermediate cation ordering is observed that is neither pure fluorite (where there is no distinction between cation sites) nor pure pyrochlore (where there is no mixing between A and B sites, and oxygen vacancies are strictly on the O3 site) for 20Zr. For this intermediate arrangement to exist, a certain amount of anionic disorder must be present. It is therefore these local domains of disorder, with distinct cation arrangements, that are partially responsible for the

conductivity of the samples (≥ 20 mole % Zr). The local disorder is maintained, while the longer range order as seen by XRD remains pyrochlore.

3.5 Conclusions

^{17} O NMR and XRD have been used to study the crystallization at both the local and long – range orders of the fluorite and pyrochlore structures. Compounds were synthesized using liquid precursors, facilitating homogeneous atomic level mixing. Mild heat treatments allowed the observation of metastable forms of the compounds, 10Zr ($Y_2Ti_{1.2}Zr_{0.4}O_7$), 20Zr ($Y_2Ti_{1.2}Zr_{0.8}O_7$), and 30Zr ($Y_2Ti_{0.8}Zr_{1.2}O_7$) which lies along the tie-line of $Y_2Ti_2O_7$ –$Y_2Zr_2O_7$. As crystallization occurs, the fluorite to disordered pyrochlore transition has been observed as cation ordering results. Increased heat treatments greatly affect the structure of the compound, resulting in differences in the first coordination sphere of oxygen. Doping Zr for Ti has the effect to disorder the cation and anion array; as more Zr is added, the normally vacant O3 site becomes increasingly occupied with distinct resonances seen in the ^{17}O NMR spectra of these compounds. Occupancy of the O1 and O3 sites becomes ~50% at 30 mole % Zr substitution for Ti. This broadens the ^{17}O NMR spectra, however, distinct oxygen coordination is observed in 30Zr series, suggesting local level order of distinct cation combinations coordinated to oxygen.

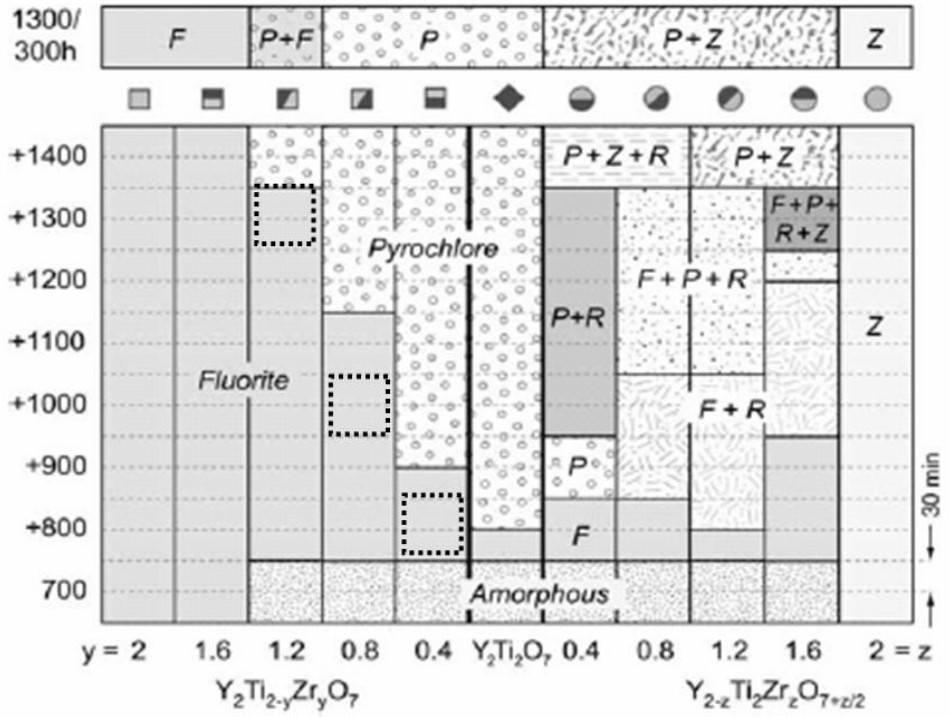

Figure 3. 19 Phase evolution map adapted from Schaedler *et al* (Reference 8). Dashed boxes indicate where the pyrochlore superstructure reflection begins to occur in our work.

3.6 References

[1]. J. L. Palumbo; T. A. Schaedler; L. Peng; C. G. Levi; C. P. Grey, *J. Solid State Chem.* **2007,** 180, (7), 2175 2185.

[2]. T.J. Bastow; S.N. Stuart, *Chem. Phys.* **1990,** 143, 459-467.

[3]. T. J. Bastow; P. J. Dirken; M. E. Smith; H. J. Whitfield, *J. Phys. Chem.* **1996,** 100, 18539-18545.

[4]. N. Kim; C. P. Grey, *J. Solid State Chem.* **2003,** 175, 110 - 115.

[5]. B. J. Wuensch; K. W. Eberman; C. Heremans; E. M. Ku; P. Onnerud; E. M.E. Yeo; S.M. Haile; J. K. Stalick; J. D. Jorgensen, *Solid State Ionics* **2000,** 129, 111-133.

[6]. C. Heremans; B.J. Wuensch, *J. Solid State Chem.* **1995,** 117, 108-121.

[7]. Y. Liu; R. L. Withers; L. Noren, *J. Solid State Chem.* **2004,** 177, 4404.

[8]. T. A. Schaedler; W. Francillon; A. S. Gandhi; C. P. Grey; S. Sampath; C. G. Levi, *Acta Materialia* **2005,** 53, 2957-2968.

[9]. C. G. Levi, *Acta Materialia* **1998,** 46, (3), 787.

[10]. C. Suryanarayana, *Prog. Mat. Sci.* **2001,** 46, 1-184.

[11]. C. Heremans; B.J. Wuensch, *J. Solid State Chem.* **1995,** 117, 108-121.

Chapter 4:

Studies of Structure and Dynamics of $La_{1-x}Sr_xGa_{1-y}Mg_yO_{3-(x+y)/2}$ (LSGM) through the use of Variable Temperature ^{17}O and ^{71}Ga MAS NMR Spectroscopy and X-Ray Diffraction

Abstract:

^{17}O and ^{71}Ga variable temperature (VT) MAS NMR and VT XRD have been used to characterize a series of singly and doubly doped varieties of $LaGaO_3$. When La is substituted for Sr and Mg for Ga, all structures have either a distorted or cubic perovskite structure. Variable temperature XRD data reveal that, depending on the dopant and the dopant level, the structures have either rhombohedral or cubic symmetry. ^{17}O MAS NMR collected at room temperature and 240°C reveal that upon mild heating, oxygen motion is present as observed by a loss of spinning sidebands present in the room temperature spectra. ^{71}Ga MAS NMR in the same temperature range show that Ga environments of 6 and lower exist in both the singly and doubly doped compounds and that the coordination possibly changes with heat treatment.

4.1 Introduction

$LaGaO_3$ belongs to the ABO_3 perovskite family. $LaGaO_3$ adopts a distorted perovskite structure with orthorhombic symmetry in space group Pbnm, where the distortions are due to the GaO_6 octahedral tilting (figure 1). The Glazier notation (see below) [1] of the tilt scheme in room temperature $LaGaO_3$ is described as $a^-b^-c^+$. At 145°C $LaGaO_3$ exhibits a phase change going to the rhombohedral space group R-3c with a tilt scheme of $a^-a^-a^-$ [2]. Doping $LaGaO_3$ with Sr on the A site and Mg on the B site, introduces oxygen vacancies into the lattice resulting in sufficiently high ionic conductivity so that it can be used as an electrolyte in a SOFC operated at 850°C [3, 4]. In addition, it is stable in reducing atmospheres and ranges of oxygen partial pressures where other solid oxide electrolytes are not [5]. Also, cathode and anode materials made of perovskites can be used with the LSGM electrolyte, allowing for similar thermal expansion behaviors amongst components, increasing the life time of an SOFC.

The over all structure of LSGM is the subject of dispute in the literature. The material has at least one phase change between 300 – 500°C [4, 6, 7], yet results from different groups for the room temperature structure and the high temperature structural results do not agree. For example, in 1998 *Slater et al* [4] reported that $LaGaO_3$ with 10%Sr on the A site and 20% Mg on the B site (LSGM1020) adopts the space group I2/a, whereas in 2001, *Lerch et al* [6], report that the space group for the room temperature structure of the same compound to be Imma. Further, in the study performed in 1998, the high temperature phase is indexed in space group R-3c, whereas in the study of 2001, the high temperature phase is indexed to Pm3m. Other variations exist, which are summarized in Table 4.1.

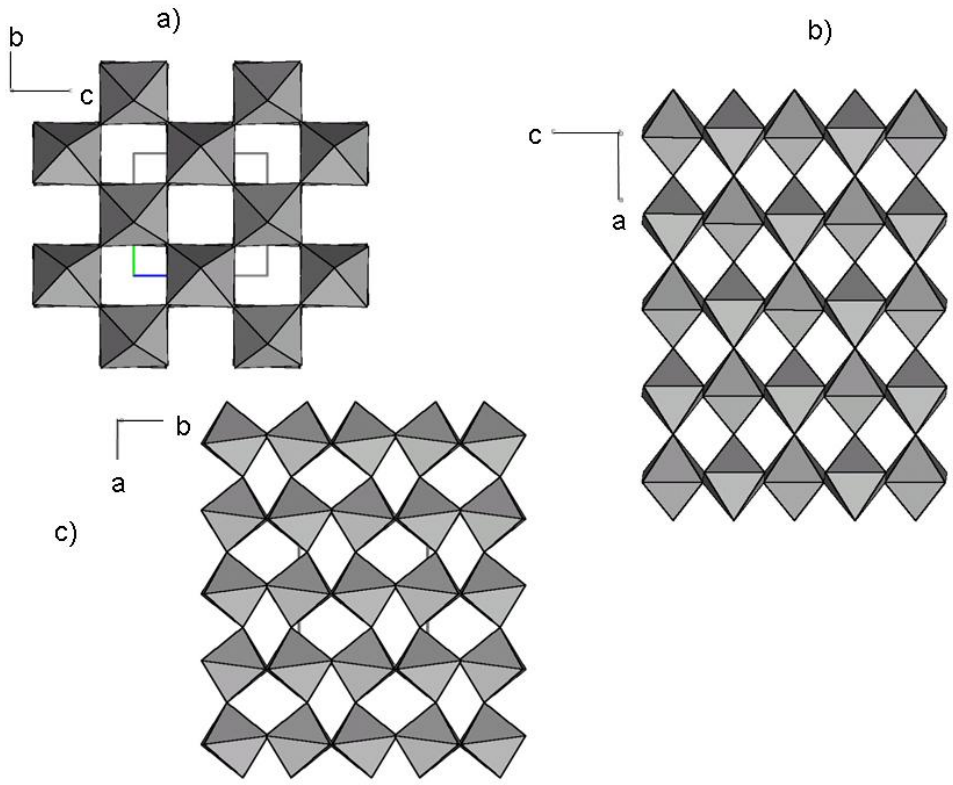

Figure 4. 38 Room temperature LSGM1020 structure showing octahedral tilts of the I2/a phase (adapted from P. R. Slater *et al. Solid State Ionics).* In all three views the GaO_6 octahedra are out of phase. The angle of the tilts about the a and b axis are the same.

Despite the discrepancies in the details of the symmetry of these materials as noted above, all structures have in common tilting of the GaO_6 octahedra at room temperature. In short, adapting the Glazier notation [1], *Slater et al* describes the monoclinic structure, I2/a as having $a^- a^- c^-$ tilt scheme (synonymous tilting is found in the rhombohedral structure, $R\bar{3}c$) where the phases of tilt are opposite with respect to the [100] direction vs. a tilt scheme in the orthorhombic structure Pnma where phases are the same along the [100] direction, notated as $a^+ b^- b^-$. The degree of octahedral tilting is the maximum in the pure compound at room temperature, at 11° (figure 4.1) [8] .

Doping the lanthanum gallate structure seems to minimize the octahedral tilt angles as reported by [9], allowing for enhanced ionic conduction due to an increased aperture for the oxygen ion to travel through [4]. The oxygen sites were refined and it was found that at lower temperatures (<500°C) the vacancies order, preferably on the apical O2 site. In a combined neutron and electron diffraction study by *Skowron et al.* [10] ordering of oxygen vacancies at lower temperature in LSGM2015 was also found. Further, it was postulated that, as a result of high resolution transmission electron microscopy (HRTEM), local structures with symmetry lower than cubic were found [14]. In [14], the average structure of LSGM2015 was cubic

yet regions on the order of 20 – 40 Å were detected, consisting of domains of lower symmetry. Upon heating to 600°C, these regions disappear, consistent with the onset of ionic conductivity. These domains which then reappear upon cooling. It is believed that the regions with random domain orientations are those where oxygen vacancies are ordered. The resultant sub-domains impose a super structure on the system in which the oxygen vacancies order into planes. These sub-domains were compared to the tetrahedral BO_4 layers found in the browmillerite structure [11].

The room temperature structures of the doped compounds vary with dopant (either just Mg or Sr or both, and the amount of the single dopants or both) as summarized in table 1. At above 500°C, the structure changes dependent on the amount of dopants [10]. The doubly doped compound at high temperature exhibits cubic symmetry.

The limit of solid solution of the singly doped species varies. It has been found that limit of singly doped species is 10% and 20% for Sr and Mg respectively [12]. However, it has been shown that the simultaneous addition of Mg and Sr extends the solid solution range of Sr to 20%. Our studies concur with these findings.

Singly doped species exhibit different conductivity from each other and from the doubly doped compounds [12]. When $LaGaO_3$ is doped only with 10% Sr [12], it is found that the conductivity at a given temperature is higher than when doped with the same amount of Mg [13, 14]. This is attributable to the difference in activation energy associated with oxygen vacancy ordering and motion as a result of Sr vs. Mg doping based on computer simulations [13]. Activation energy associated with Mg doping is sufficiently high to act as a 'trap' of oxygen-vacancy clusters, prohibiting appreciable anionic mobility. Sr doping has the opposite effect [15], lowering the activation energy of the vacancy hopping. However, when doped with both Sr and Mg, the experimentally determined conductivity is appreciably higher [12].

Sample	25°C	Above 500°C	Reference
LSGM2020	$Pm\bar{3}m$	no data	[16]
LGM20	Pbnm	no data	Ibid
LSGM1010	I2/a	$R\bar{3}c$	[8]
LGM10	Ibmm	$R\bar{3}c$	Ibid
LSGM1020	Imma	Pm3m	[9]
LSGM1020	I2/a	R3c	[6, 9]
LSGM2015	$Pm\bar{3}m$	no data	[10]

Table 4. 2 Different phases of singly and doubly doped $LaGaO_3$ as reported from the results of neutron scattering experiments.

Characterising the local structure of a dynamic material in is a challenge, for often the local level ordering of a material differs significantly from the average structure detected across the sample. NMR has been shown to be an affective tool for monitoring local structures as they deviate from the macro level ordering. NMR has also been successfully used to help characterize dynamic systems where there is molecular motion [17, 18]. 71Ga NMR is a particularly good tool for determining local geometry as different Ga coordination environments resonate in frequency ranges which have been previously characterized and are most often resolvable from one another as shown in [19].. In the spinel $MgGa_2O_4$, Ga exists as 4 coordinate and six coordinate environments, which resonate at 171 and 74 ppm, respectively. In the same study, Ga in the cristobalite polymorph of $GaPO_4$ was reported to resonate at 118 ppm with Ga inhabiting a 4 coordinate environment. The 4 coordinate environment of the quartz polymorph of $GaPO_4$ resonates at a similar frequency (111 ppm). Also in the same study, Ga in a 6 coordinate environment of a layered gallium hydroxyphosponate is reported to resonate at 48 ppm. In addition to the chemical shift information, the lineshape can also be very sensitive to the local symmetry of the coordination environment. A characteristic lineshape, due to the second order quadrupolar interaction, may be observed, and can be used to determine whether the atom is in an axial or lower symmetry environment. In another NMR study of $^{69, 71}Ga$, ^{139}La, in $LaGaO_3$ and LSGM1010 [19], it was found that lines shapes of the spectra (both $^{69,71}Ga$ and ^{139}La NMR) of the pure and doped compounds reflect structural disorder when going from the pure compound to the doubly doped compound. η values for pure $LaGaO_3$ of ^{139}La and ^{69}Ga as reported in [19] are 0.3 (±0.03) and 0.05(±0.015), respectively, while QCC values reported are 2.10(±0.03) MHz and 49.0 (±0.2) MHz for ^{69}Ga and ^{139}La, respectively. The ^{71}Ga NMR spectrum of the pure compound has a well resolved lineshape that can be simulated to extract the asymmetry parameter η and the QCC (QCC = e^2Q/h), which is a product of the nuclear quadrupole moment and the surrounding electric field gradient consistent with those found in [20]. The ^{71}Ga NMR spectra of the doped compound are convoluted and cannot be readily simulated to extract these parameters. ^{17}O NMR has the same ability to determine local coordination as well as the kind of geometry. In other ^{17}O NMR studies, [11, 17, 18, 21, 22] oxygen was shown to resonate at different frequencies with varying line widths depending on the cation present in the first coordination shell as well as the coordination number. In this study, we investigate the effect of doping Mg and Sr, in both singly and doubly doped $LaGaO_3$ through the use of ^{17}O and ^{71}Ga NMR spectroscopy, to monitor changes in the local coordination of O and Ga and relate this to changes in structure in an attempt to help describe the mechanism of ionic conduction in these materials.

4.2 Experimental

Synthesis of the pure, singly and doubly doped samples began with stoichiometric amounts of Ga_2O_3, $SrCO_3$, MgO, and La_2O_3, where the La_2O_3

was heated in an open muffle furnace to 1000°C for 2 hrs prior to weighing to drive off sorbed CO_2 and H_2O. Weighed powders, such that the ratio of masses of the milling media to reactant masses were 3:1, were placed in a 50 mL stainless steel vessel with 3, 10 mm diameter stainless steel milling media spheres and milled in a high energy planetary ball mill at 600 rpm for 4 hrs. The resultant mixtures were examined using a Rigaku X-ray diffractometer directly after ball milling, and found to have an amorphous component at low 2θ as well as the strong reflections of the perovskite structure often evident in the diffraction pattern. Powders were then pressed into pellets and sintered in a muffle furnace at 1450°C for 4 – 6 hours, then reexamined by XRD to determine sample purity. High resolution XRD spectra were obtained for the same set of samples as a function of temperature, from room temperature to 900°C, at Brookhaven National Laboratory's (BNL) Nation Synchrotron Light Source (NSLS) X-7B with a wavelength of 0.92111 (5) Å

Variable temperature (VT) ^{17}O MAS NMR experiments were performed with a double or triple resonance 4mm MAS Chemagnetics probe on a 500 MHz spectrometer operating at 67.7 MHz or on a 360 MHz spectrometer operating at 48.8 MHz, with a rotor spinning speed of 15 kHz. One pulse and Hahn echo ($\pi/2 - \tau - \pi - \tau$) pulse sequences were used with solid $\pi/2$ pulses of 2.2 μs with pulse delays of 1s. Shifts were referenced to $H_2{}^{17}O$ (10% ^{17}O, Isotec.) at 0 ppm**.** ^{71}Ga NMR VT data were collected at Larmor frequencies on the same spectrometers operating at 152.4 MHz or 109.797 MHz, respectively, and at a spin rate typically of ~15 kHz. In addition a Chemagnetics 3.2mm probe was used, with rotor spinning of 20 kHz. One Pulse or Hahn echo pulse sequences were deployed which utilized a ($\pi/2 - \tau - \pi - \tau$) pulse sequence where $\pi/2 = 2.3\mu s$. The gallium reference used was a 1M $Ga(NO_3)_3$ solution and the subsequent chemical shift of the sample was set to 0.0 ppm. VT experiments were realized by using a Chemagnetics variable temperature stack. The temperature range employed was from room temperature to 250°C.

^{17}O enrichment was conducted by placing powdered samples in vacuum tubes and ^{17}O gas (40-60% purity, Isotec) was added and sealed with a stop cock. The sealed tubes were then heated to 600°C in a tube furnace for 24 hours to allow the ^{17}O exchange to occur. The enriched compounds were characterized by XRD to ensure sample purity.

Some of the samples were run on both an 8.45 and 11.7 T magnets. Line narrowing was observed as a function of magnetic field strength for spectra of both nuclei which suggests that 2nd order quadrupolar interaction is present which broadens the lines of the spectra. Based on the shapes of the lines for the ^{71}Ga spectra, distributions in second-order quadrupolar interactions are also present, which further lend difficulty in interpretation of structural information. In some of the spectra, chemical shift distributions are a likely contribution to the line broadening also.

4.3 Results

4.3.1 XRD results

XRD data of $LaGaO_3$ display no impurities and the diffraction is consistent with JCPDS card 24-1102 of $LaGaO_3$ (figure 4.2).

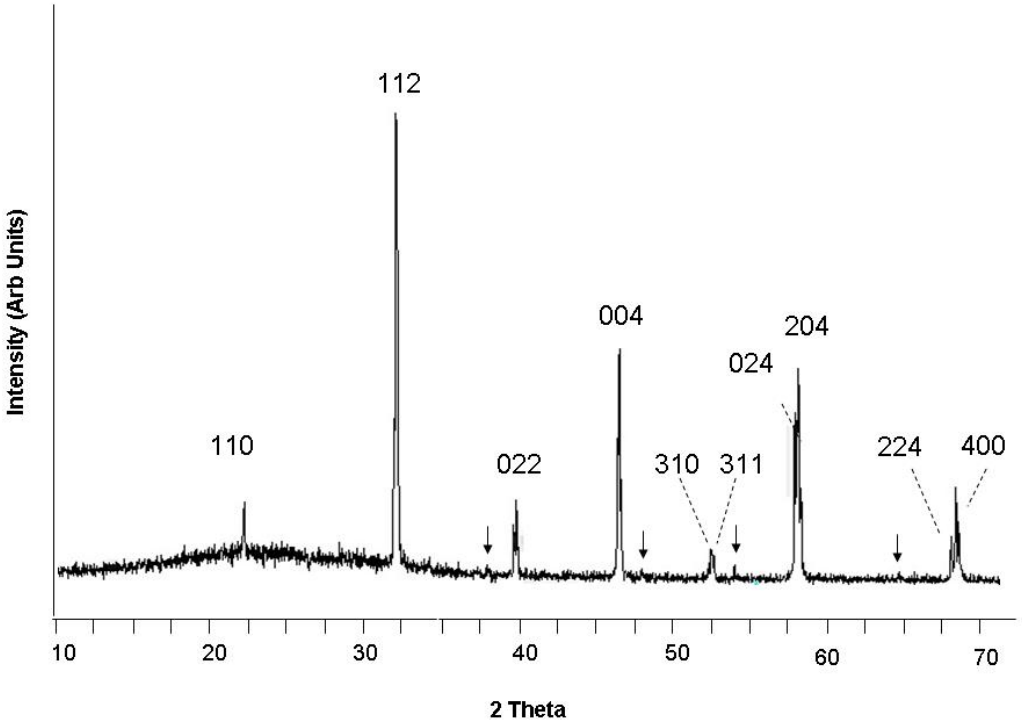

Figure 4. 39 XRD of $LaGaO_3$ collected on a Rigaku bench top diffractometer using Cu Kα. The diffraction pattern is consistent with literature reports and can be indexed with the space group Pbnm. Arrows indicated residual β-Ga_2O_3.

The XRD pattern of LSG10 shows an impurity of $SrLaGa_3O_7$, $P42_1m$ [23] (JCPDS card 45-0637). Neglecting reflections of the impurity, the high resolution diffraction spectrum of LSG10 was indexed to space group R-3c (figure 3) from room temperature to 900°C. The lattice parameters (summarized in table 2) show an increase in both a and c as temperature is increased.

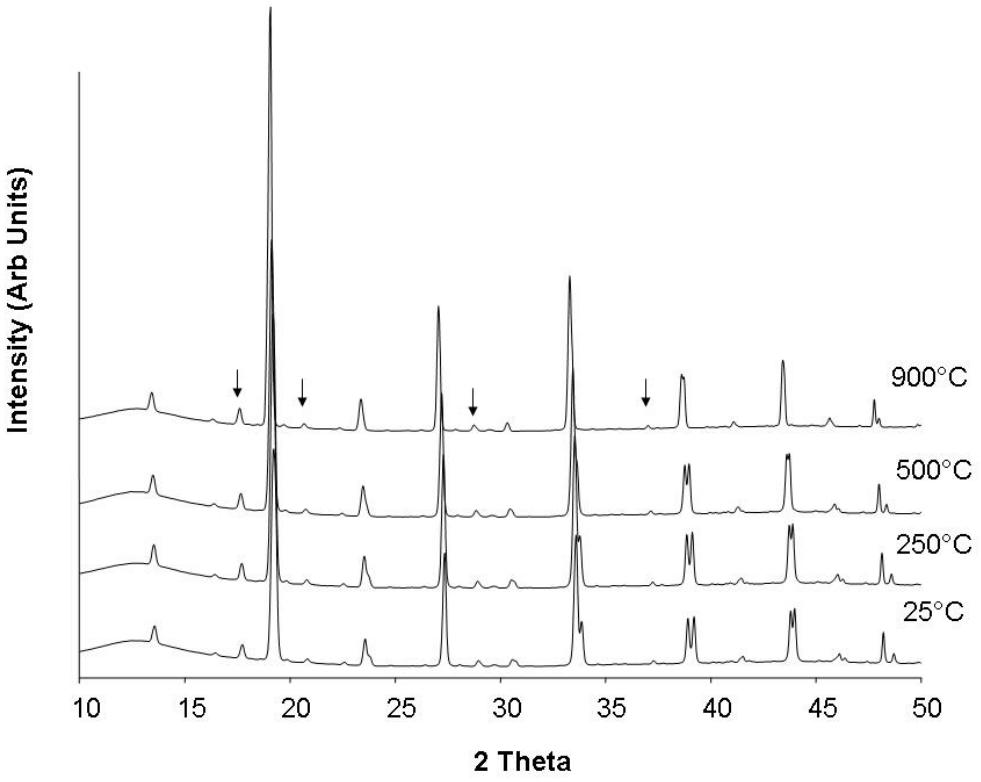

Figure 4. 40 LSG10 variable temperature XRD data collected at Brookhaven National Laboratory's National Synchrotron Light Source (BNL's NSLS). Low concentrations of the impurity $SrLaGa_3O_7$ are indicated with arrows.

sample	LSGM4,4	LSGM1010	LSGM1717	LSGM2020	LSG10	LGM20
space group	Pbnm	R-3c (a, c)	Pm3m	Pm3m	R-3c (a, c)	Pbnm
25°C	5.50 (1) (a) (Å) 5.54 (1) (b) 7.78 (1) (c)	5.52 (1) (Å) 13.39 (2) 2.43 (c/a)	3.92 (1) (Å)	3.92 (1) (Å)	5.52 (2) (Å) 13.40 (2) 2.42 (c/a)	5.56 (2) (a) (Å) 5.59 (2) (b) 7.87 (2) (c)
250°C	R-3c (a, c) 5.55 (1) (Å) 13.44 (1) 2.42 (c/a)	5.54 (1) (Å) 13.55 (2) 2.45 (c/a)	3.92 (1) (Å)	3.93 (1) (Å)	5.52 (1) (Å) 13.42 (2) 2.43 (c/a)	5.66 (1) (a) (Å) 5.68 (1) (b) 7.99 (2) (c)
500°C	5.55 (1) (Å) 13.50 (1) 2.43 (c/a)	5.56 (1) (Å) 13.64 (3) 2.45 (c/a)	3.94 (1) (Å)	3.94 (1) (Å)	5.55 (1) (Å) 13.48 (1) 2.43 (c/a)	R-3c (a, c) 5.51 (2) (Å) 13.46 (6) 2.44 (c/a)
900°C	5.55 (2) (Å) 13.51 (2) 2.43 (c/a)	cubic 3.95 (1) (Å)	3.96 (1) (Å)	3.96 (1) (Å)	5.57 (1) (Å) 13.60 (3) 2.44 (c/a)	5.55 (4) (Å) 13.56 (1) 2.44 (c/a)

Table 4.2 Cell indexing of XRD data of the LSGM series collected at the NSLS. Cell indexing done with Jade software.

The XRD pattern of LGM10 in figure 4 (Rigaku) reveals no detectable impurity; the peak splitting observed is consistent with that of the JCPDS diffraction (24-1102) of $LaGaO_3$ and the orthorhombic space group Pbnm.

Variable temperature XRD data of LGM20 data show no detectable impurities and the diffractogram profile indicates R-3c structure at all temperatures investigated (figure 4.5). The variable temperature X-ray diffractogram of LSGM4,4 collected shows minor impurities of $La_4Ga_2O_9$ (JCDPS card 37-1433) and $SrLaGa_3O_7$ (JCPDS card 45-0637), otherwise, fits the profile of R-3c throughout the temperatures explored (figure 6). The VT XRD OF LSGM1010 (figure 7) reveals the structure remains rhombohedral though 500°C. Above 500°C it is best fit to a cubic pattern. The XRD pattern of 1717 and 2020 (figures 8 and 9) are consistently cubic with increasing lattice parameter through to 900°C.

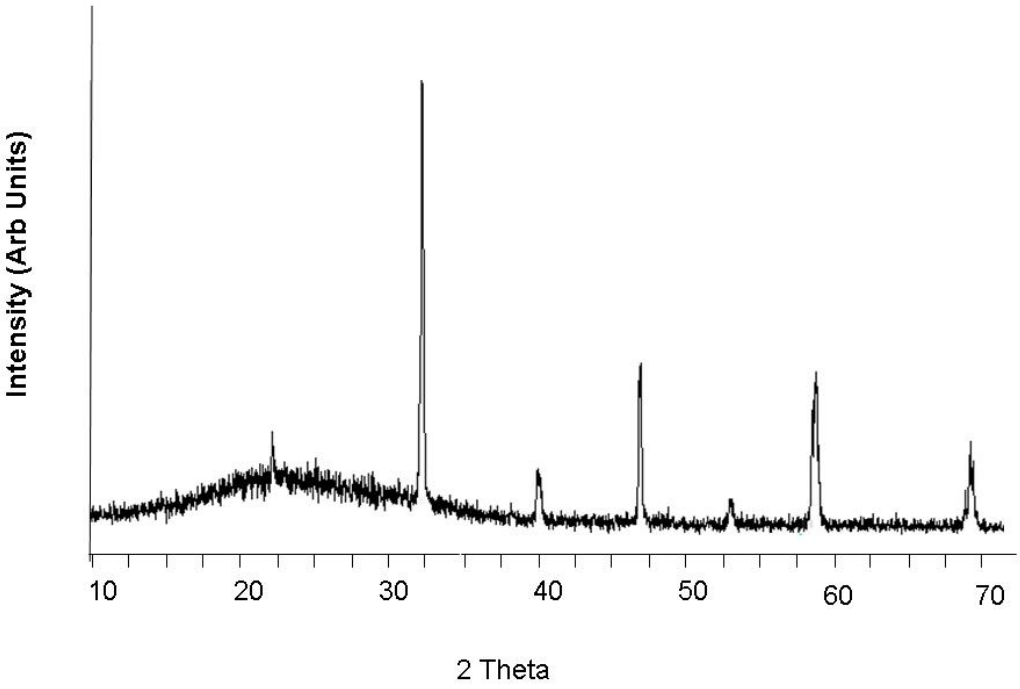

Figure 4. 41 XRD of LGM10 collected on the Rigaku bench top diffractometer using Cu Kα. The diffraction pattern is consistent with the Pbnm space group adapted by $LaGaO_3$ (JCPDS 24-1102).

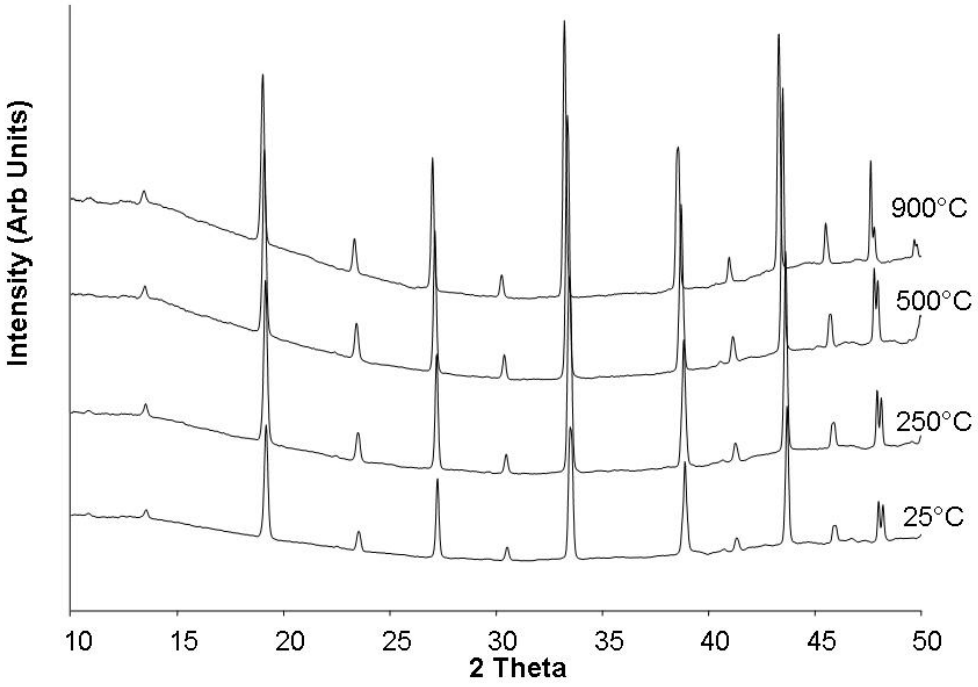

Figure 4. 42 LGM20 variable temperature XRD data collected at BNL's NSLS.

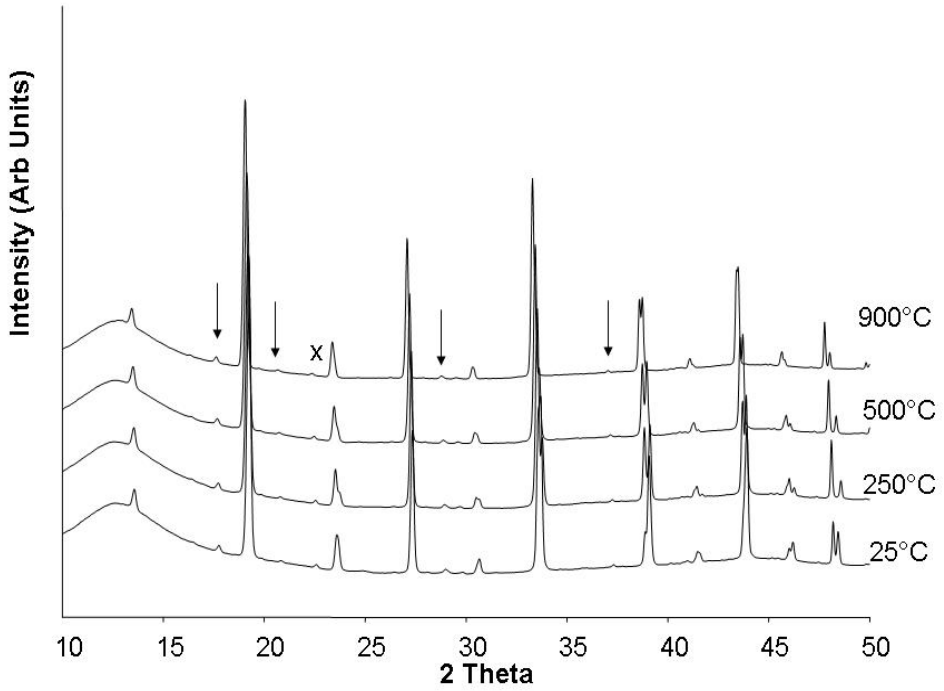

Figure 4. 43 VT XRD data collected at NSLS of LSGM4,4. Low concentrations of the impurities $SrLaGa_3O_7$ (indicated with an arrow) and $La_4Ga_2O_9$ (indicated with an x) are seen.

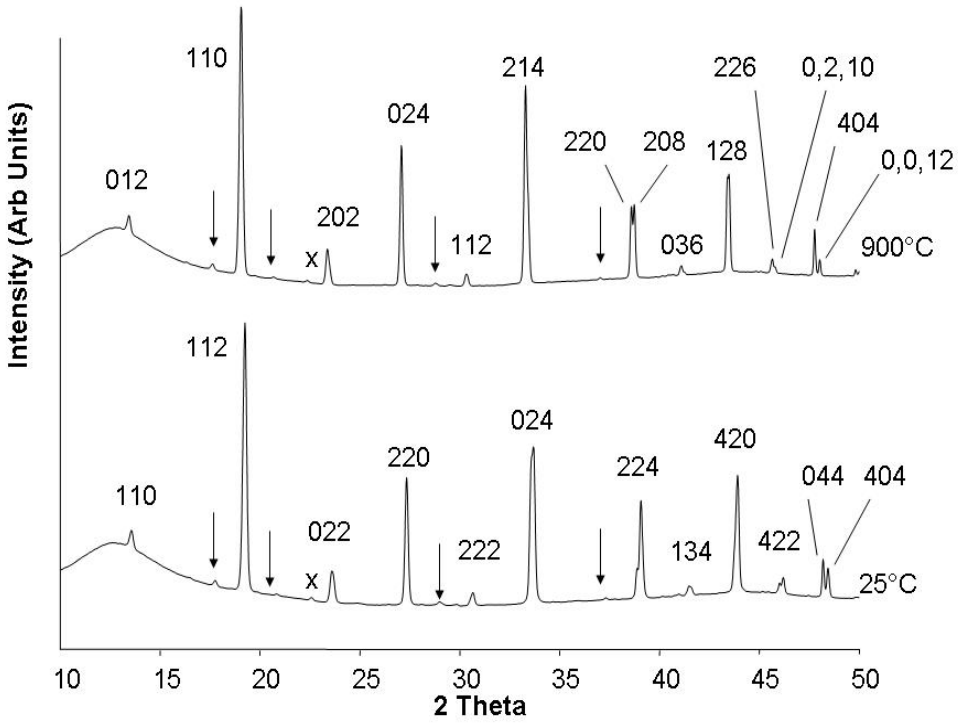

Figure 4. 44 Indexing of the room temperature and high temperature data collected at NSLS form figure 4.6. The bottom (25°C) is indexed to Pbnm space group, and the top (900°C) indexed to R-3c space group.

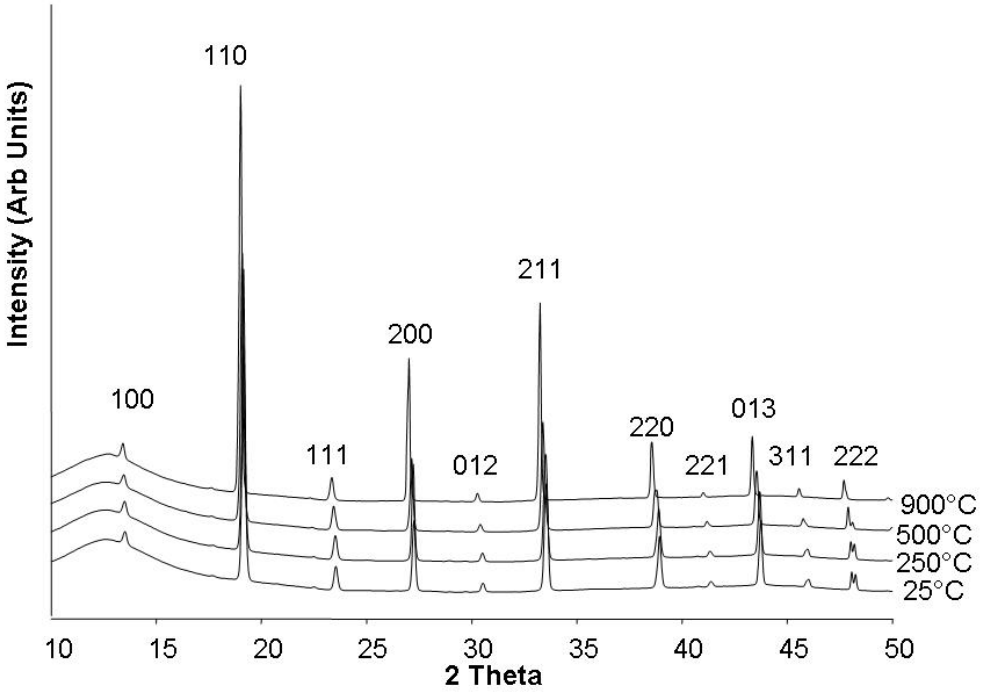

Figure 4. 45 LSGM1010 diffraction patterns collected at NSLS show cubic symmetry at 900°C and R-3c for lower temperatures. The high temperature structure is indexed to space group Pm3m.

.

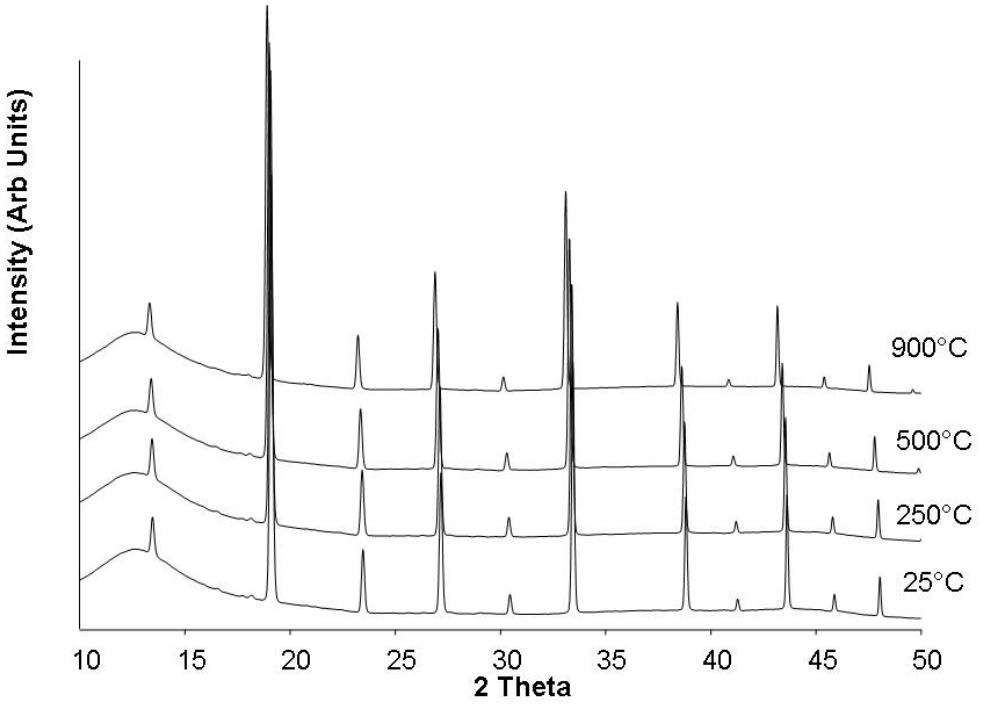

Figure 4. 46 LSGM1717 Variable temperature XRD data collected at NSLS shows a cubic crystal system from room temperature to 900°C.

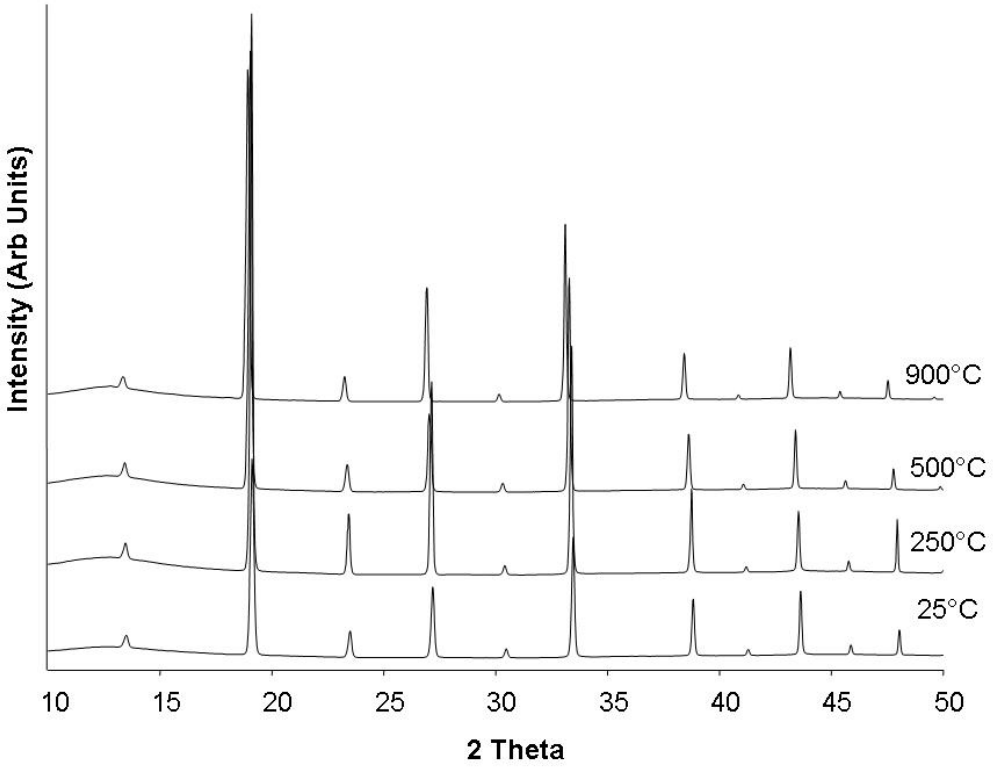

Figure 4. 47 Variable temperature XRD data collected at NSLS of LSGM2020 showing a cubic crystal structure to 900 °C..

4.3.2 ^{17}O MAS NMR Spectra

Pure $LaGaO_3$

The variable temperature spectra of $LaGaO_3$ collected at 48.8 MHz exhibit peak intensities characteristic of a 2nd order quadrupolar interaction at ~ 182 ppm (figure 4.11). However, the broad resonance seen at ~125 ppm, which does not appear in the sample synthesized by the solid state route, is not assigned. At 240°C, this feature is better resolved as the 2nd order quadrupole broadening is becoming averaged.

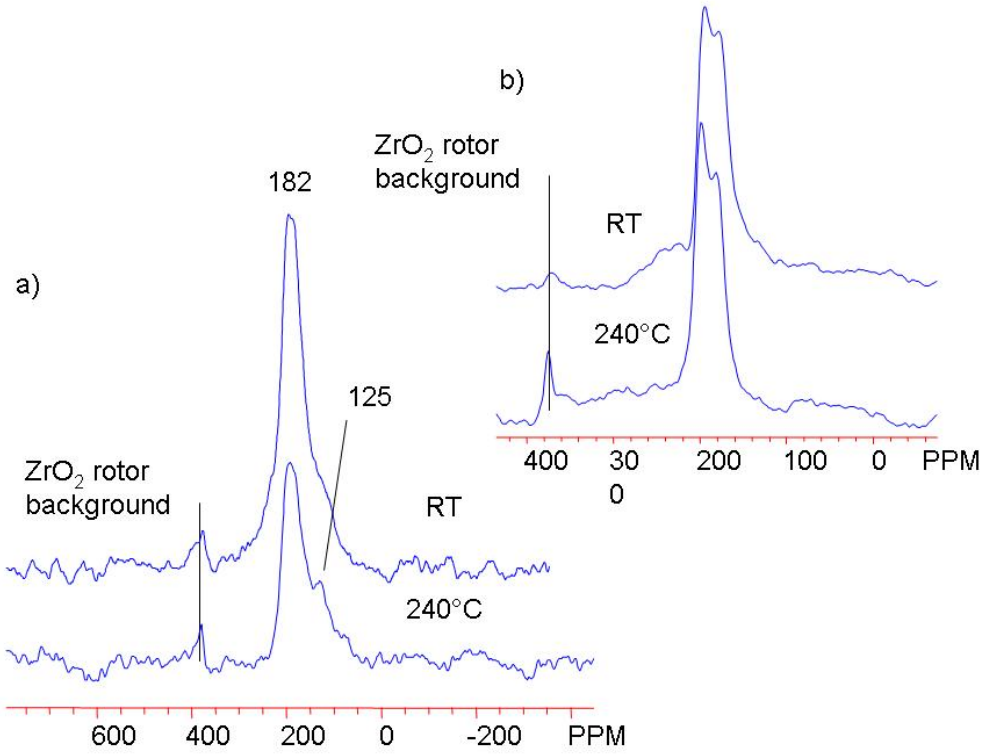

Figure 4. 48 Variable temperature (VT) ^{17}O MAS NMR spectra of $LaGaO_3$ collected at an operating frequency of 48.8 MHz. ZrO_2 background indicated at ~ 379 ppm. In a) sample made by ball milling and in b) solid state synthesis (description of synthesis can be found in Chapter 5).

LSG10

The variable temperature spectrum of 10% Sr doped $LaGaO_3$ collected at 67.7 MHz (figure 4.12) displays a single peak with a peak maximum at 203 ppm, with a full width at half maximum (FWHM) line width of approximately 2 kHz. A broad feature at low frequency is seen in the room temperature spectrum at about 150 ppm. This is suggestive of a second oxygen environment. The sidebands present in the room temperature spectrum disappear upon going to high temperature along with the broad feature at 150 ppm. The spectra at both temperatures exhibit resonances without a discernable 2nd order quadrupolar line shape, none the less which cannot be fit by a single Gaussian line, indicating some residual chemical shift distributions and 2nd order quadrupolar broadening.

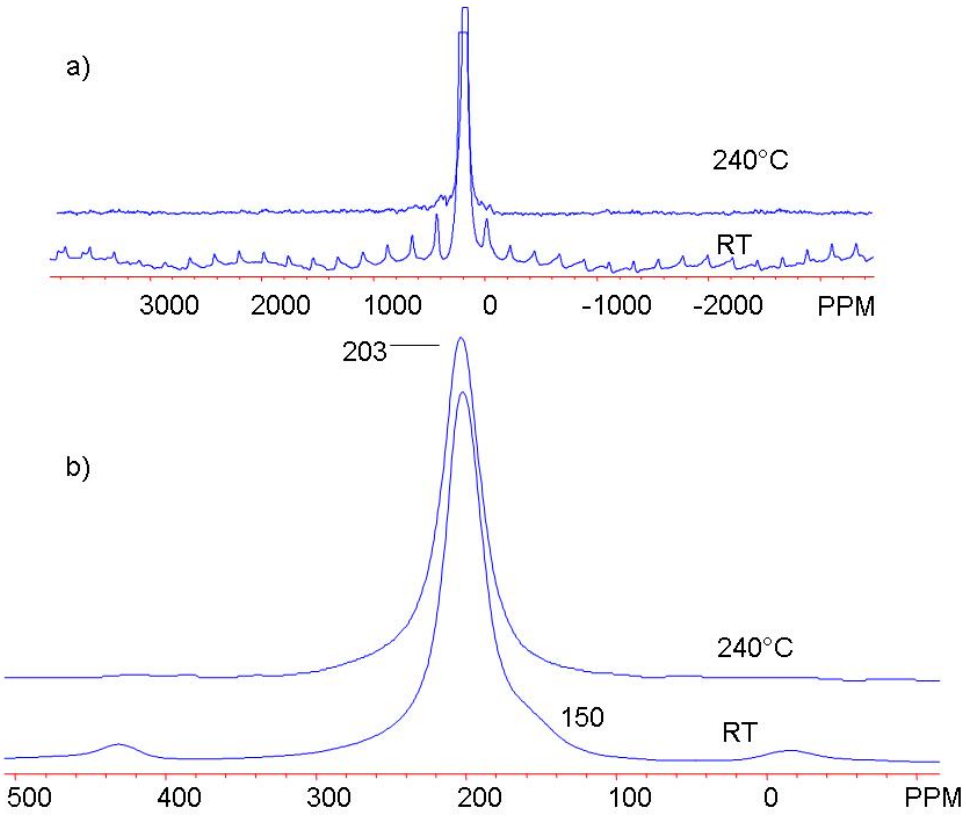

Figure 4. 49 VT ^{17}O MAS NMR of LSG10 collected at 67.7 MHz. In a) full spectrum displaying sidebands (fig 1.7) in the room temperature spectrum (bottom), and loss of spinning sidebands in the spectrum collect at 240°C (top). In b) the central transition is zoomed in and truncated to display weak broad resonance at 150 ppm in the room temperature spectrum (bottom) and the loss of it at 240°C. There is no change in the line width of the central transition upon heating, where it remains the same at 2.0 kHz.

LGM10

The room temperature and 240°C ^{17}O MAS NMR spectra of $LaGaO_3$ with 10% Mg doped at the Ga site collected at 67.7 MHz (figure 4.13) has a maximum peak intensity at 212 ppm for the high temperature spectrum vs. 206 ppm for the room temperature spectrum. Upon heating, spinning side bands are greatly reduced at the elevated temperature. The FWHM line widths are on the order of 2 kHz wide for both spectra.

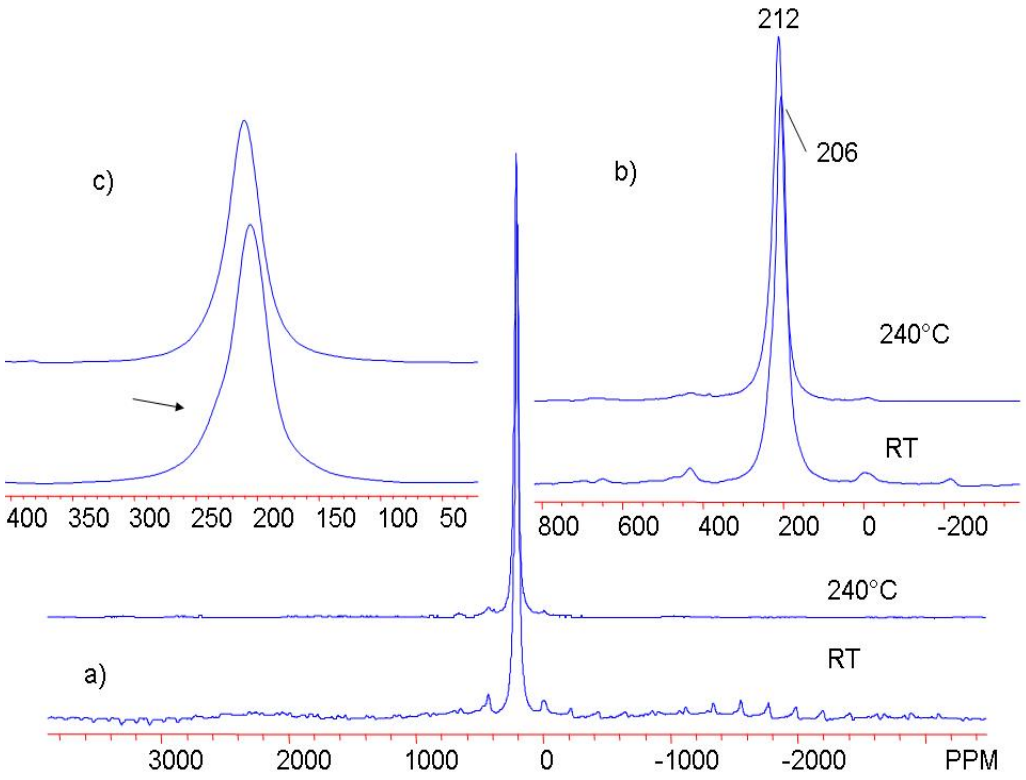

Figure 4. 50 VT ^{17}O MAS NMR of LGM10 collected at 67.7 MHz. a) Side bands present in room temperature spectrum are lost on heating. b) Line widths of the central transition remain the same at 2 kHz upon heating. There is a slight shift of the maximum peak intensity of 6 ppm going from room temperature to 240°C. In c) a weak resonance at 240 ppm is seen in the room temperature spectrum (indicated with an arrow) that disappears upon heating.

LGM20

For 20% Mg doped $LaGaO_3$, (LGM20) VT data were collected at an operating frequency of 67.7 MHz (11.7 T) and 48.8MHz (8.45 T) (figure 4.14). Starting with the lower frequency data, the maximum peak intensity of the room temperature spectrum is at 198 ppm with a FWHM of 4 kHz. The spectrum taken at the same frequency with at 240°C has maximum peak intensity at 201 ppm and a FWHM of 3 kHz. Side bands present in the room temperature spectrum are not present in the 240°C spectrum. The higher field data set follows similar trends. The maximum peak intensity of the room temperature data is at 209 ppm and a FWHM of 3.4 kHz. The spectrum at 240°C has maximum peak intensity at 216 ppm and a FWHM at 2.8 kHz.

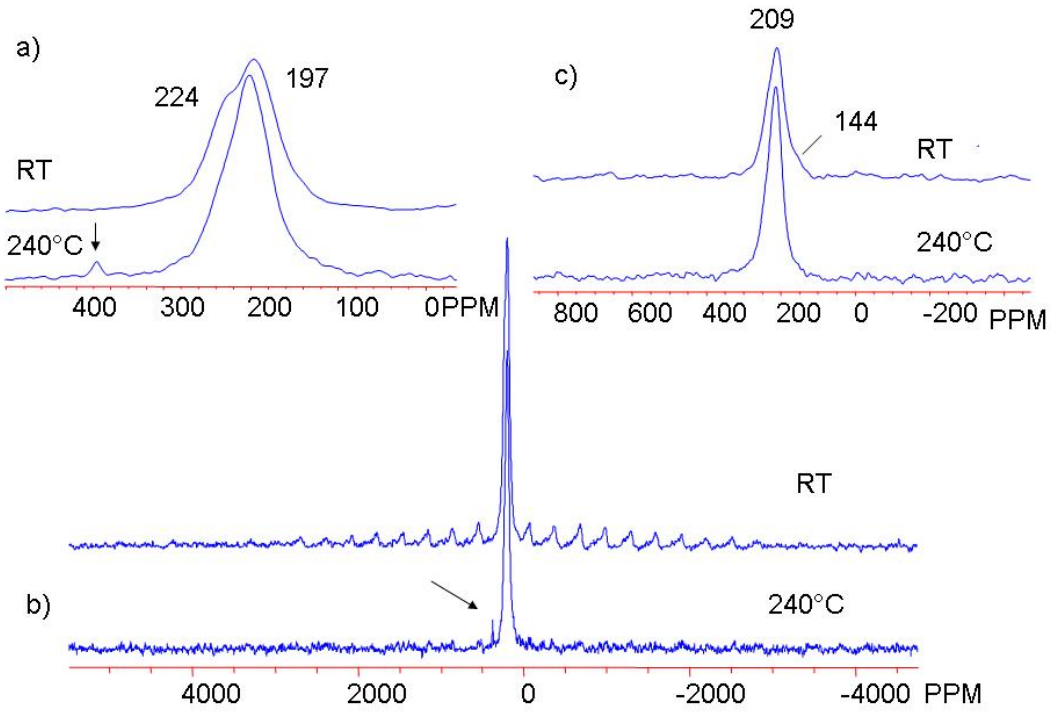

Figure 4. 51 LGM20 VT ^{17}O MAS NMR spectra collected at 48.8 (a and b) and 67.7 MHz (c). In a) line widths narrow upon heating, from 4.0 kHz to 3.0 kHz. The broad feature at 224 ppm disappears upon heating. In b) full spectrum reveals loss of sidebands upon heating as well as ZrO_2 rotor background indicated with an arrow. In c) spectra were collected at 67.7 MHz. A weak broad resonance appears to low frequency at 144 ppm. Line widths decrease from 3.4 kHz to 2.8 kHz upon heating.

LSGM4,4

Doping 4% of Sr on the La site (A site) and 4% of Mg site for Ga (B site) in $LaGaO_3$, a maximum peak intensity is found in the ^{17}O MAS NMR collected at 48.8 MHz at 196 ppm for both the room temperature and 240°C spectra (figure 4.15). In addition, a broad feature emerges at high frequency at about 226 ppm. FWHM line widths show a lie narrowing from ~2 kHz in the room temperature to ~ 1.6 kHz in the spectrum collected at 240°C. Side bands present in the room temperature spectrum disappear from the high temperature spectrum, as does the broad feature at 229 ppm.

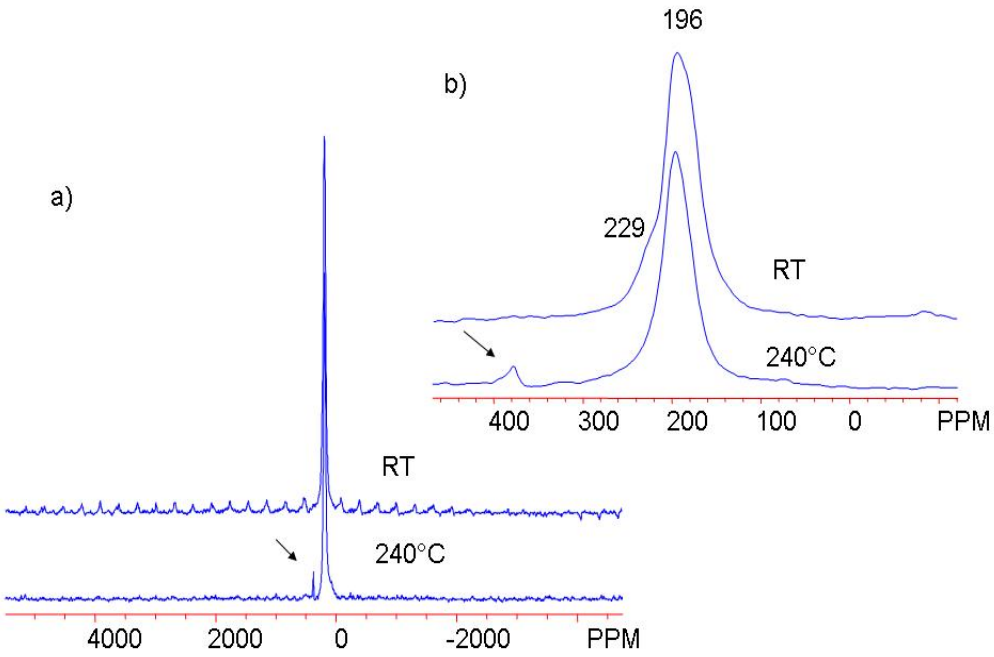

Figure 4. 52 VT ^{17}O MAS NMR spectra collected at 48.8 of LSGM4,4. In a) spinning sidebands disappear upon heating. ZrO_2 rotor background indicated with an arrow. In b), line widths decrease upon heating from 2.0 kHz to 1.6 kHz as does the weak broad resonance at 229 ppm.

LSGM1010

Doped with 10% each Sr and Mg on the A and B sites, respectively, ^{17}O MAS NMR spectra of LSGM1010 collected at 67.7 MHz show maximum peak intensity at 205 ppm for both the room temperature and 240°C spectra (figure 4.16). FWHM line widths increase from 2.8 kHz for the room temperature spectrum to 2 kHz at 240°C. In addition the room temperature spectrum exhibits a broad feature at about 155 ppm. Side bands detected in the room temperature spectrum disappear in the high temperature spectrum as does the board feature at 155 ppm

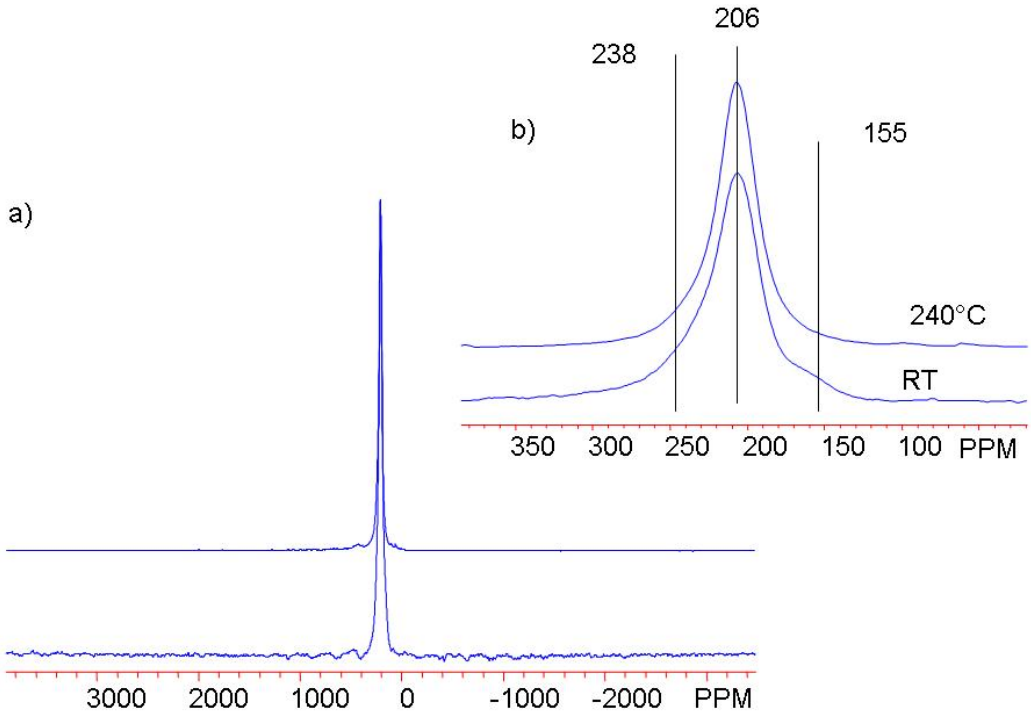

Figure 4. 53 ^{17}O MAS NMR VT spectra collected at 67.7 MHz of LSGM1010 showing loss of sidebands with heat in a) and weak broad resonance at 155 ppm disappearing with heat as well as line narrowing from 2.8 kHz at room temperature to 2.0 kHz at 240°C in b).

.

LSGM1717

The LSGM1717 ^{17}O MAS NMR variable temperature spectra collected at 67.7 MHz have maximum peak intensity at 207 ppm. The room temperature spectrum has side bands and a line width of the main resonance of ~5 kHz, while the spectrum collected at 240°C has a line width of ~4kHz with no side bands (figure 4.17).

.

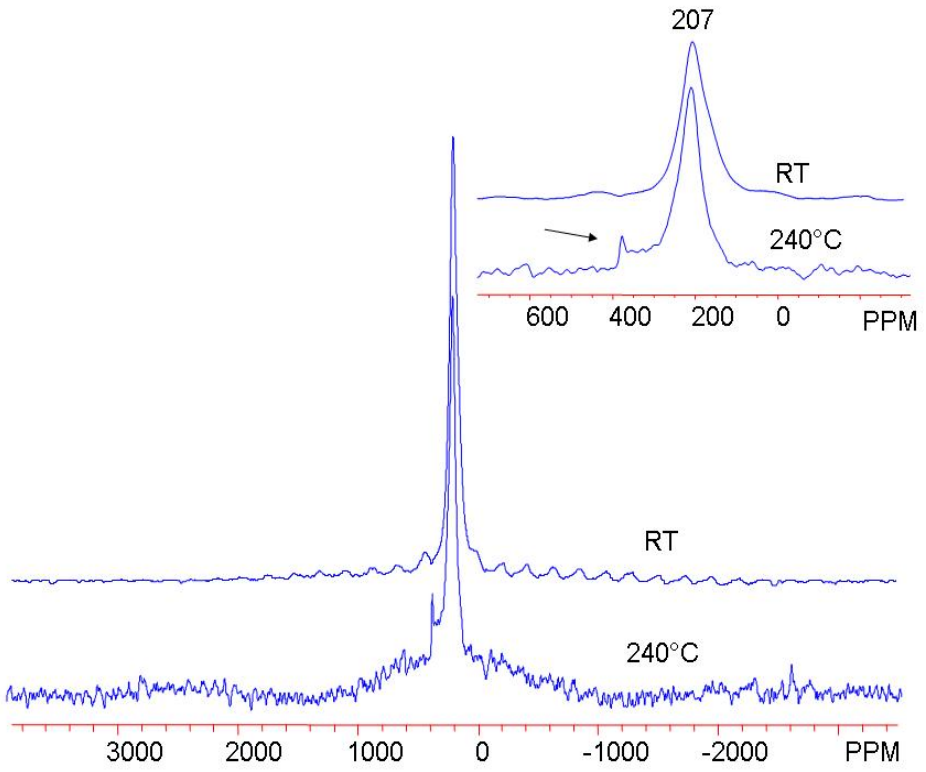

Figure 4. 54 VT ^{17}O MAS NMR of LSGM1717 collected at 67.7 MHz. In a) sidebands disappear upon heating as well as a loss of line breadth from 5.0 kHz to 4.0 kHz. In b) ZrO_2 rotor background indicated with an arrow.

LSGM2020

The LSGM2020 ^{17}O MAS NMR spectra collected at 48.8 MHz reveal line narrowing from 4.2 kHz to 3.2 kHz upon heating from room temperature to 240°C. Side bands present in the room temperature spectrum disappear at 240°C. Maximum peak intensity remains the same throughout the two temperatures at 200 ppm (figure 4.18).

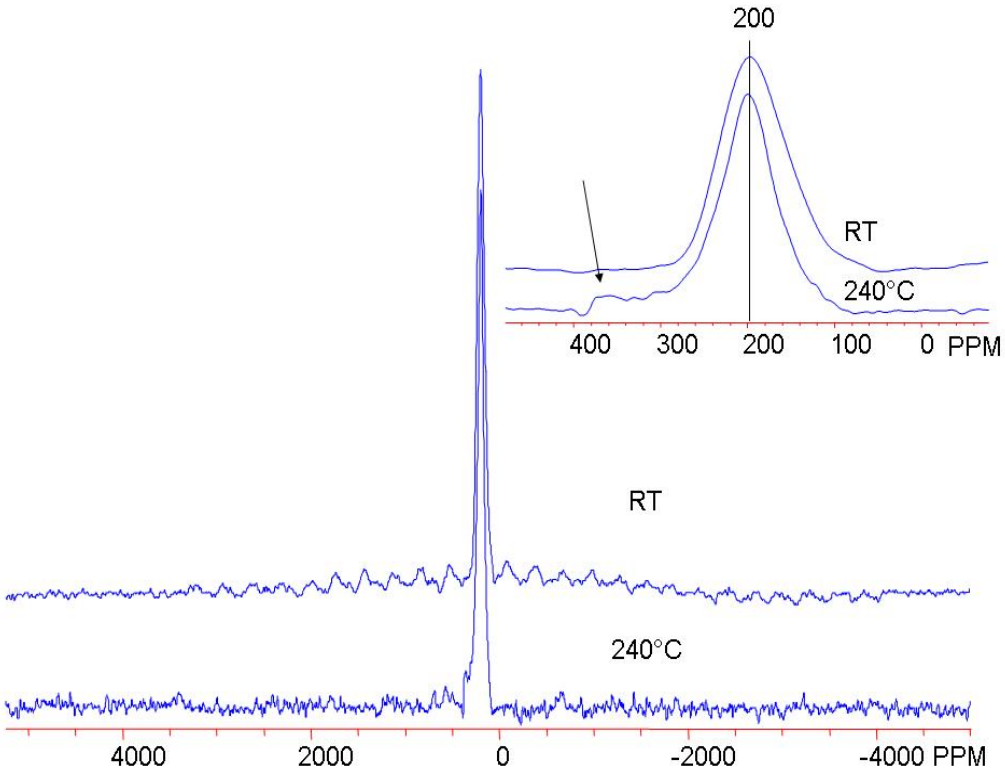

Figure 4. 55 VT ^{17}O MAS NMR of LSGM2020 collected at 48.8 MHz. In a) sidebands disappear upon heating as well as a loss of line breadth from 4.2 kHz to 3.2 kHz. In b) ZrO_2 rotor background indicated with an arrow.

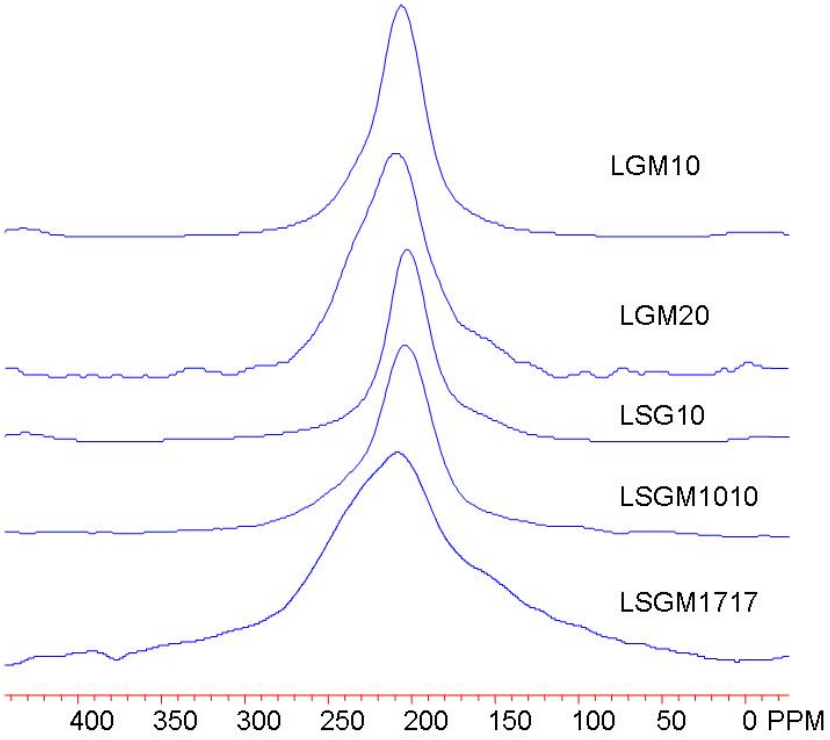

Figure 4. 56 ^{17}O NMR room temperature spectra of (top to bottom) LGM10, LGM20, LSG10, LSGM1010 and LSGM1717 collected at 67.7 MHz using a Hahn echo. This figure focuses on the central transition of the spectra.

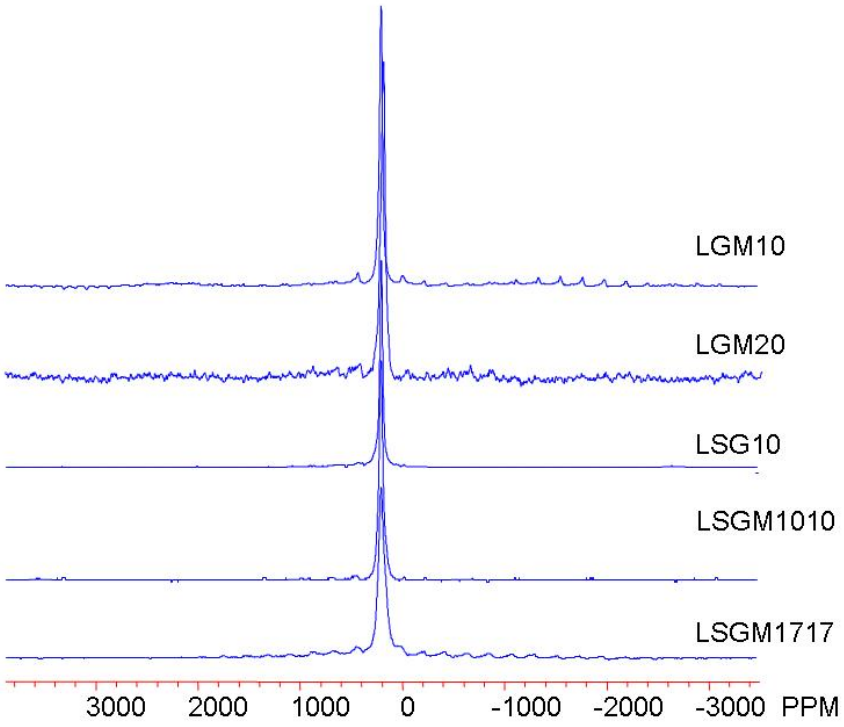

Figure 4. 57 ^{17}O NMR room temperature spectra of (top to bottom) LGM10, LGM20, LSG10, LSGM1010 and LSGM1717 collected at 67.7 MHz using a Hahn echo.

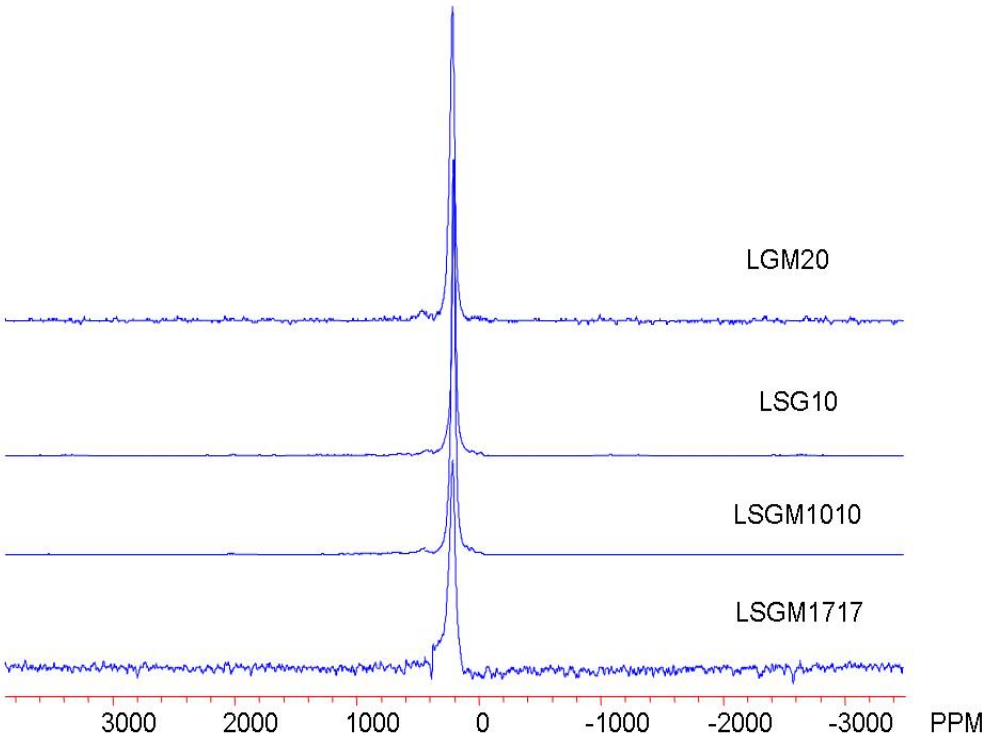

Figure 4. 58 ^{17}O NMR spectra collected at 240°C of (top to bottom) LGM10, LGM20, LSG10, LSGM1010 and LSGM1717 collected at 67.7 MHz using a Hahn echo.

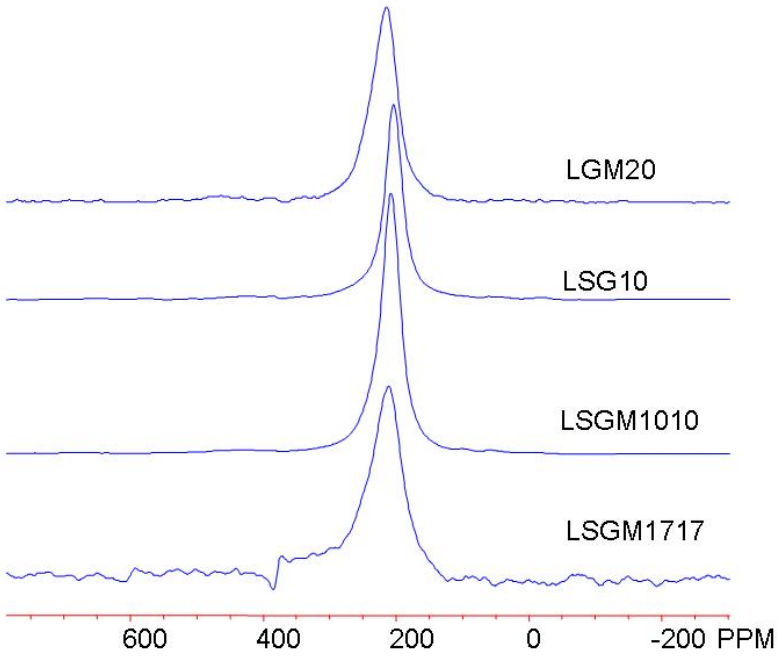

Figure 4. 59 ^{17}O NMR spectra collected at 240°C of (from top to bottom) LGM20, LSG10, LSGM1010 and LSGM1717 focusing on the central transition lineshape. Data collected at 67.7 MHz using a Hahn echo.

4.3.3 ^{71}Ga MAS NMR spectra:

Pure $LaGaO_3$

The ^{71}Ga NMR spectra of $LaGaO_3$ collected at 109.7 MHz have maximum peak intensity at 50 ppm. The line widths increase upon heating, such that the room temperature spectrum has a line width of 1.3 kHz and the spectrum collected at 240°C has a line width of 1.4 kHz. Spinning sidebands are present in both spectra (figure 4.23).

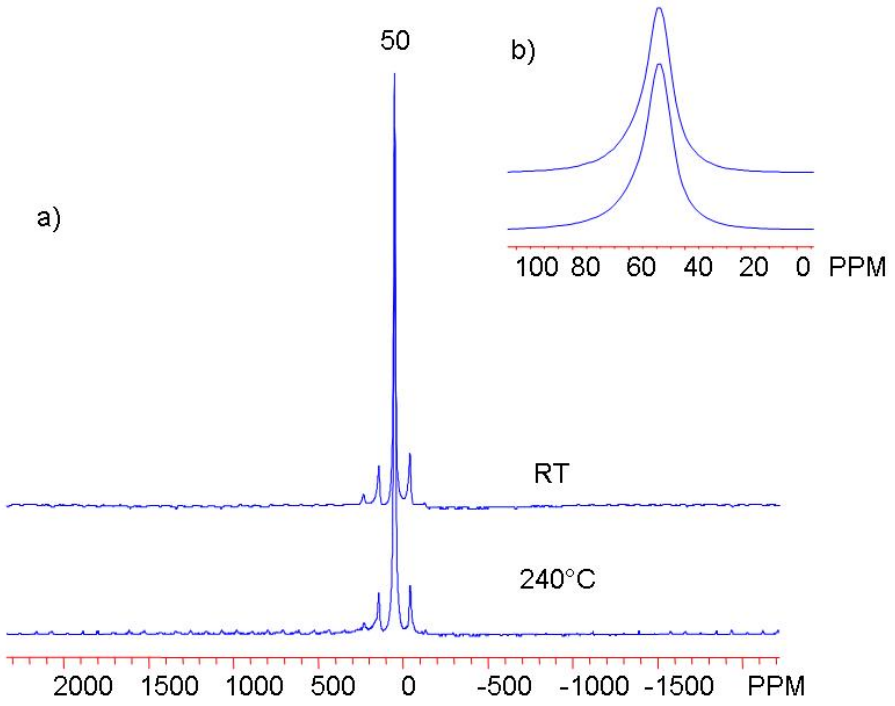

Figure 4. 60 ^{71}Ga MAS NMR VT spectra $LaGaO_3$ colleted at 109.7 MHz. Maximum peak intensity at 50 ppm in a). In b), a close up of the central transition line shape reveals no significant difference upon heating, except for a slight increase in line width from 1.3 kHz to 1.4 kHz.

LSG10

The ^{71}Ga NMR spectrum of LSG10 collected at 109.7 MHz shows subtle broadening at 103 ppm, which is to higher frequency of the main resonance peak at 43 ppm (figures 4.24 & 4.25). The room temperature spectrum and the 240°C ^{71}Ga spectra of this compound both have maximum peak intensity at 46 ppm with FWHM line widths of 2.7 (room temperature) and 3 kHz (240°C). The overall character of the line shapes in both spectra have tails toward the lower frequency which are characteristic of distributions in 2nd order quadrupolar interaction [19]. Both have spinning sidebands, but in the high temperature spectrum, a broad feature of low intensity emerges at 103 ppm.

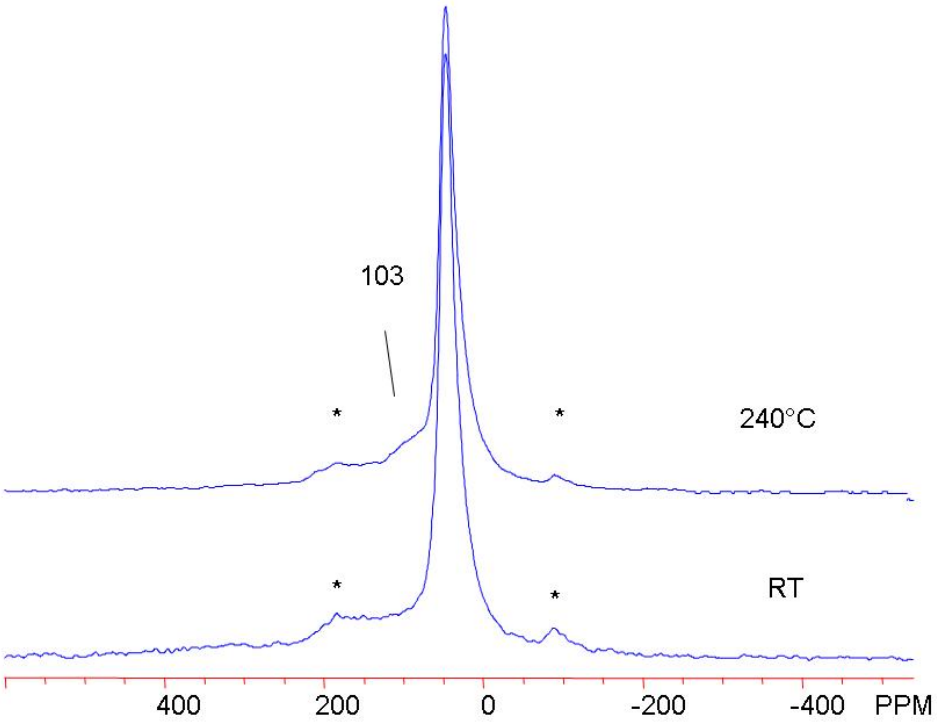

Figure 4. 61 VT spectra of ^{71}Ga MAS NMR of LSG10 showing the emergence of a weak resonance at 103 ppm at 240°C.

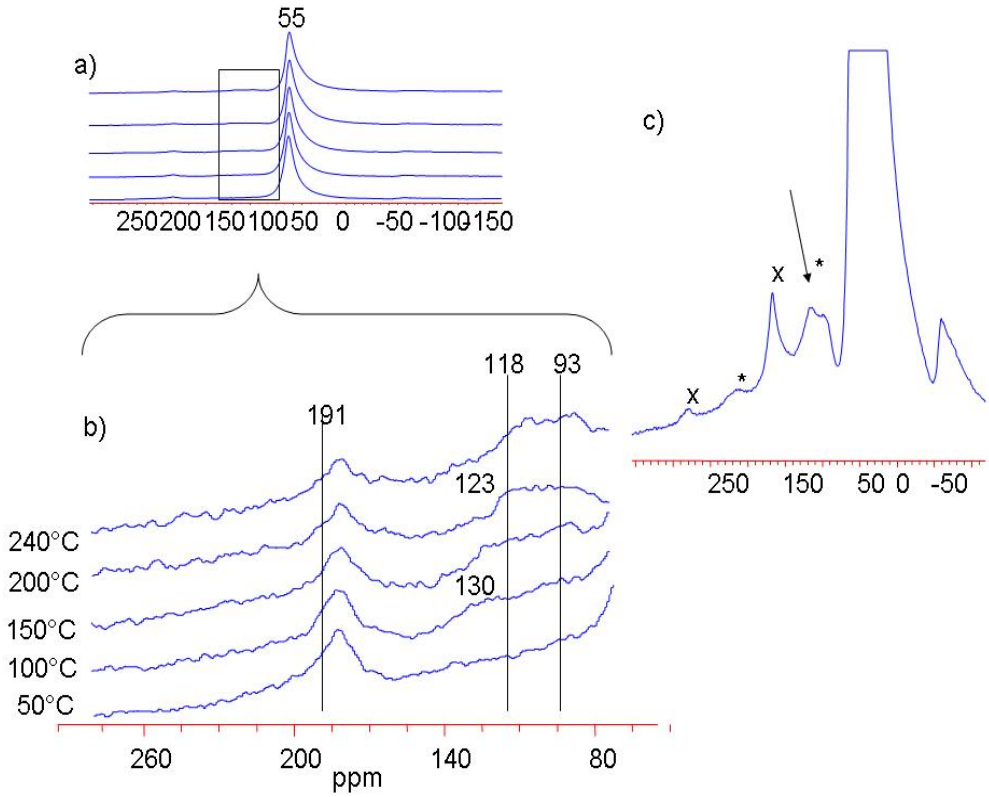

Figure 4. 62 VT spectra of ^{71}Ga MAS NMR of LSG10 collected in 50°C intervals at 152.9 MHz (a) showing the evolution of the broad weak resonance (zoomed in on in b). In c) a higher resolution spectrum illustrating second Ga environment (indicated with an arrow) with spinning sidebands (asterisks show sidebands of second environment and x sidebands of the main resonance).

LGM10

The ^{71}Ga NMR spectra of LGM10 (figures 4.26 and 4.27) collected at 109.7 MHz have a maximum peak intensity at 48 ppm and line width increases from 1.7 kHz at room temperature to 1.9 kHz at 240°C. For both spectra, a high frequency resonance appears. However, at room temperature, this resonance appears at 116 ppm while at 240°C it appears at 87 ppm. The variable temperature data set collected at 152.9 MHz have a maximum peak intensity at 54 ppm and show a similar broad resonance to high frequency as the data collected at 109.7 MHz. However, the broad resonance at room temperature for the high field data, this resonance appears at 129 ppm and has small sidebands. In the spectrum collected at 240°C, it is at 103 ppm with no visible sidebands.

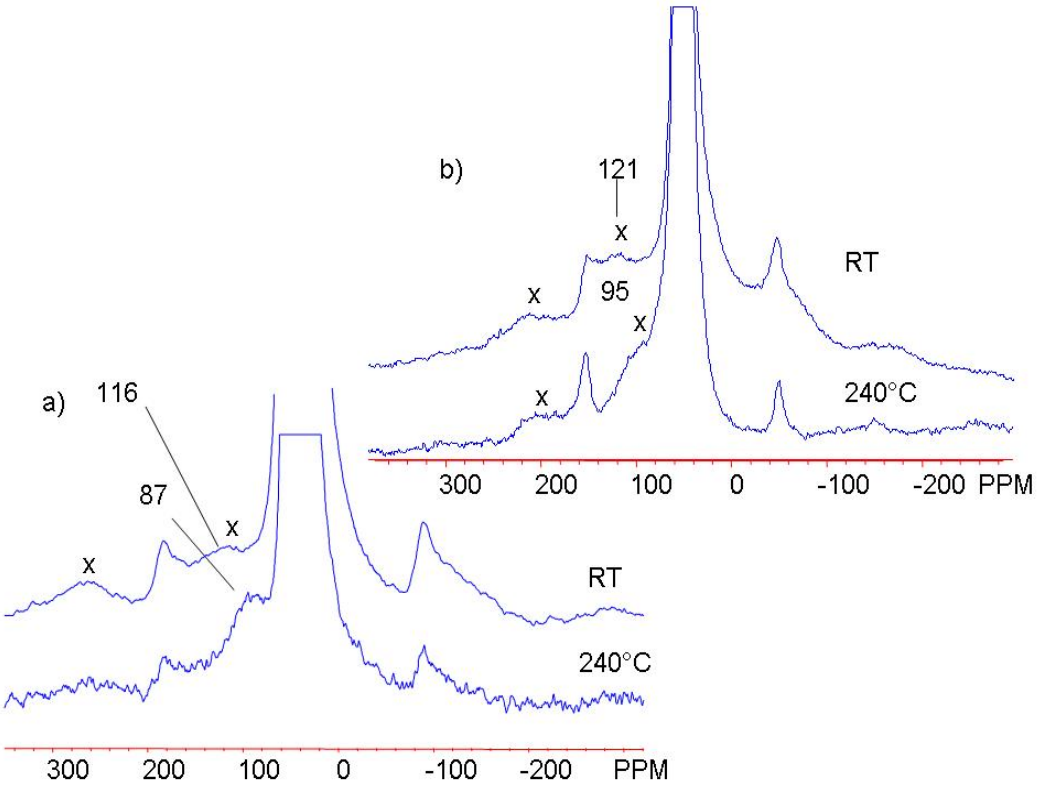

Figure 4. 63 VT Hahn echo spectra of ^{71}Ga MAS NMR of LGM10 at 109.7 (a) and 152.9 (b) MHz showing the emergence of a similar resonance at both room temperature and 240°C. In a) low frequency tail shows distributions in 2nd order quadrupolar interactions. In b) close up of second Ga environment at 103 ppm at 240°C (tom) and ~129 at room temperature. Asterisks and x indicate sidebands of the respective isotropic resonances.

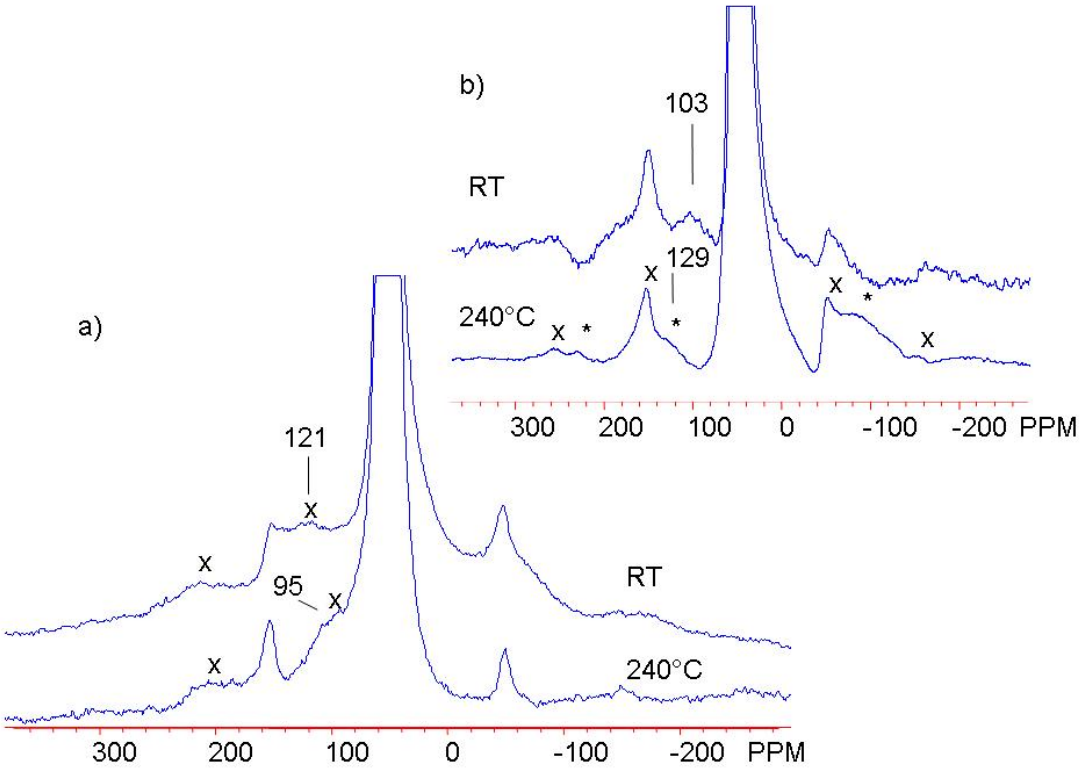

Figure 4. 64 Same as figure 21 (LGM10), except that in a) a Hahn echo was used to collect the spectra and in b) a 1 pulse pulse sequence was used. Asterisks and x indicate sidebands of the respective isotropic resonances.

LGM20

Data collected at 109.7 MHz at both room and 240°C display line shapes that describe distributions in 2nd order quadrupolar interaction, where a low frequency tail is evident. For both temperatures, broad side bands are evident as is unchanging maximum peak intensity at 43 ppm. From room temperature to high temperature, line narrowing is evident from the FWHM going from 4.4 kHz to 3.2 kHz (figure 4.28).

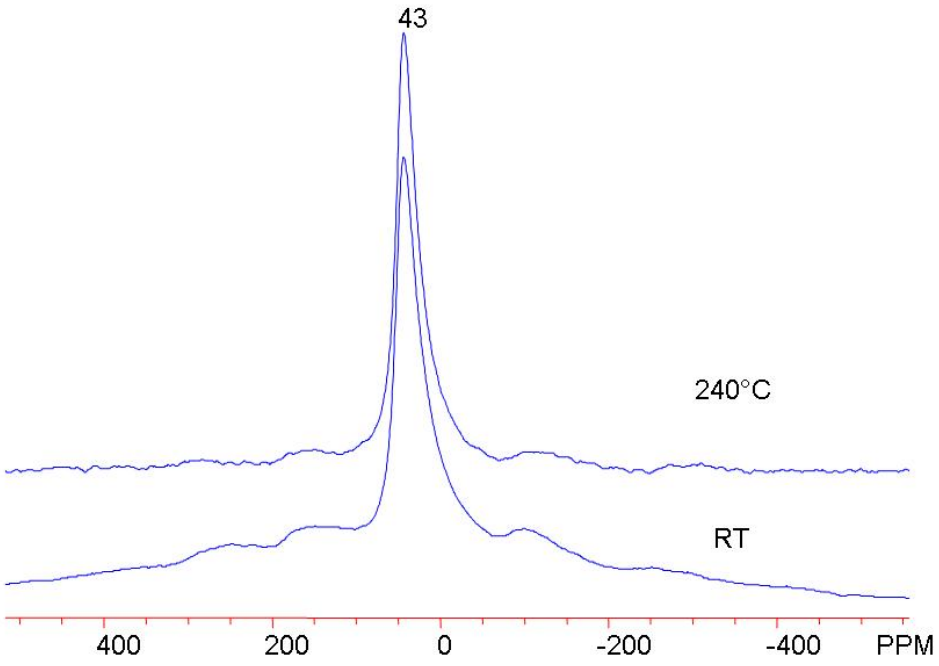

Figure 4. 65 ^{71}Ga MAS NMR data of LGM20 collected at 109.7 MHz. Room temperature spectrum (bottom) has a broad baseline which reduced in the spectrum collect at 240°C (top).

LSGM4,4

Variable temperature ^{71}Ga NMR spectra collected at 152.9 MHz using a Hahn echo pulse sequence all have a maximum peak intensity of 54 ppm and the line widths of both the room temperature spectrum and the 240°C spectrum have the same line width of 1.7 kHz. The room temperature spectrum, however, has a broad feature, similar to the LGM10 and LSG10, where the maximum peak intensity is at ~ 126 ppm with discernable side bands. Upon heating, this resonance appears at ~ 100 ppm. The data collected at the same field using a single pulse pulse-sequence shows this broad intensity more readily in the high temperature spectrum, where this resonance appears to have a symmetric ($\eta \approx 0$, eqn 1.3) 2nd order quadrupolar line shape (figure 4.29).

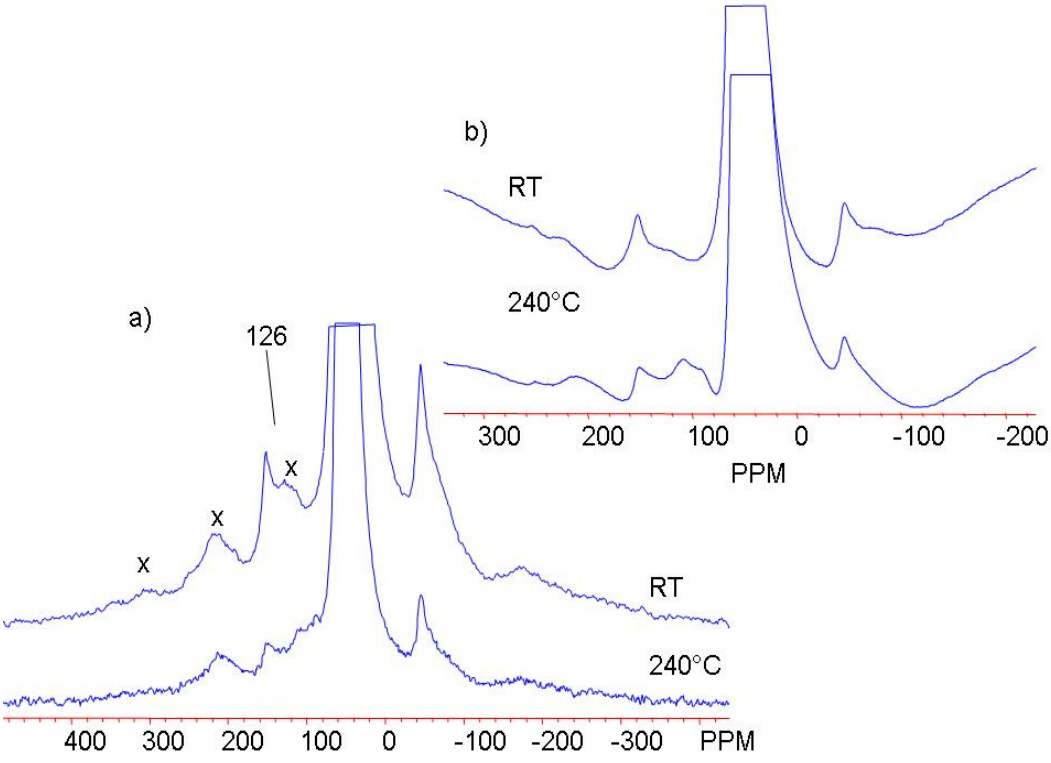

Figure 4. 66 ^{71}Ga MAS NMR data of LSGM4,4 collected at 152.9 MHz. In a) a Hahn echo pulse sequence was used and in b) a 1 pulse pulse sequence.

LSGM1717

Data collected at 109.7 MHz follow a similar trend as ^{71}Ga NMR of LGM20 differing in the widths of the lines, increasing with increasing temperature from 5.2 kHz to 6.2 kHz at 240°C (figure 4.30).

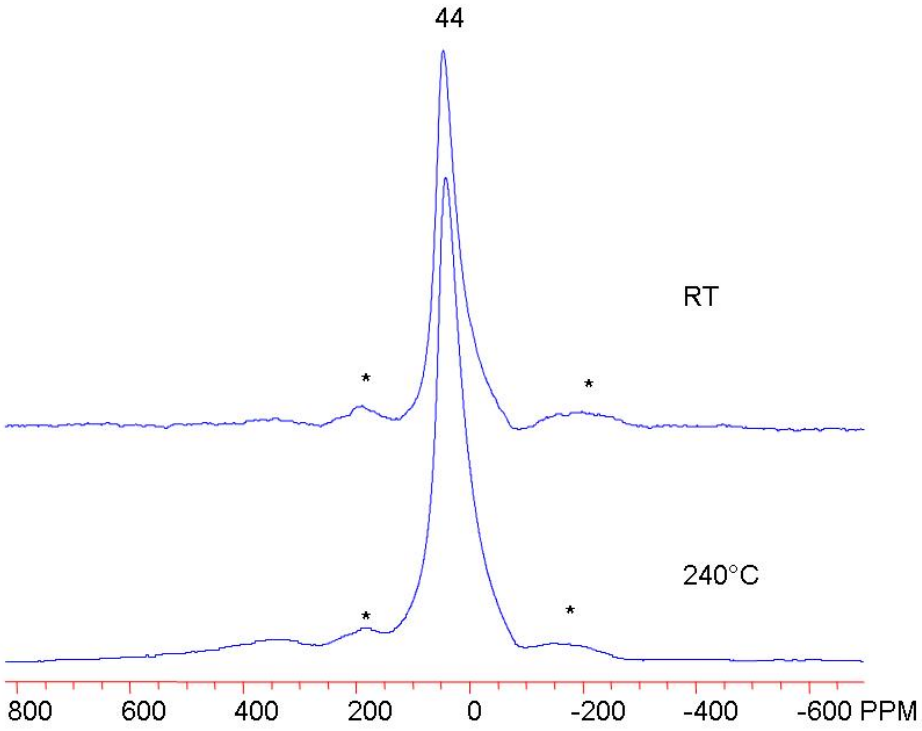

Figure 4. 67 ^{71}Ga MAS NMR data of LSGM1717 collected at 109.7 MHz using a 1 pulse pulse sequence. Asterisks indicate spinning sidebands.

LSGM2010

LSGM2010 ^{71}Ga NMR spectra collected at 109.7 MHz show the same low frequency tail characteristic of distributions in 2nd order quadrupolar interaction (fig 4.31). Noticeable differences in this data set are the increase of line width from 4 kHz at room temperature to 6 kHz at 240°C. XRD reveal small levels of $SrLaGaO_3$ impurity.

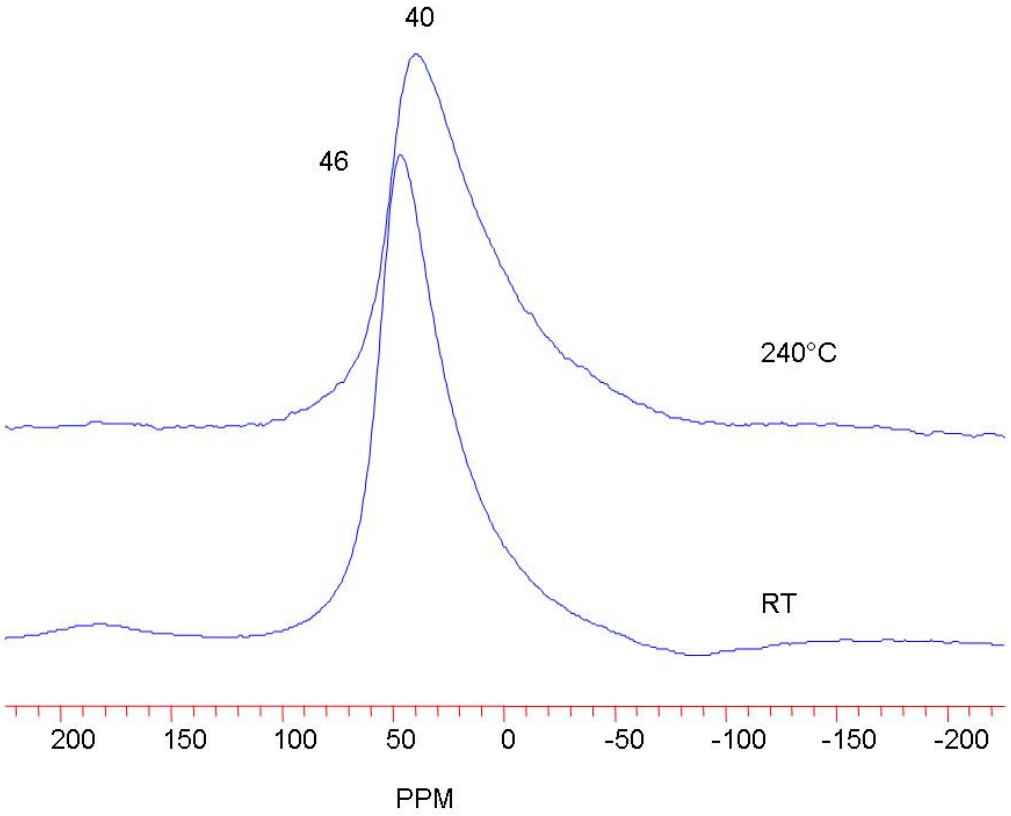

Figure 4. 68 ^{71}Ga MAS NMR data of LSGM2010 collected at 109.7 MHz. Heating to 240°C increases the line width and shifts the maximum peak intensity toward higher frequency as seen from the zoom image of the central transition.

LSGM2020

LSGM2020 ^{71}Ga NMR VT spectra show an increase in line width upon heating from 5.2 kHz to 6.0 kHz. The room temperature spectrum has a very broad feature in the baseline measuring about 2.2 MHz whereas in the 240°C spectrum it is reduced to about 60 kHz. Spinning sidebands are present in both spectra (figure 4.32).

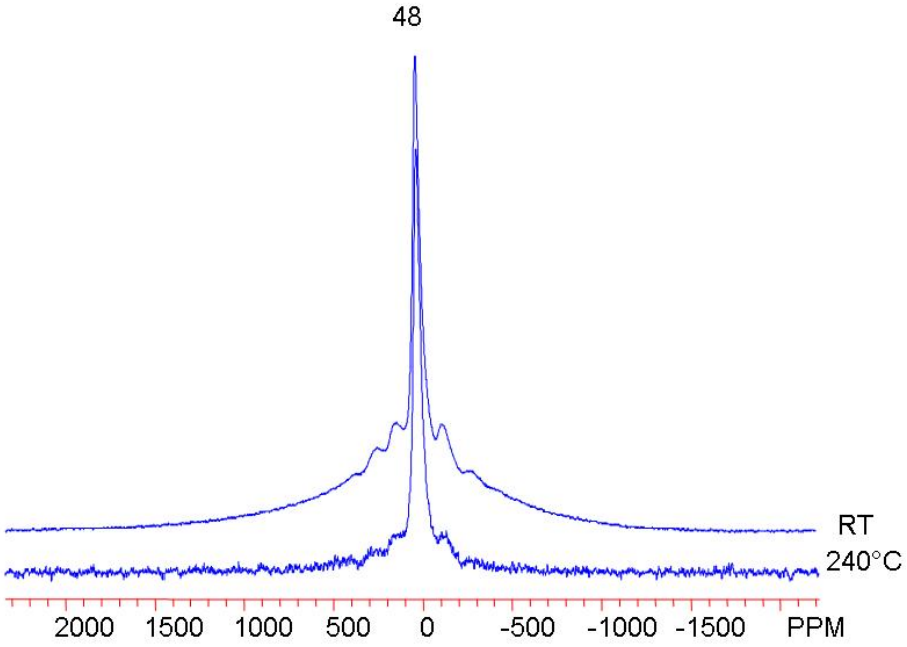

Figure 4. 69 ^{71}Ga MAS NMR data of LSGM2020 collected at 109.7 MHz. Room temperature spectrum has a very broad base line that is lost upon heating. Maximum peak intensity is at 48 ppm for both spectra.

LSG5

Data collected at 152.9 MHz using a 3.2 rotor spinning at 20 kHz reveal similar broad weak resonances at ~114 and 92 ppm as seen in figure 4.33.

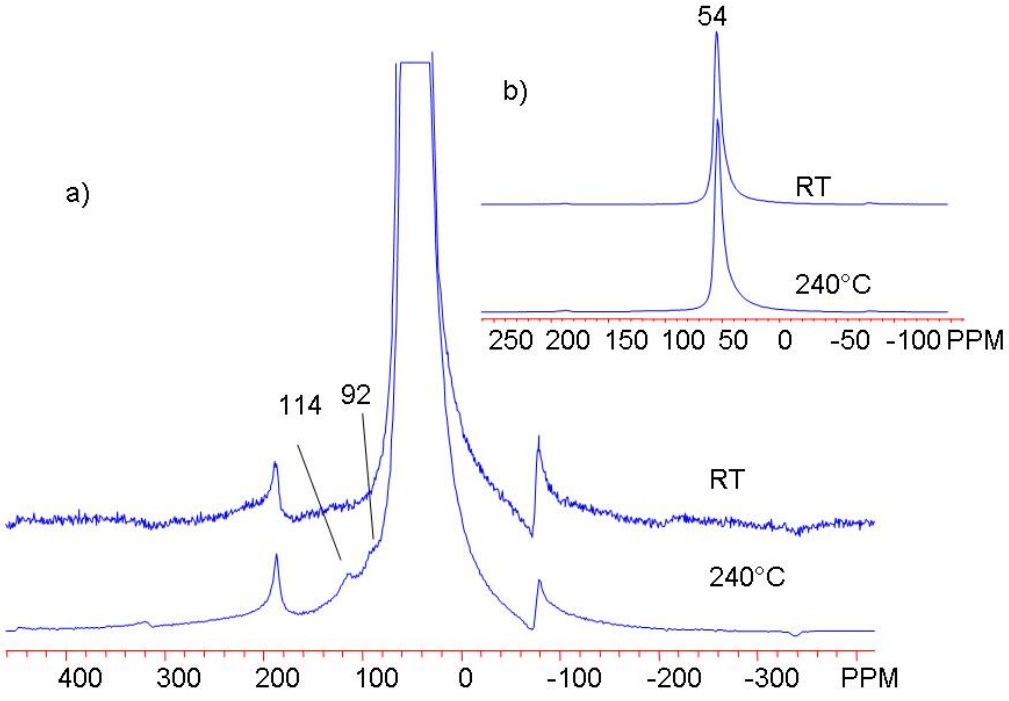

Figure 4. 70 ^{71}Ga MAS NMR data of LSG5 collected at 152.9 MHz using a 3.2mm rotor and a spinning speed of 20 kHz. Similar broad weak resonances to higher frequency can be seen in (a) as in LSG10, LGM10, and LSGM4,4. In b) full spectral window shown.

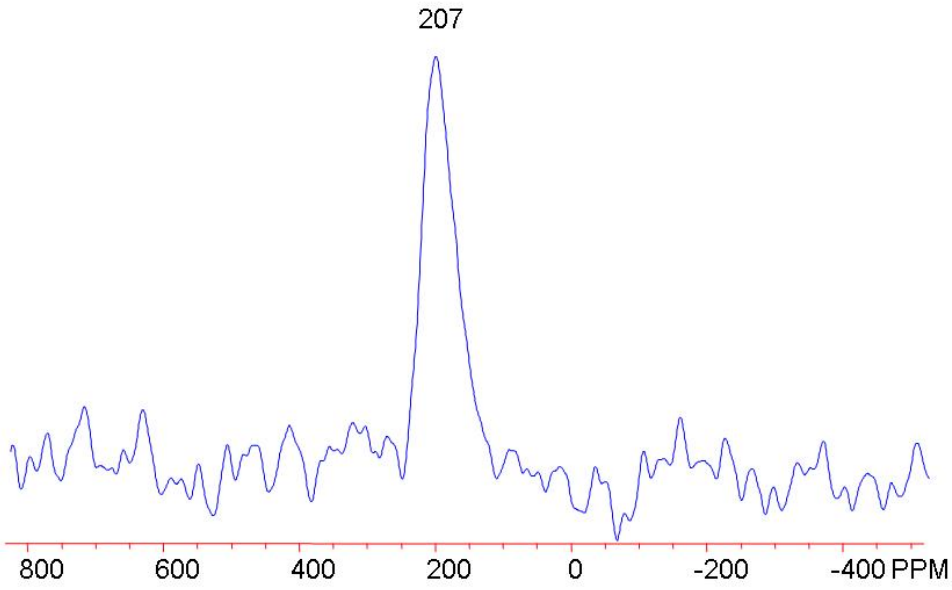

Figure 4. 71 ^{71}Ga MAS NMR spectra of $SrLaGa_3O_7$, a common impurity in these compounds, collected at an operating frequency of 152.9MHz. The main isotropic resonance is at 207 ppm.

4.4 Discussion

4.4.1 ^{17}O NMR

4.4 Discussion

4.4.1 ^{17}O NMR

The ^{17}O NMR spectra of pure $LaGaO_3$ in figure 4.11 have an isotropic resonance at 182 ppm. The additional resonance at ~125 ppm is attributable to β - Ga_2O_3 impurity (see chapter 5 for the ^{17}O NMR characterization of β - Ga_2O_3) as detected in the XRD (figure 4.2). In chapter 5, stoichiometric $LaGaO_3$ synthesized via the solid state route is presented, along with values of η and the QCC for ^{17}O determined by simulation (0.3 (±0.02) and 3.1 (±0.2) MHz, respectively). The value of the QCC for ^{17}O does not change when the compound changes phase. QCC values of the samples synthesized via the solid state route and the mechanochemical route are assumed to be similar since the line widths of the central transition are approximately equal. QCC

values for the mechanochemically synthesized material cannot be simulated due to the featureless line shape, in part because these data were acquired at higher fields. Details of the differences will be further discussed in chapter 5.

Due to the doping of divalent cations for trivalent cations, all of these compounds have a degree of disorder due vacancies induced by charge compensation. Of all the samples studied here, LSG10, LGM20, LSGM4,4, LSGM1010 exhibit suggestions of a second oxygen environment at room temperature. These features cannot be fit with a single line overlapped with the main resonance of the spectra. In general, the lines of these spectra have peaks either to low frequency of the main resonance (LSG10, LSGM1010) or to high frequency (LGM20, LSGM4,4). Upon heating to 240°C, all of these discontinuities disappear, as do the spinning sidebands, suggesting ionic movement [23, 24] at these temperatures. The oxygen motion prohibits refocusing under the conditions of the echo pulse sequence and the side bands are lost. The process of oxygen motion is reflected in the width of the powder pattern. The magnitude of the rate of motion can be calculated from the square of the ratio of the spinning speed to the spectral width ($\delta\omega_0$) [24]. All the ^{17}O NMR spectra except for LSG10 and LGM10 exhibit line narrowing [23], which is another suggestion of oxygen motion (LSG10 and LGM10 line widths stay the same upon heating).

In references [9, 10] vacancy ordering was observed at temperatures lower than 500°C limiting the degree of oxygen mobility. However, the oxygen motion increases significantly above 500°C. In figure 4.20, the ^{17}O NMR spectrum of LSGM1717 exhibits more than one broad resonance, all of which overlap at about 207 ppm. The XRD in figure 4.9 of the same compound indicates that the structure is cubic. Compounds having cubic symmetry have only one unique crystallographic site, and thus, in principle one *average* oxygen environment. Furthermore, $LaGaO_3$ has GaO_6 corner sharing octahedra with a Ga-O-Ga bond angle of 180°. The appearance of different resonances in the ^{17}O NMR spectrum, however, indicates multiple unique oxygen local environments reflecting differences in the short range order. These cooperative displacements [25] would appear as different oxygen environments, detectable by ^{17}O NMR, and lower the symmetry from cubic as seen from the XRD. Therefore the proposed cooperative displacement model does not account for the resonance seen in the room temperature ^{17}O NMR spectrum. Ga –O-Ga bond bending is responsible for the different ^{17}O NMR resonances in the room temperature spectrum.

The high temperature spectrum exhibits effects of oxygen motion through the loss of spinning side bands [24] and motional narrowing [23]. However, in [4], slight increases in bond distances of Ga-O1- Ga from room temperature to 250°C are reported which begin to suggest the onset of thermal anisotropic displacement. It is a combination of these effects, the thermal anisotropy, evident from increase of the Ga-O bond length from the neutron refinements,

and loss of side bands and motional narrowing that are evident in the high temperature ^{17}O NMR spectrum of LSGM1717 in figure 4.22.

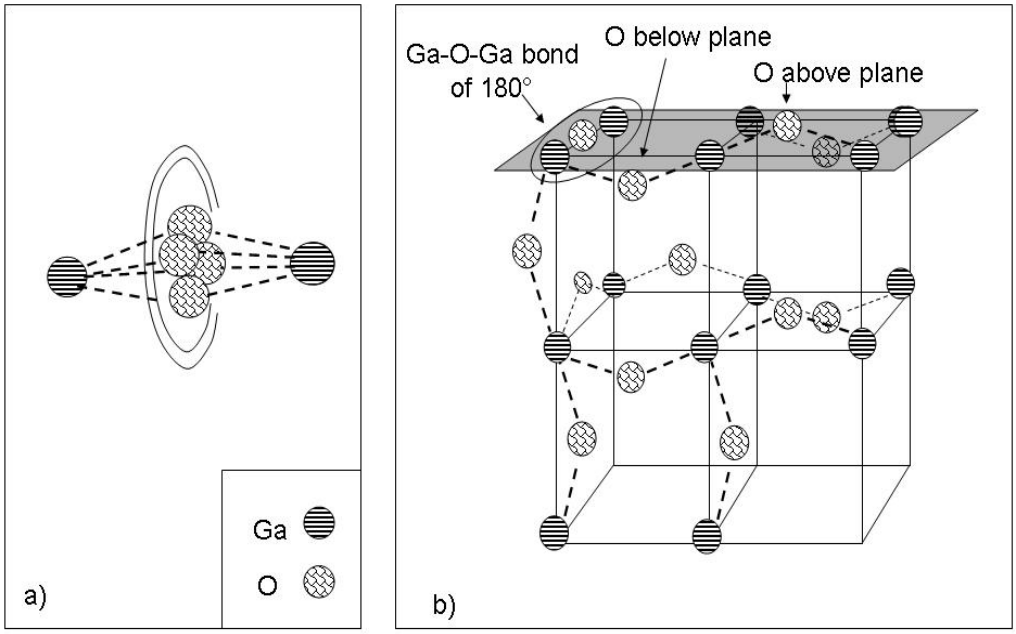

Figure 4. 72 Cartoon depicting the two models of structural ordering. In (a) the dynamic anisotropic model where the ring indicates the path of motion. In (b) the static cooperative disorder model depicts alternating displacements where the bonds average out to be linear in an XRD.

4.4.2 ^{71}Ga NMR

For pure $LaGaO_3$ synthesized via the solid state route (chapter 5), the phase change of this compound at ~150°C is evident in the increase of the QCC from 150°C to 200°C (1.4 to 1.7MHz). The differences between the ^{71}Ga spectra of the mechanochemically synthesized $LaGaO_3$ and solid state synthesis of $LaGaO_3$ will be discussed in chapter 5. The predominant resonance in all of the ^{71}Ga NMR spectra in this study is assigned to 6 coordinate Ga. This resonance exhibits a line shape that is characteristic of distributions in 2nd order quadrupolar interactions, where a low frequency tail is present to varying degrees [24]. In addition, LGM10, LSG10, and LSGM4,4 exhibit weak resonances to high frequency of the main resonance which is where the majority of the following discussion will focus. The effect of doping into these systems creates oxygen vacancies. These vacancies affect Ga such that the coordination number of Ga decreases from 6. 4 and or 5 coordinate Ga is

then expected. Previous workers have compare the ^{71}Ga NMR of compounds with Ga in 4 and 5 coordinate environments with the ^{27}Al NMR spectra of similar aluminates. The trend of coordination environment to chemical shift has a linear relationship for ^{27}Al and ^{71}Ga as shown in [26]. However, Ga coordinate environments of 4 and 5 have not been thoroughly characterized in the literature. Massiot *et al* in[26] have characterized some 4, 5 and 6 Ga coordinate environments. In their study, 6 coordinate Ga has a chemical shift range of -6 to 74 ppm while 4 coordinate Ga resonates at 100 to 250 ppm and the single example of 5 coordinate Ga at 75 ppm in $LaGaGe_2O_7$. In another study, 4 and 6 coordinate environments of Ga in β-Ga_2O_3 were found to have chemical shifts of 200 and 40 ppm, respectively [27]. The following assignments are made by using these general resonance ranges.

The ^{71}Ga NMR room temperature spectrum of LSG10 (fig 4.24) exhibits a very broad, low intensity feature hardly visible between the main resonance at 46 ppm, and the high frequency spinning sideband. This is due to 4, 5 and 6 coordinate Ga as a result of oxygen vacancies. Upon heating, oxygen vacancies begin to become mobile and the material increases in disorder [10]. In [10], as heat is introduced into the system, regions of lower symmetry were observed in a High Resolution Transmission Electron Microscopy (HRTEM) study of LSGM2015. These lower coordination environments were likened to tetrahedral layers in the Brownmillerite structure (figure 4.36a) [10]. The Brownmillerite structure consists of alternating layers of corner sharing GaO_6 octahedra separated by GaO_4 tetrahedra. The perovskite structure is similar to the Brownmillerite structure in that it contains GaO_6 octahedra that are corner sharing. Another suggested model of the ordering of oxygen vacancies shows that the vacancies order to an extent on the O2 (apical) site (figure 4.36b) [4]. In both models, the vacancies are ordered in planes twice that of the cubic perovskite lattice parameter. It is interesting to note how in the Brownmillerite model, where the vacancies are in adjacent equatorial positions (O1), produce a GaO_4 tetrahedron, whereas the vacancies ordered on the O2 apical site do not, yet the spacing of the vacancies remains twice that of the cubic perovskite lattice parameter.

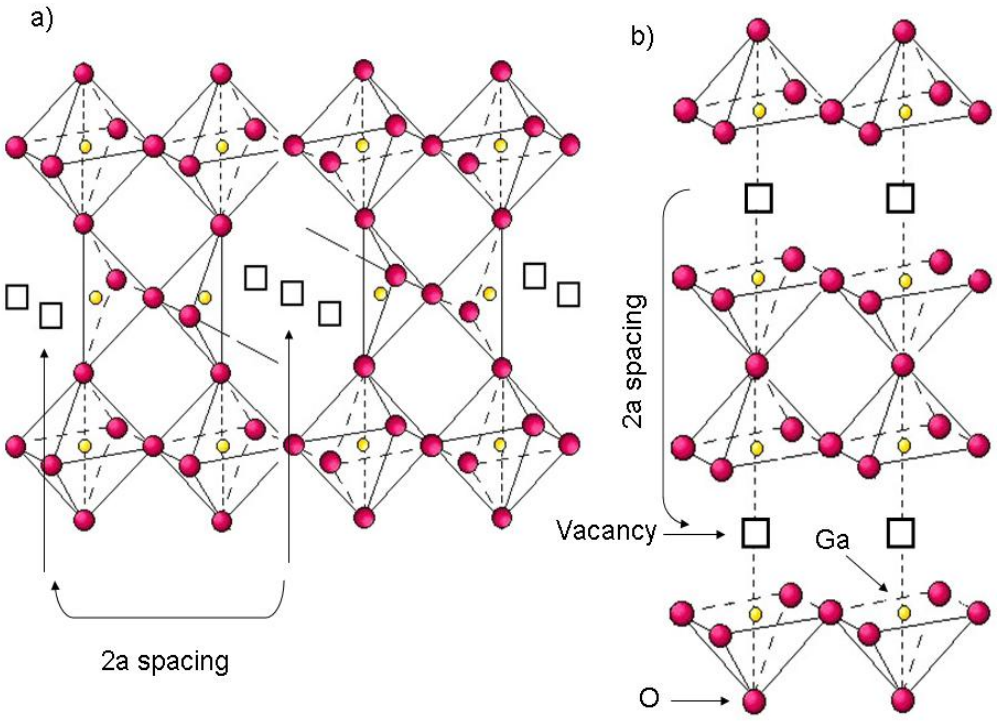

Figure 4. 73 Two models of vacancy ordering. In (a), the Brownmillerite structure. In (b), the oxygen vacancies order on the apical O2 site.

Through computer simulation, was shown in [28] that a tetrahedral B cation is more energetically favorable than a 5 coordinate cation arrangement in Brownmillerite. It is on this premise that the resonance seen emerging at 240°C is tentatively assigned to a 4 coordinate Ga. The ^{71}Ga NMR VT spectra of LGM10 show a similar trend. A similar resonance appears at 240°C, however, at room temperature this resonance is also suggested from a broad resonance at approx 116 ppm. Calculated activation energies of mobility of oxygen vacancies in [15] as a result of Mg doping vs. Sr doping reveal that Mg acts as a 'trap' of oxygen vacancies where Sr does not. This difference in activation energy could explain how this resonance appears in both the room temperature and 240°C spectra of LGM10, albeit at different resonances (116 ppm for room temp and 87 for 240°C). Presumably, the more broad resonance at 116 ppm in this spectrum could be more likened toward 4 coordinate Ga whereas the more narrow resonance is possibly the 5 coordinate.

For the ^{71}Ga NMR spectra of LSGM4,4 (fig 4.29), similarities are found to the LGM10 spectra. The resonance appears at higher frequency in the room temp spectrum at approx 126 ppm and, upon heating, moves to ~110 ppm and

seems to narrow. The same rationale follows as for the LGM10 and this resonance is tentatively assigned to a 5 coordinate Ga site. Increasing the dopant level, tends to broaden the main resonance , presumably because of increased disorder, creating larger distributions in chemical shift and 2nd order quadrupole interactions [19], and these weak resonances disappear. It is assumed that the resonances of these lower Ga coordination environments are also broadened from the same interactions and are hidden by the main resonance of the 6 coordinate Ga environment.

4.5 Conclusion

Mechanochemical synthesis of the singly and doubly doped compounds has been demonstrated as an effective means to form singly and doubly doped $LaGaO_3$ compounds at lower temperatures. In addition, mechanochemical synthesis has been shown to produce the phase pure cubic LSGM2020. Through the use of ^{17}O and ^{71}Ga NMR, oxygen vacancies induced by substitution of divalent cations for trivalent cations on the La and Ga sites by Sr and Mg, respectively, affect the crystal structure of $LaGaO_3$. Oxygen vacancies are ordered in the temperature ranges of the NMR spectra. ^{71}Ga MAS NMR results show that Ga inhabits a range of coordination environments of 4, 5 and 6 in doped lanthanum gallate. In the ^{17}O MAS NMR spectra, oxygen motion occurs in the singly and doubly doped compounds and as evidenced by the loss of spinning side bands present in the room temperature spectra. A model where there the Ga-O-Ga bonds are bent, as in stoichiometric $LaGaO_3$, but where there are no cooperative tilts (resulting in a decrease in symmetry from cubic) best describes the resonances seen in the room temperature ^{17}O NMR spectrum of LSGM1717 while the anisotropic model, where rapid rotation of the oxygen atoms about the Ga-Ga interatomic vector, combined with oxygen motion from one oxygen site to another best describes the spectrum collected at 240°C.

4.6 References

[1]. A. M. Glazer, *Acta Cryst.* **1972,** B24, 3384.
[2]. W. Marti; P. Fischer; F. Altorfer; H. J. Scheel; M. Tadin, *J. Phys. Condens. Matter* **1994,** 6, 127-135.
[3]. T. Ishihara; H. Matsuda; Y. Takita, *J. Am. Chem. Soc.* **1994,** 116, 3801-3803.
[4]. P.R. Slater; J.T.S. Irvine; T. Ishihara; Y. Takita, *J. Solid State Chem.* **1998,** 139, 135-143.
[5]. J. P. Martinez; D. M. Lopez; J.C.R. Morales; B.E. Buergler; P. Nunez; L.J. Gauckler, *J. Pow. Sour.* **2006,** 159, 914-921.
[6]. M. Lerch; H. Boysen; T. Hansen, *J. Phys. Chem. Solids* **2001,** 62, 445-455.
[7]. Y. Matsuzaki; I. Yasuda, *Solid State Ionics* **2002,** 152-153, 463-468.
[8]. M. Kajitani; M. Matsuda; A. Hoshikawa; S. Harjo; T. Kamiyama; T. Ishigaki; F. Izumi; M. Miyake, *Chem. Mater.* **2005,** 17, 4235-4243.
[9]. P. R. Slater; J. T. S Irvine; T. Ishihara; Y. Takita, *Solid State Ionics* **1998,** 107, 319-323.
[10]. A. Skowron; P. Huang; A. Petric, *J. Solid State Chem.* **1999,** 143, 202-209.
[11]. S. B. Adler; J. A. Reimer; J. Baltisberger; U. Werner, *J. Am. Chem. Soc.* **1994,** 116, 675-681.
[12]. P. Huang; A. Petric, *J. Electrochem. Soc.* **1996,** 143, (5), 1644-1648.
[13]. M. Cherry; M. S. Islam; C. R. A. Catlow, *J. Solid State Chem.* **1995,** 118, 125-132.
[14]. M. S. Khan; M. S. Islam; D. R. Bates, *J. Phys. Chem. B* **1998,** 102, 3099-3104.
[15]. M. S. Islam; R. A. Davies, *J. Mater. Chem* **2004,** 14, 86-93.
[16]. M. Kajitani; M. Matauda; A. Hoshikawa; K. Oikawa; S. Torii; T. Kamiyama; F. Izumi; M. Miyake, *Chem. Mater.* **2003,** 15, 3468.
[17]. J. L. Palumbo; T. A. Schaedler; L. Peng; C. G. Levi; C. P. Grey, *J. Solid State Chem.* **2007,** 180, (7), 2175 2185.
[18]. N. Kim; C. P. Grey, *J. Solid State Chem.* **2003,** 175, 110 - 115.
[19]. T. J. Bastow; T. Mathews; J. R. Sellar, *Solid State Ionics* **2004,** 175, 129-133.
[20]. J. T. Ash; P. J. Grandinetti, *Magn. Reson. Chem* **2006,** 44, 823-831.
[21]. T. J. Bastow; S. N. Stuart, *Chem. Phys.* **1990,** 143, 459-467.
[22]. T. J. Bastow; P. J. Dirken; M. E. Smith; H. J. Whitfield, *J. Phys. Chem.* **1996,** 100, 18539-18545.
[23]. M. H. Levitt, *Spin Dynamics*. John Wiley and Sons: New York, 2001.
[24]. M. M. Maricq; J.S. Waugh, *J. Phys. Chem.* **1979,** 70, (1), 3300-3316.
[25]. P.J. Chupas; S. Chaudhuri; J. C. Hanson; X. Qiu; P. L. Lee; S. D. Shastri; S. J. L. Billinge; C.P.Grey, *J. Am. Chem. Soc.* **2004,** 126, 4756-4757.

[26]. M. Massiot; T. Vosegaard; N. Magneron; D. Trumeau; V. Montouillout; P. Berthet; T. Loiseau; B. Bujoli, *Solid State Nucl. Mag.* **1999,** 15, 159-169.
[27]. D. Massiot; V. Montouillot; F. Fayon; P. Florian, *Chem. Phys. Lett.* **1997,** 272, 295.
[28]. S. Stolen; E. Bakken; C. E. Mohn, *Phys. Chem. Chem. Phys.* **2006,** 8, 429-447.

Chapter 5:

The Detection of the Development of Crystallization of LSGM Perovskites through the use of ^{17}O and ^{71}Ga NMR Spectroscopy and X-ray Powder Diffraction

5.1 Introduction

There have been many attempts at enhancing the ionic conductivity of doped $LaGaO_3$. Many of these focus on different synthesis techniques [1-5]. The difficulty in achieving a phase pure doped compound has been noted by many authors. When LSGM1010 was first discovered in 1994 by Ishihara *et al* [6], the synthesis technique used was the solid state synthesis method, where the simple constituent metal oxides were ground with a mortar and pestle, calcined at 1000°C, reground, pelletized, sintered at ~ 1500°C for 6 hrs, then reground, re-pelletized and re-sintered. Various single and doubly doped permutations of $LaGaO_3$ have been synthesized by many other groups. These synthesis techniques include: Pechini methods and sol-gel methods [1], acrylamide polymerization[2] , microwave-assisted [3] technique, pulse laser deposition [4], and mechanochemical synthesis [5]. β - Ga_2O_3 and La_2O_3 are reactants that form the basis of $LaGaO_3$ when synthesized via the solid state synthesis or mechanochemical method.

The structural details of pure and doped $LaGaO_3$ can be found in Chapter 4. β - Ga_2O_3 monoclinic belongs to space group C2/m with lattice parameters of a = 12.23 Å, b = 3.04 Å, and c = 5.80 Å and β = 103.7° [7]. β - Ga_2O_3 has 3 crystallographic oxygen sites and two crystallographic Ga sites all with the same multiplicity [8] occupying site 4i. Two of the O sites are 3 coordinate and one 4 coordinate as is one of the Ga sites while the other Ga is 6 coordinate. La_2O_3 belongs to the hexagonal space group P-3m1 and has lattice parameters 3.937 Å x 3.937 Å x 6.130 Å (JCPDS 05-0602). La_2O_3 has two oxygen sites, one of tetrahedral coordination and one of octahedral coordination in a ratio of 2:1, respectively. The ^{17}O NMR resonances of these two oxygen sites are 584 and 467 ppm, respectively [9]. The ^{17}O NMR resonances of β – Ga_2O_3 have not been previously reported. $Mg^{17}O$ and $Sr^{17}O$ resonate at 47 and 390 ppm respectively [10].

Often the local ordering and structure differ from the macro-level structure and sometimes these differences can be exploited through synthetic manipulation. Nuclear Magnetic Resonance (NMR) measures element-specific atoms at the 1st and 2nd cation and anion coordination spheres, giving rise to structural details not seen on the macro scale. The following study exemplifies this point. Mechanochemically synthesized doped $LaGaO_3$ are observed from the 1st coordination spheres of oxygen through the use of ^{17}O and ^{71}Ga Magic Angle Spinning (MAS) NMR and compared to XRD.

5.2 Experimental

LSG10, LGM20, and LSGM1717 ($La_{0.9}Sr_{0.1}GaO_{2.95}$, $LaGa_{0.8}Mg_{0.}O_{2.9}$, and $La_{0.83}Sr_{0.17}Ga_{0.83}Mg_{0.17}O_{2.83}$, respectively. For further description see chapter 4) were synthesized via the mechanochemical route. MgO and La_2O_3 were first heated at 1000°C for 2 hrs to drive off sorbed CO_2 and H_2O, then

were combined with $SrCO_3$, Ga_2O_3 in appropriate stoichiometries (where applicable to form either the singly doped, or doubly doped material) in a Retsch Planetary Ball Mill (Model PM 100) with 3 stainless steel milling media of 10 mm Ø in a 50 ml milling chamber (such that the ratio of the masses of reactants to milling media was 1:10) and were milled for 4 hrs at 600 rpm (unless otherwise indicated). XRD were performed on a Rigaku Diffractometer with either Cu Kα or Cr Kα radiation. A second set of samples using the same stoichiometric ratios of reactants were prepared by the solid state route. Samples were mixed using an agate mortar and pestle, pressed into pellets, and sintered at 1500°C for 8-12 hours, ground, re-pelletized and re-sintered for 8-12 hrs.

$^{17}O_2$ gas (Isotec 50 - 60 atom %) was added to the raw milled powders and the sintered powders in evacuated Pyrex tubes that were then sealed with a stopcock and heated to 600°C for 12 hrs. XRD was then performed on the enriched samples to observe structural changes as crystallization commenced for the milled powders.

Variable temperature (VT) NMR data were collected in 50°C increments starting from room temperature up to 250°C. Chemagnetics spectrometers operating at 48.8 and 67.7 MHz for ^{17}O and 109.7 and 152.9 MHz for ^{71}Ga using a 4mm Chemagnetics probe, with sample spinning of 15 kHz. Hahn echo pulse sequence was used where $\pi/2 = 1.2$ μs for ^{17}O and 0.8 μs ^{71}Ga. The ^{17}O reference was set to 0 ppm using $H_2{}^{17}O$ (Isotec) and the ^{71}Ga reference was 1M $Ga(NO_3)_3$ solution also set to 0 ppm.

5.3 Results

5.3.1 XRD

XRD of the samples that were milled reveal various degrees of crystallinity. Of the samples synthesized, the XRD pattern LSG10 from the ball mill indicates that the product is the least crystalline (fig 1a). However the main perovskite peaks present indicating some reaction to form a crystalline phase. Upon heating for 12 hrs at 600°C in $^{17}O_2$ gas, the sample becomes slightly more crystalline (fig1b) opposed to heating the milled sample in air for 8 hrs, where it becomes more crystalline. Then, more rigorous heat treatment of the milled sample at 1450°C renders an even more crystalline sample. Reflections labeled with an arrow in the figure show an impurity of $SrLaGa_3O_7$ (JCPDS card # 45-0637). For LGM20, the milled sample (Fig 2a) shows a completely amorphous diffraction pattern. Upon heating to 600°C in $^{17}O_2$, the amorphous component at low 2 Theta remains, but the reflections due to the perovskite structure intensify slightly. (Fig 2b). In figure 2c, LGM20 heated to 1450°C for 6 hrs exhibits a fully developed perovskite diffraction pattern. The XRD pattern for the ball milled sample of LSGM1717 has a similar amorphous diffraction to the other samples presented in this study. The most intense peak of the perovskite structure can

be seen at ~ 32 deg of the milled sample (fig 3a). Figure 3b reveals the perovskite structure formation after ball milling for 8 hrs. Unreacted hexagonal La_2O_3 impurities are marked with an "L". Heating the sample ball milled for 4 hrs to 600°C for 8hrs increases the crystallinity of the sample.(fig 3c) Upon heating the sample milled for 4 hrs to 1450°C for 6 hrs, the crystalline phase of the perovskite is fully developed. A weak reflection due to the impurity $La_4Ga_2O_9$ (JCPDS card #13-1433) is marked with an arrow. Figure 4 shows the three samples heated in $^{17}O_2$ gas after being milled for 4 hrs. The samples synthesized via the solid state route have XRD patters similar to those found in the high temperature diffraction of the milled powders and can be seen in figure 5.

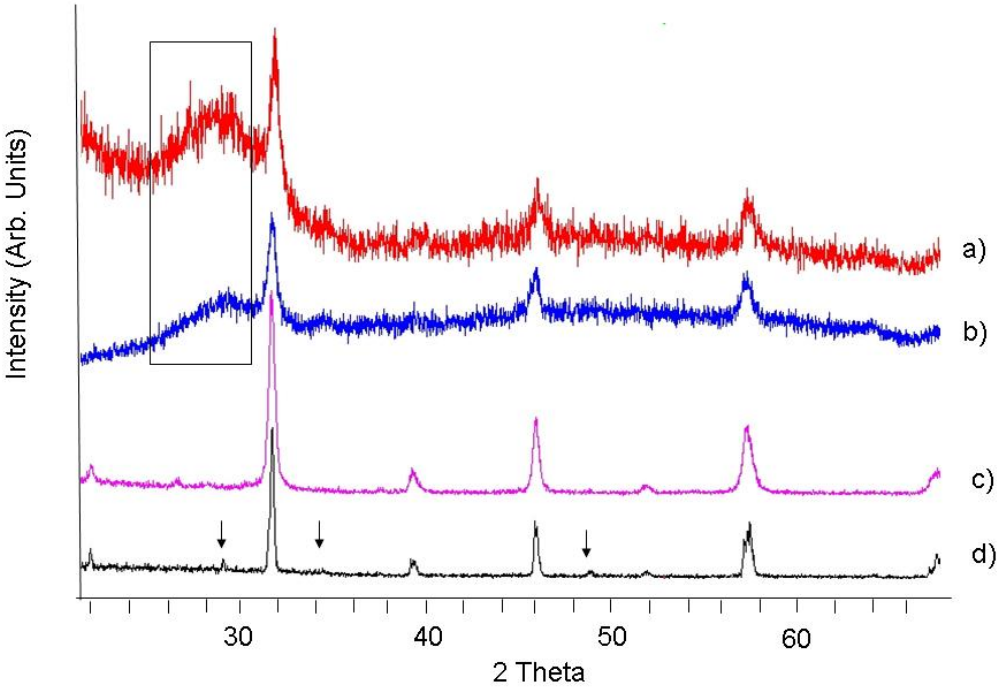

Figure 5. 14 XRD of LSG10 (a) after ball milling for 4 hrs at 600 rpm where the main perovskite peaks appear. In (b) the perovskite structure peaks appear more clearly after heating in $^{17}O_2$ gas for 12 hrs at 600°C (see figure 5.4 for indexing of perovskite reflections). Boxed in region shows an amorphous component. In (c) the same compound after heating for 8 hrs in air at 600°C. In (d) after heating at 1450°C for 4 hrs. Radiation used was Cu Kα on a Rigaku bench top diffractometer. (Impurity marked with arrow is $SrLaGa_3O_7$ JCPDS card #45-0637).

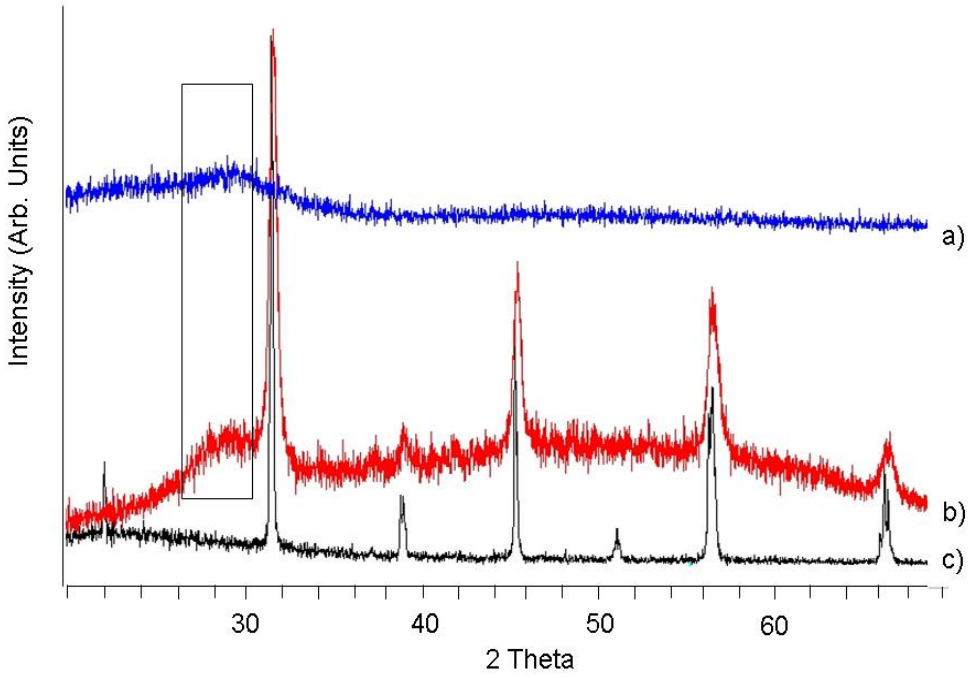

Figure 5. 15 XRD of LGM20 after ball milling for 4 hrs at 600 rpm (a). In (b) the perovskite structure peaks appear after heating in $^{17}O_2$ gas for 12 hrs at 600°C. In (c) the same compound after heating for 6 hrs at 1450°C. Boxed in region shows an amorphous component. Radiation used was Cu Kα on a Rigaku bench top diffractometer.

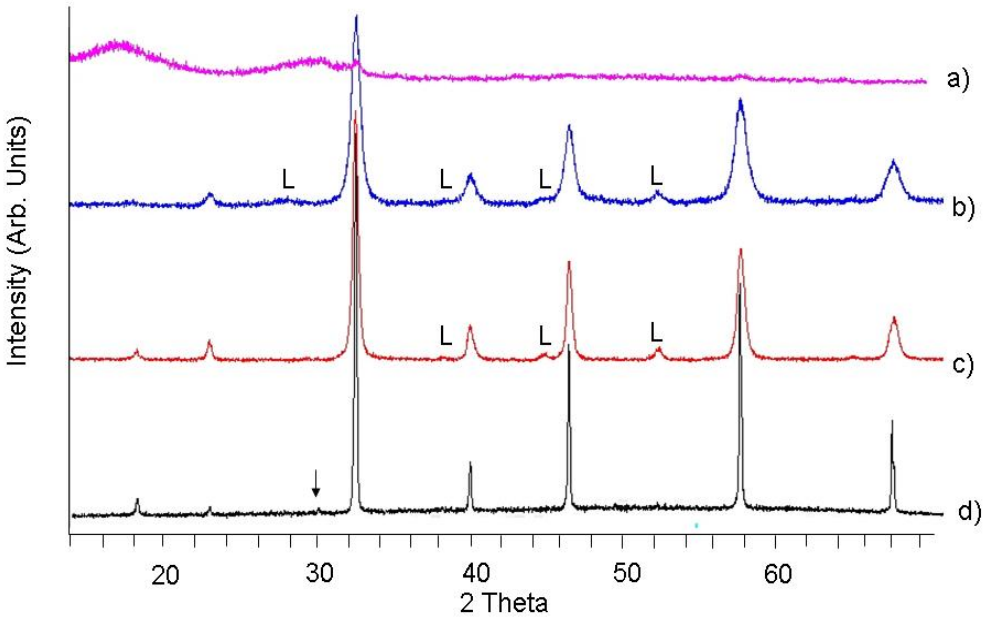

Figure 5. 16 XRD of LSGM1717 after ball milling for 4 hrs at 600 rpm (a) and (b), 8 hrs at 600 rpm (residual hexagonal La_2O_3 indicated with an 'L'). In (c) the sample that was milled at 600 rpm for 4 hrs was heated to 600°C for 8hrs (residual hexagonal La_2O_3 indicated with an 'L'). In (d), LSGM1717 that was milled for 4 hrs was heated for 6 hrs at 1450°C (impurity marked with an arrow is $La_4Ga_2O_9$ JCPDS card #13-1433). Radiation used was Cu Kα on a Rigaku bench top diffractometer.

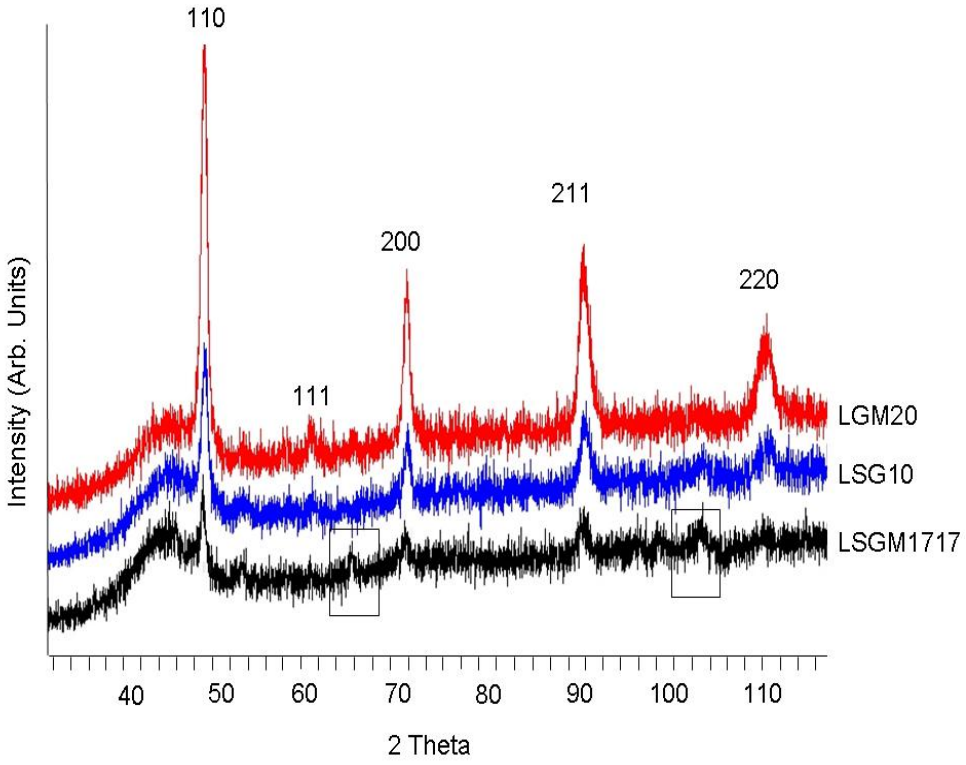

Figure 5. 17 XRD of LSGM1717, LSG10 and LGM20 samples milled for 4 hrs then treated in $^{17}O_2$ gas for 12 hrs. Boxed in regions indicate $SrLaGaO_4$ (JCPDS # 24-1208) as an impurity. Perovskite peaks were indexed to space group Pm3m. (Radiation used was Cr Kα on a Rigaku bench top diffractometer).

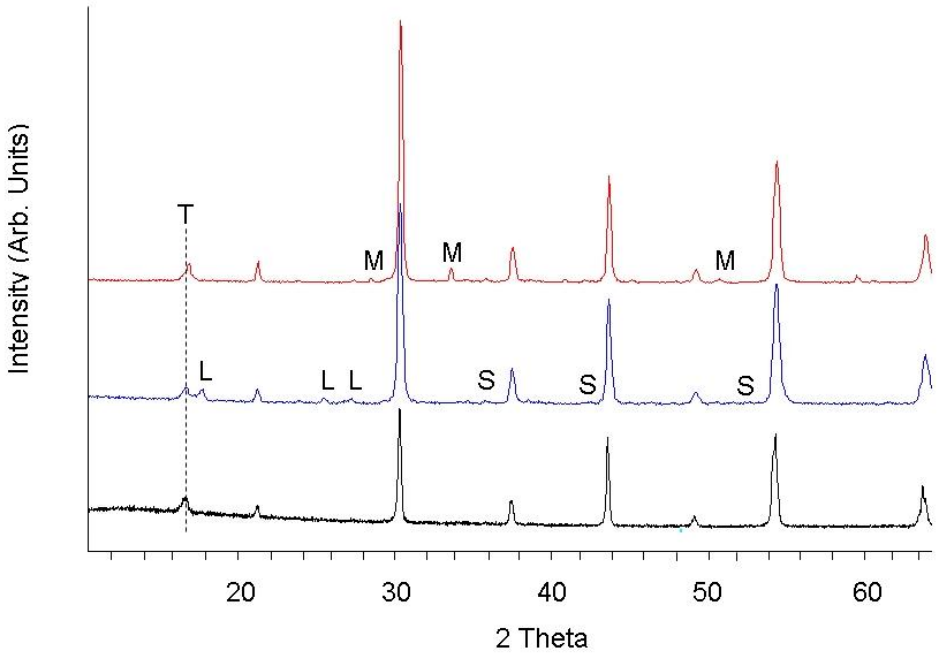

Figure 5. 18 XRD of LSGM1010, LSG10 and LGM3 synthesized via the solid state route (from bottom to top, respectively). Impurities labeled as: L = $La_4Ga_2O_9$, M = $MgGa_2O_4$, S = $SrLaGaO_4$, dashed line is Teflon sample holder. Radiation used was Cu Kα on a Rigaku bench top diffractometer.

5.3.2 ^{71}Ga NMR

In figure 6a the unheated milled sample of LSG10 exhibits a main resonance with a low frequency tail, suggestive of 2nd order quadrupolar interaction. In the heated sample of figure 6a, the line width decreases, yet exhibits the same low frequency tail as the unheated sample [11]. The broad weak resonance at 133 ppm is suggestive of another Ga environment and is reduced in intensity upon heating as seen in figure 6b. In figure 6c, the solid state synthesis exhibits a single Ga environment. The Quadrupole Coupling Constant (QCC) increases from room temperature to 250°C.

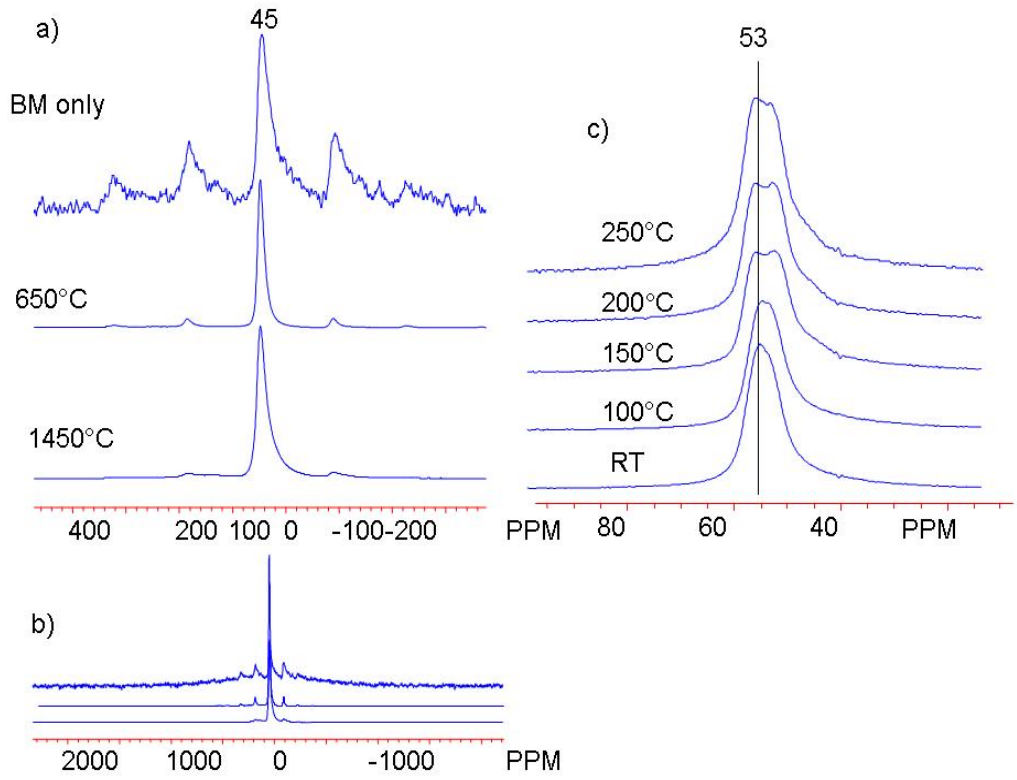

Figure 5. 19 ^{71}Ga NMR collected at 109.7MHz. In a) LSG10 Ball milled only (top), heated at 600 for 8 hrs (middle) and heated at 1450°C for 4 hrs (bottom). In b) full spectra of (a). In c) solid state synthesis as a function of temperature.

Figure 7 is the ^{71}Ga NMR collected at 109.7 MHz of LGM20. In (a) the ball milled sample (top) and the heated at 600 for 8hr (bottom) display the same line widths. The sidebands do display differences in that the side bands of the heated sample are less intense than the unheated sample. The maximum peak intensity is at 45 ppm. Figures 7a and 7b show the ^{71}Ga NMR spectra of the compound synthesized via the solid state route.

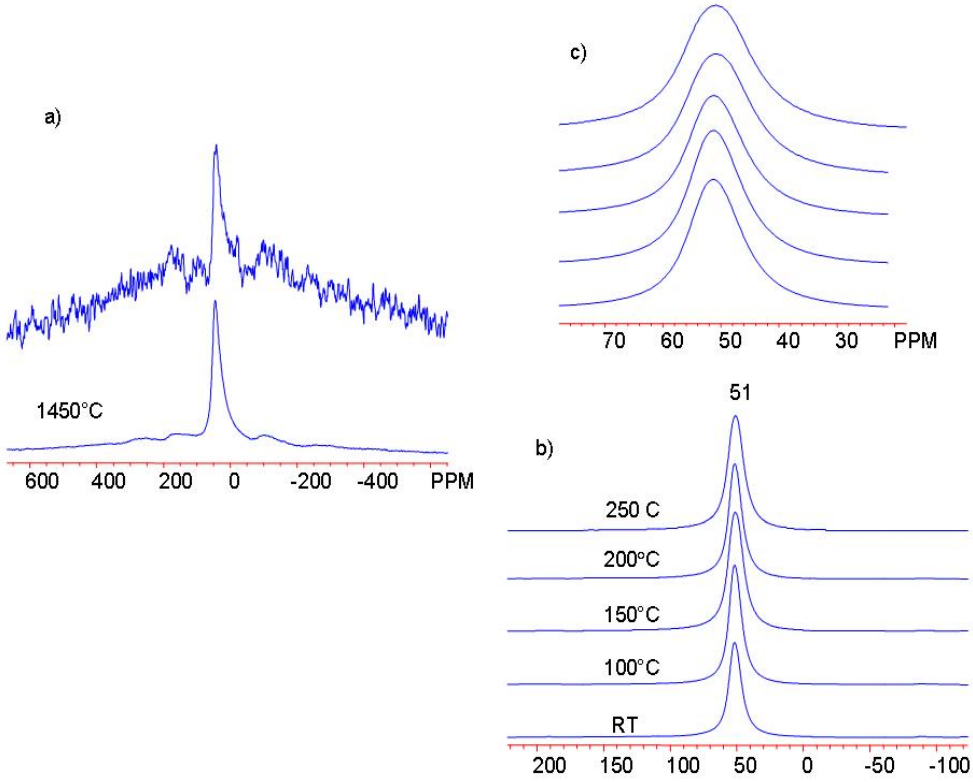

Figure 5. 20 ^{71}Ga NMR collected at 109.7 MHz of LGM20 with a rotor spinning speed of 15 kHz. In a) ball milled sample (top), heated at 1450°C for 4hr (bottom). In b) solid state synthesis. In c), a close up of isotropic resonances seen in (b).

The ^{71}Ga NMR of LSGM1717 (ball milled) and LSGM1010 (solid state synthesis) are compared in figure 8. The milled sample in 8a shows no significant changes upon heating. The solid state sample remains the same as a function of temperature, where the line widths and line shapes remain the same.

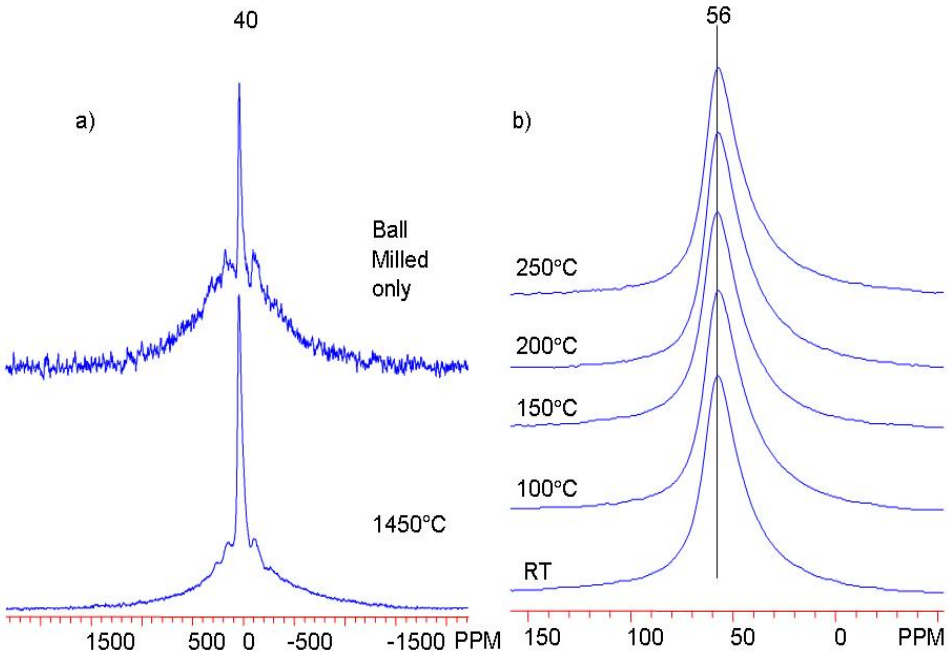

Figure 5. 21 ^{71}Ga NMR collected at 109.7MHz of LSGM1717 (a) and LSGM1010 (b). Top shows ball milled sample only. Bottom is after heating at 1450°C for 4 hrs. LSGM1010 was synthesized via the solid state route.

5.3.3 ^{17}O NMR

The $\beta - Ga_2O_3$ ^{17}O NMR spectrum in figure 9 reveals two main resonances at 94 and 4 ppm in figure 7. However, the resonance at 4 ppm is significantly broader than the resonance at 94 ppm. This suggests two overlapping resonances, where the second is assigned to ~50 ppm. It is in this region, where the two 3 coordinate oxygen environments are expected to resonate. The remaining 4 coordinate oxygen assigned to the peak at 94 ppm.

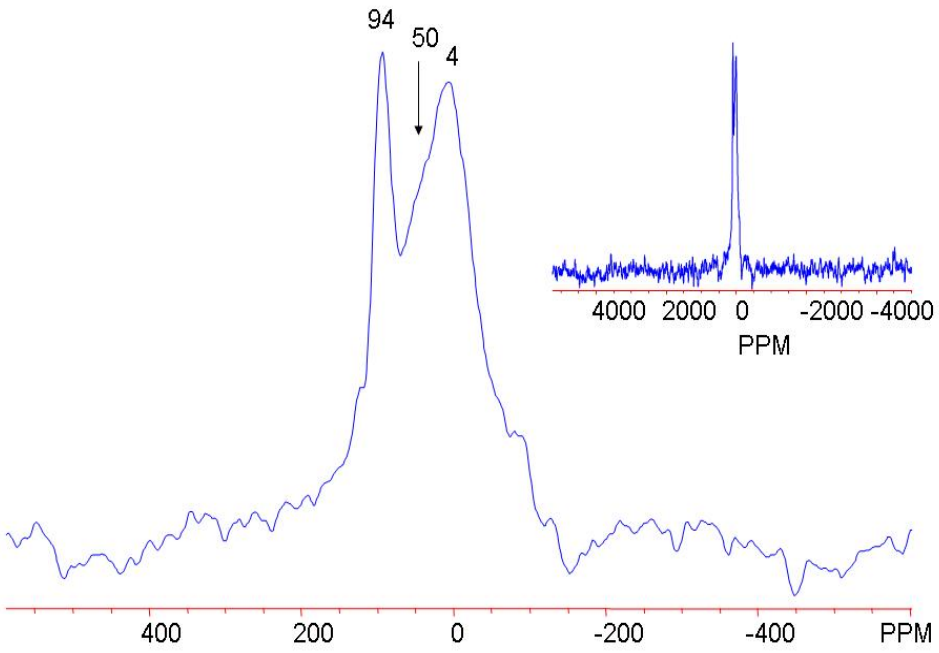

Figure 5. 22 ^{17}O NMR of β-Ga_2O_3 collected at 48.8 MHz using a Hahn echo with a rotor spinning speed of 15 kHz. A single resonance seen at 94 ppm and two overlapping resonances at 4 ppm.

The VT ^{17}O NMR of LSG10 that was milled for 4 hrs and then heated in enriched $^{17}O_2$ gas at 600°C for 12 hrs shows resonances consistent with that of La_2O_3 (540 and 465 ppm) as well as β – Ga_2O_3 with a resonance at ~102 ppm (figure 10). In addition, a sharp resonance is seen at 201 ppm and a more broad resonance at 262 ppm. These can be tentatively assigned to oxygen in the perovskite structure of LSG10. The ^{17}O NMR spectra in figure 11 of LGM20 have many similarities to the spectra in figure 10. Resonances for "La_2O_3 – like" and "β – Ga_2O_3 – like" environments are assigned to 550 and 469 (La_2O_3) and 106 ppm (β – Ga_2O_3). The zirconia rotor background can be seen in the high temperature spectrum of figure 12a. Sidebands are present in both the room temperature spectrum and the spectrum collected at 240°C in figure 11b. Figure 12 shows ^{17}O NMR spectra of LSGM1717 collected at room temperature and 240°C. The room temperature spectrum has similar resonances as LSG10 and LGM20. However, these resonances at 554, 240 and 110 (of La_2O_3, LSGM1717, and β – Ga_2O_3 respectively) are less broad that the other ^{17}O NMR spectra in this study. The resonance at 240 ppm in the

room temperature spectra has a line shape of a 2nd order quadrupolar interaction as seen in figure 10b. Upon heating, the resonance at 554 ppm disappears, and the resonance at 110 ppm becomes less intense and more broad. The ZrO_2 rotor background also becomes more pronounced at 240°C. In figure 13, the VT ^{17}O NMR spectrum of LSGM1717 synthesized via the solid state route shows featureless spectra as a function of heating from room temperature to 250°C.

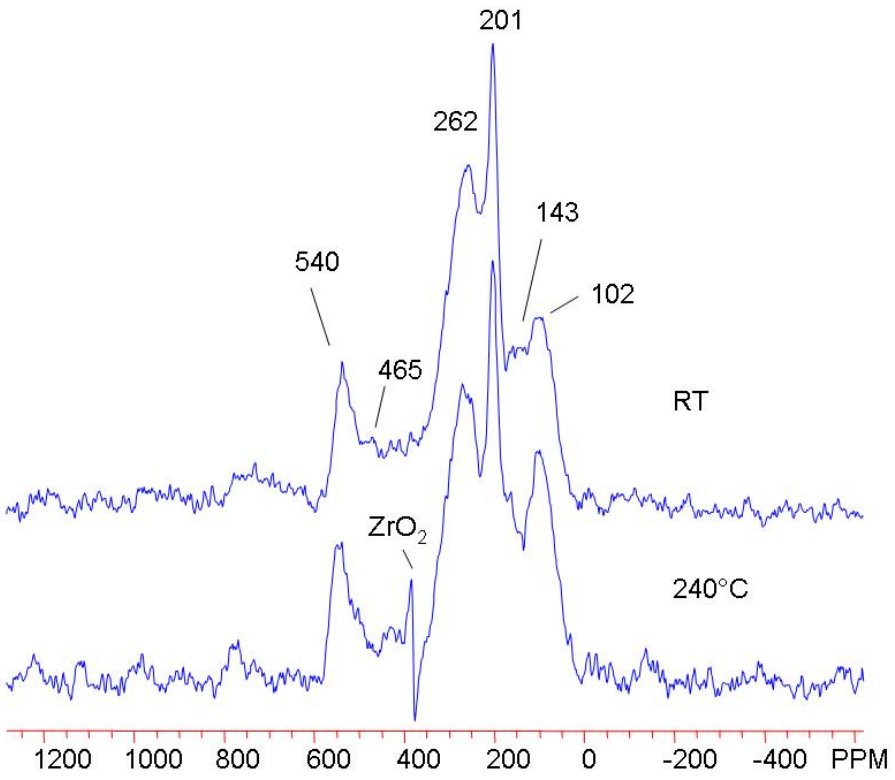

Figure 5. 23 VT ^{17}O NMR of LSG10 collected at 67.7 MHz using a Hahn echo. The sample was ball milled then heated in $^{17}O_2$ gas at 600°C for 12hrs. Multiple environments are seen in both spectra. (ZrO_2 rotor marked at 379 ppm in spectrum collected at 240°C).

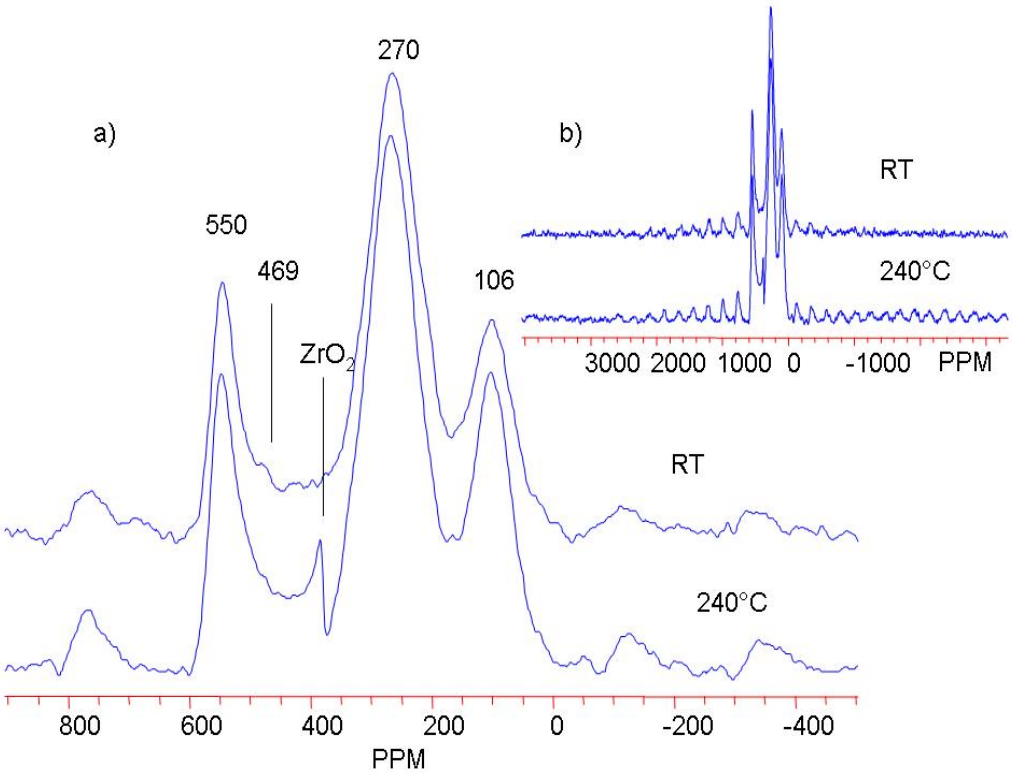

Figure 5. 24 VT ^{17}O NMR of LGM20 collected at 67.7 MHz using a Hahn echo. In a) 3 separate oxygen environments found at 550, 270 and 106 ppm in both spectra (room temperature and 240°C). ZrO_2 rotor background indicated at 379 ppm. In b) full spectrum with spinning sidebands.

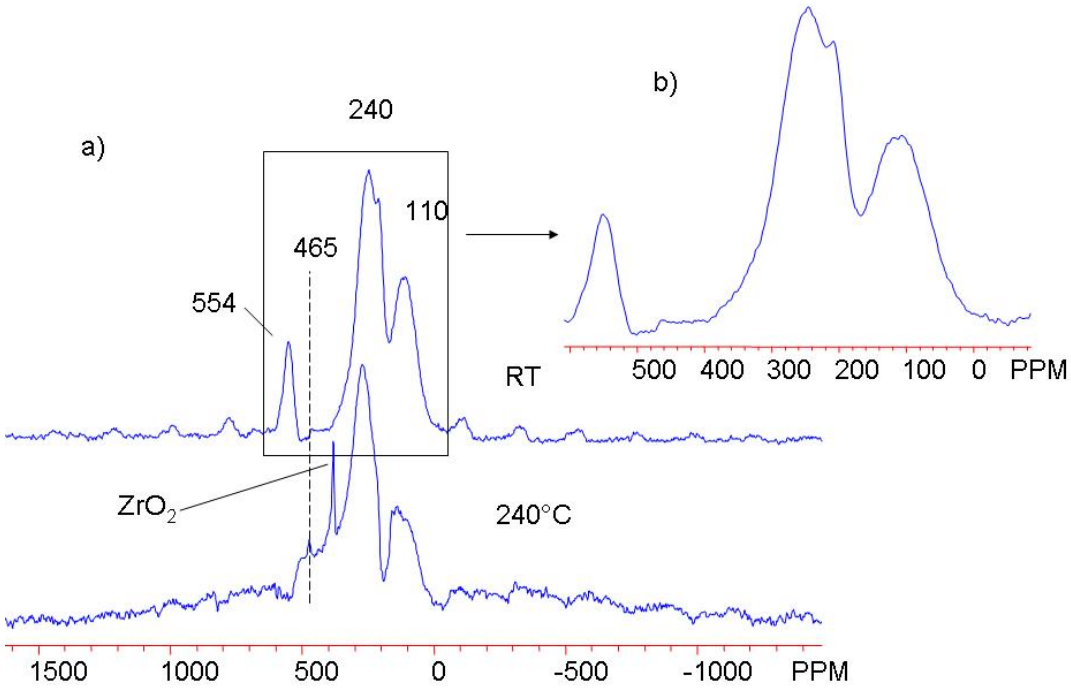

Figure 5. 25 VT ^{17}O NMR of LSGM1717 collected at 67.7 MHz using a Hahn echo. 3 separate oxygen environments are seen in room temperature spectrum at 554, 240 and 110 ppm as well as ZrO_2 rotor background in (a). In b) zoom in of isotropic resonances seen in (a).

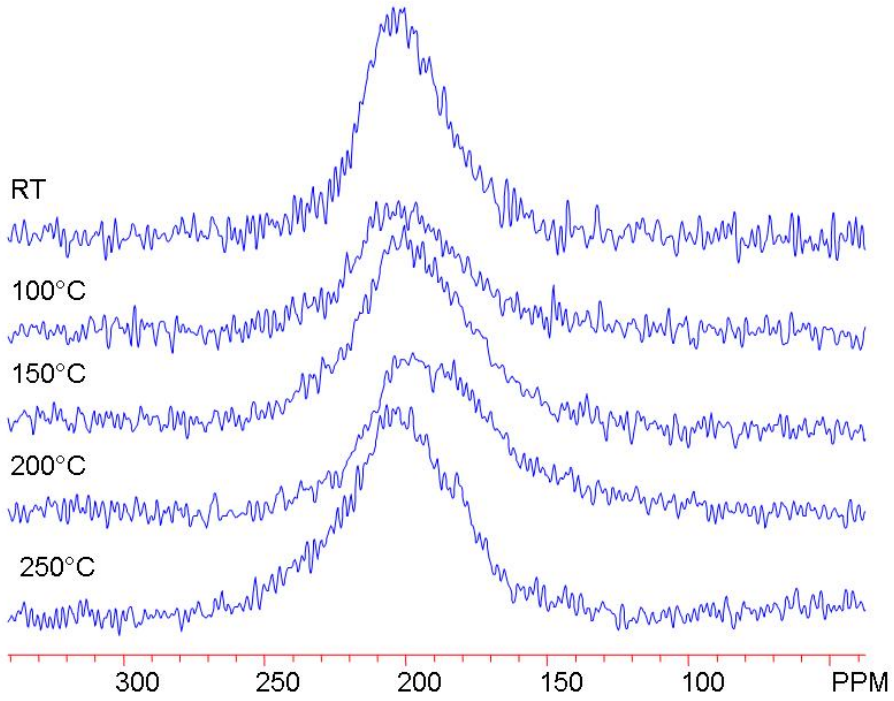

Figure 5. 26 VT ^{17}O NMR of LSGM1717 synthesized via the solid state route, collected at 48.8 MHz as a function of temperature.

5.4 Discussion

Comparing the XRD of the samples heated to 600°C in $^{17}O_2$ gas with the ^{17}O NMR spectra, it is interesting to note how the La_2O_3 and $\beta - Ga_2O_3$ reflections are absent from the diffractograms in figure 5.4. However, the ^{17}O NMR spectra of these three samples show resonances of La_2O_3 and $\beta - Ga_2O_3$ type oxygen environments, for the resonances appear very close to the resonances of the pure reactants. In addition, a resonance appears at ~ 200 ppm which is assigned to the perovskite environment. The ^{17}O NMR resonances of La_2O_3 and $\beta - Ga_2O_3$ are broader than those of the raw materials especially that of La_2O_3 (see reference 8) where the lines for the two oxygen environments are particularly narrow. Since the XRD reveal none (or very little) reflections of the reactants, the effect of ball milling has removed the long-range crystallographic order, yet the on the local level, the environments remain somewhat the same. Poor signal to noise can be ruled out for the same compounds heated to 1450°C do not have the same signal to noise ratio (see chapter 4). The broadening of the ^{17}O NMR resonances assigned to La_2O_3 and $\beta - Ga_2O_3$ regions suggests distorted local environments similar to environments found in the crystal structures yet there is no long range order.

The ^{71}Ga NMR spectra do not illustrate this point as well. This may be for the ^{71}Ga NMR of β- Ga_2O_3 as reported in [12] exhibits a very broad resonance encompassing the range of the narrow resonances seen in these spectra. The extreme contrast between the long – ranger order as seen from XRD and the local order as seem from the ^{17}O NMR spectra is exemplary of how local ordering can be significantly different from the long – range order.

5.5 Conclusion

Through the use of XRD, ^{71}Ga and ^{17}O NMR, it has been shown that extreme difference of local ordering and macro level ordering can exist. In samples prepared by ball milling and subsequently mildly heated, XRD reveals the onset of the formation of the perovskite structure, while the ^{17}O NMR reveals oxygen environments of the perovskite structure as well as resonances characterized by the reactants with approximately equal intensity. The loss of crystallinity of the reactants, as seen by XRD, show that the long range order of the reactants has been lost, but, the local environments occupied by oxygen remain, as seen by the ^{17}O NMR spectra. These results help elucidate the process of synthesizing a perovskite from metal oxide reactants via the mechanochemical route.

5.6 References

[1]. R. Polini; A. Pamio; E. Traversa, *J. Europ. Ceram. Soc* **2004,** 24, 1365.

[2]. A. Tarancon; G. Dezanneau; J. Arbiol; F. Peiro; J.R. Morante, *J. Pow. Sour.* **2003,** 118, 256.

[3]. R. Subasri; T. Mathews; O.M. Sreedharan, *Mat. Lett.* **2003,** 57, 1792-1797.

[4]. S. Kanazawa; T. Ito; K. Yamada; T. Ohkubo; Y. Nomoto; T. Ishihara; Y. Takita, *Surface and Coatings Technology* **2003,** 169-170, 508-511.

[5]. E. Gomes; M.R. Soares; F.M. Figueiredo; F.M.B. Marques, *J. Europ. Ceram. Soc* **2005,** 25, 2599 - 2602.

[6]. T. Ishihara; H. Matsuda; Y. Takita, *J. Am. Chem. Soc.* **1994,** 116, 3801-3803.

[7]. E. G. Villora; K. Shimamura; K. Aoki; N. Ichinose, *J. Cryst. Growth* **2004,** 270, 462 - 468.

[8]. S. Geller, *J. Chem. Physics* **1960,** 33, (3), 676.

[9]. T. J. Bastow; S. N. Stuart, *Chem. Phys.* **1990,** 143, 459-467.

[10]. G. L. Turner; S. E. Chung; E. Oldfield, *J. Mag. Res.* **1985,** 64, 316 - 324.

[11]. D. Coster; A. L. Blumenfeld; J.J. Fripiat, *J. Phys. Chem.* **1994,** 98, 6201-6211.

[12]. J. T. Ash; P. J. Grandinetti, *Magn. Reson. Chem* **2006,** 44, 823-831.

Chapter 6:

Conclusion

6.1 Conclusion

Continuing efforts at improving SOFC technology rely on a detailed understanding of how ionic conductivity is related to structure and how structure can be controlled by altering the synthesis conditions. Therefore, understanding the mechanism of ionic conduction as it relates to structure, and, knowing how structure is dependent on synthesis conditions, affords the opportunity to fine tune materials that exhibit ionic conduction. Characterization of a structure at the local level and long range are necessary for a more complete understanding of how the structure is related to function. Ultimately, having detailed views of both the long range and local structures of a material helps in modifying existing models and/or creating new, more accurate ones.

The work presented in this dissertation has helped to contribute to these ideas through the use of NMR and XRD, in an attempt to improve understanding of how structure at the local and long range levels aids in ionic conductivity.

Chapters 2 and 3 explore the relationship of the pyrochlore to the fluorite structures as a function of synthesis conditions and heat treatment. It was shown in chapter 2 that substitution of Zr for Y on the A site of the pyrochlore structure, in the material that crystallizes from the amorphous precursor resulted in a system that was not stable in this configuration. ^{17}O NMR and XRD characterized this by the observation of the movement of Zr from the A to the B site of the pyrochlore structure. This was accompanied by the exsolution of Zr and Ti in the forms of rutile and $ZrTiO_4$, as well as the development of the longer range ordering of the pyrochlore structure. These results help explain the somewhat surprising results presented in the earlier analysis of this crystallization process, based solely on the use of the long-range probe of structure, XRD [1]. Chapter 3 examines the effect of Zr substitution for Ti on the B site of the pyrochlore structure. The structure starts as a stoichiometric pyrochlore with all the Ti on the B site and has the formula $Y_2Ti_2O_7$. As the concentration of Zr increases, the structure gradually becomes disordered resulting in a fluorite structure, $Y_2Zr_2O_7$. It was found through the use of ^{17} O NMR that 'intermediate' oxygen arrangements begin to clearly occur at 20 mole % Zr substitution for Ti on the B site. These intermediate oxygen environments lie in between those found in the stoichiometric pyrochlore phase and fluorite structures. These 'intermediate' oxygen environments were identified as being coordinated to cation arrangements that are somewhat disordered. This disorder was not detected by XRD for the longer range order is that of a pyrochlore, where the cations are ordered. The implication is that on the local level, there are disordered domains that are similar to the disorder found in the fluorite structure. The disorder found in the fluorite structure helps explain the higher conductivity of fluorites compared to pyrochlores. In the pyrochlore structure, the oxygen vacancies are ordered and the ordering inhibits oxygen motion. The disorder of oxygen vacancies in the fluorite structure allows oxygen to be more mobile and consequently exhibit higher ionic conductivities than pyrochlores. It is suspected that these intermediate oxygen environments that are fluorite-like help promote the high ionic conductivity of these compounds [2]. In comparing the results of neutron

studies [2] to the ^{17}O NMR spectra, O3 occupancy increases, as shown by the neutron studies, while the NMR characterized the cation coordination to the O3 site. As the O3 site is occupied, the O1 site relaxes toward its ideal position found in the fluorite (3/8 1/8 1/8) [2]. The O3 and O1 sites then become closer to each other with increasing O3 occupancy and results in a repulsion of the two sites. It is concurrent with the partial occupancy of the O3 site that ionic conductivity commences.

Chapters 4 and 5 investigated the local level ordering of oxygen in LSGM. Again, the relationship between synthesis conditions and heat treatment were examined to monitor the effect of this on the 1st coordination sphere of oxygen and oxygen mobility. Chapter 4 focuses on detecting the disorder of oxygen vacancies for samples synthesized at high temperature. LSGM1717 was shown to exist in a cubic form via XRD. However, oxygen exists in more than 1 environment as shown by the room temperature ^{17}O NMR spectrum. In this ^{17}O NMR spectrum, broad overlapping resonances were observed even though this material contains only one crystallographic site for oxygen. The model of cooperative displacement does not explain local variations in oxygen ordering, for, the cubic symmetry as seen by XRD would not be maintained. On heating this material to 250 ºC, dynamics of oxygen motion were then observed via the loss of spinning sidebands and motional narrowing of the peaks. Rapid motion of the oxygen atoms about the Ga-Ga interatomic vector is consistent with the changes observed in the spectra of this compound. Both of these effects (rapid tumbling about the Ga – Ga interatomic vector and oxygen motion) best describe the high temperature spectrum. In addition to the changes in the local O environments as a function of heat, ^{71}Ga environments with coordination lower than 6 were detected as well. It was shown through the use of ^{71}Ga NMR that at room temperature, Ga inhabits an environment next to an oxygen vacancy that is that is of lower symmetry than 6 and is in low concentration, in addition to the abundant 6 coordinate environment of the GaO_6 octahedra. Upon heating, it was shown that the 4 coordinate Ga environment then prefers an environment of 5 coordinate. Detection of the 4 and 5 coordinate Ga environments allow a comparison between the two proposed models of oxygen ordering, the Brownmillerite structure and the O2 apical site vacancy [3, 4].

Finally in chapter 5, the evolution of the perovskite structure was examined at the local and long range levels as a function of mechanochemical activation. Through the use of ^{17}O NMR as well as XRD, it was shown that the metal oxide reactants Ga_2O_3 and La_2O_3 decompose, leaving Ga-O and La-O environments similar to those found in the metal oxides. XRD of the prepared samples reveal the formation of the perovskite as the main reflections are present, albeit broad. However, no reflections due to the Ga_2O_3 and La_2O_3 structures were present. The ^{17}O NMR reveals that Ga_2O_3 and La_2O_3 environments were present at the local level only. These facts lend insight into the mechanochemical process in which the Ga_2O_3 and La_2O_3 were degraded to a level where all crystallinity was lost, yet, the Ga-O and La-O like environments persisted.

Ideally this work will contribute to the advancement of technologies that produce more efficient forms of energy harvesting, helping to facilitate a cleaner environment and reduce dependence on fossil fuel.

6.2 References

[1]. T. A. Schaedler; W. Francillon; A. S. Gandhi; C. P. Grey; S. Sampath; C. G. Levi, *Acta Materialia* **2005,** 53, 2957-2968.

[2]. C. Heremans; B.J. Wuensch, ***J. Solid State Chem.*** **1995,** 117, 108-121.

[3]. P.R. Slater; J.T.S. Irvine; T. Ishihara; Y. Takita, ***J. Solid State Chem.*** **1998,** 139, 135-143.

[4]. A. Skowron; P. Huang; A. Petric, ***J. Solid State Chem.*** **1999,** 143, 202-209.